

“Design, Implementation and Application of High Throughput Magnetic Tweezers for Cell Mechanics Studies”

Von der Fakultät für Mathematik, Informatik und Naturwissenschaften der
RWTH Aachen University zur Erlangung des akademischen Grades eines
Doktors der Naturwissenschaften genehmigte Dissertation

vorgelegt von

Master of Science-Condensed Matter Physics

La Chen

aus Hunan, China

Berichter: Universitätsprofessor Dr. rer. nat. Andreas Offenhäusser
Universitätsprofessor Dr. rer. nat. Jörg Fitter

Tag der mündlichen Prüfung: 19.07.2016

Diese Dissertation ist auf den Internetseiten der Universitätsbibliothek online
verfügbar.

Zusammenfassung

In den letzten Jahren wurde gezeigt, dass die mechanischen Eigenschaften von Zellen eine wichtige Rolle bei einer Vielzahl von biologischen Prozessen spielen. Die meisten lebenden Zellen sind klein, empfindlich und sehr heterogen. Oft wurde beobachtet, dass die mechanischen Eigenschaften sehr stark von Zelle zu Zelle variieren. Daher sind mikrorheologische Methoden mit einem hohen Durchsatz von großem Vorteil für Untersuchungen der Zellmechanik. Außerdem werden meistens große mechanische Kräfte benötigt, um Zellen mit hoher Festigkeit zu untersuchen, und um die nichtlinearen mechanischen Eigenschaften von Zellen wie etwa Versteifung oder Fluidisierung zu studieren. Die meisten mikrorheologischen Verfahren sind allerdings auf kleine Kräfte, geringe Beweglichkeit und niedrigen Durchsatz beschränkt. In diesem Zusammenhang wird in der vorliegenden Arbeit der Entwurf und die Realisierung zweier mikrorheometrischer Methoden auf Basis von Magnetpartikeln vorgestellt: Magnetpinzetten (magnetic tweezers, MT) und magnetic twisting cytometry (MTC), mit denen beiden erfolgreich simultan ein hoher Durchsatz, große mechanische Kräfte und hohe Beweglichkeit erzielt wurden. Mit Hilfe dieser Verfahren wurde die Mechanik von Herzmuskelzellen und Gehirnzellen von Ratten charakterisiert.

Der erste Teil ist dem Aufbau einer Hochdurchsatz-Magnetpinzette mit drei Polen gewidmet, die zweidimensionale Aktuation von Magnetpartikeln mit hohen mechanischen Kräften erlaubt. Für einen gegebenen Magnetpartikel hängt die maximale Kraft der dreipoligen Magnetpinzette von der Größe des Probenvolumens, von der Breite der Polspitzen und von der Sättigungsmagnetisierung des Spitzenmaterials ab. Um die mechanischen Kräfte zu untersuchen und zu kalibrieren, wurde ein inverses Kraftmodell implementiert, auf dessen Basis mit Hilfe von videogestützter Positionserfassung und numerischer Lösung der Bewegungsgleichungen eine geschlossene Positionsregelschleife für einen Magnetpartikel realisiert wurde. Die Jochspitzen wurden aus einer Nickel-Eisen-Legierung mit sehr hoher Permeabilität gefertigt, um den Strom für die Elektromagneten gering halten zu können. Die Elektronik und die Software zur Spulenstromkontrolle wurden selbst erstellt, um optimale Leistungsdaten zu erhalten. Der Aufbau erlaubt es zum Beispiel, in einem Probenbereich der Größe $60 \times 60 \mu\text{m}^2$ eine Kraft von bis zu 1 nN in beliebiger Richtung auf einen $2.8 \mu\text{m}$ großen superparamagnetischen Partikel wirken zu lassen, die mit einer Rate von bis zu 1 kHz geändert werden kann. Die in der Praxis erreichbaren Kräfte sind oft niedriger als die rechnerisch vorhergesagten Werte. Dies konnte auf zwei Gründe zurückgeführt werden: einerseits wurde festgestellt, dass die magnetischen Eigenschaften der Jochspitzen durch das Laserschneiden im Fertigungsprozess durch Phasentrennung und ungleichmäßige Aufrauung verschlechtert werden, andererseits durch einen Effekt der dreidimensionalen Geometrie, der in der zweidimensionalen Simulationsrechnung nicht erfasst werden kann. Außerdem spielt die genaue Spitzengeometrie eine wichtige Rolle hinsichtlich der detaillierten Kraftverteilung.

Im zweiten Teil der Arbeit wird die Korrosion der magnetischen Spitzen bei Kontakt mit mehreren Zellkulturmedien untersucht. Eine deutlich verstärkte Korrosion wurde in Zellmedien zur Kultur von Herzmuskelzellen und Nervenzellen beobachtet, aber nicht im Zellmedium für HEK-Zellen. Um die Korrosion zu unterbinden, wurden die beiden Passivierungsmethoden der elektrochemischen Polypyrrol-Deposition und der pyrolytischen Parylen-C-Deposition untersucht. Dabei wurde festgestellt, dass die Qualität der Polypyrrol-Deposition im Bereich der lasergeschnittenen Jochspitzen unzureichend ist. Die Parylen-Deposition hingegen lieferte ausgezeichnete Isolationseigenschaften. Es wurde gezeigt, dass sowohl Herzmuskelzellen als auch primäre Nervenzellen gemeinsam mit Parylen-beschichteten Spitzen lange Zeit kultiviert werden können. Außerdem widersteht die Parylenbeschichtung den wiederholten hohen mechanischen Kräften der magnetischen Aktuierung.

Im dritten Teil der Arbeit wurde eine neuartige zweidimensionale optische magnetic twisting cytometry (MTC) auf Basis des Magnetpinzetten-Aufbaus implementiert, in der sowohl die Stärke als auch die Richtung des Biege-Magnetfeldes kontrolliert werden können. Sowohl das Polarisations- als auch das Biegefeld werden mittels Elektromagneten erzeugt. Ein separater Hochfeld-Elektromagnet wurde verwendet, um die an die Oberflächen der Zellen gebundenen Magnetpartikel aufzumagnetisieren. Das vorhandene Sechspol-Joch wurde ohne Spitzen verwendet, um das Biege-Magnetfeld aufzubringen. Für Felder kleiner 100 G wurde eine gute Linearität und ein geringer Phasenfehler erreicht. Mittels der Heterodyn-Technik gelang es, die Messfrequenz bis auf 1 kHz hochzutreiben.

Im letzten Teil der Arbeit wird die Verwendung der neuentwickelten mikrorheologischen Instrumente beschrieben, um die mechanischen Eigenschaften von Herzmuskelzellen und Gehirnzellen von Ratten zu studieren. Die Kriecheigenschaften und die Frequenzantwort von HL-1-Zellen wurden mit dem System sowohl in Pinzetten- als auch im MTC-Modus untersucht. In beiden Betriebsmodi wurde eine näherungsweise lognormale Verteilung der Steifigkeit der Zellen gefunden. Die Heterogenität der Steifigkeit einzelner Zellen war sehr groß. Bei auf festen Substraten kultivierten HL-1-Zellen wurde ein deutlicher Versteifungseffekt bei niedrigen Frequenzen gefunden, der von der mechanischen Vorspannung durch Myosin-Aktivität abhängt. Außerdem wurden die mechanischen Eigenschaften von Ratten-Neuronen und von Glia-Zellen mittels Magnetpinzette untersucht. Dabei wurde eine wachsende Steifigkeit beider Zellarten mit zunehmendem Reifegrad festgestellt. Im Falle neuronaler Zellen reduziert sich der Exponent des Potenzgesetzes mit wachsender Zellreifung, aber im Falle der Glia-Zellen bleibt er konstant. Besonders im Frühstadium wurde eine hohe mechanische Spannung der Neuronen gefunden. Außerdem werden die Neuronen steifer bei wachsender mechanischer Kraft. Es zeigte sich, dass das Elastizitätsmodul sowohl von Neuronen als auch der Glia-Zellen von der Festigkeit des Substrats abhängt.

Abstract

Recently it has been shown that the mechanical properties of cells play a very important role in various biological processes. Most living cells are small, fragile and highly heterogeneous. It is frequently observed that there is a large inherent variation in mechanical properties from cell to cell. Therefore, high throughput microrheology methods are always favorable in cell mechanics studies. Furthermore, high forces are usually needed to study cells with high stiffness and to analyze nonlinear mechanical properties such as stiffening or fluidization phenomena in cells. However, most available microrheology tools are limited to small force, poor maneuverability, and low throughput. In this context, the current thesis presents the design and implementation of two types of magnetic probe based microrheometers: magnetic tweezers (MT) and magnetic twisting cytometry (MTC), in both of which high throughput, high force (stress), and good maneuverability were successfully achieved at the same time. With the help of these tools, the mechanics of rat cardiomyocytes and brain cells were characterized.

The first part of this work focuses on the implementation of a high throughput, high force tri-pole electromagnetic tweezers which can achieve 2D actuation. For a given magnetic bead, the maximal force of tri-pole magnetic tweezers depends on the size of the workspace, the width of the magnetic tips, and on the saturation magnetization of the tip material. In order to conveniently calibrate and study the force behavior, an inverse force model based on a numerical solver and active video tracking based feedback control were implemented. Material with high permeability was adopted as the main yoke to reduce the coil current. The electronics and software were custom-made to achieve high performance. For example, with a workspace of $60 \times 60 \mu\text{m}^2$, a force of up to 1 nN can be applied on a $2.8 \mu\text{m}$ superparamagnetic bead in any direction within the plane at a speed of up to 1 kHz. However, the practically achieved saturation forces are usually lower than predicted values, which can be ascribed to two factors: magnetic performance deterioration near the cutting edges of the tips and 3D geometrical effect. The high power laser used in cutting causes segregation and morphological roughness near the cutting edge. Moreover, the geometry of the magnetic tips plays an important role regarding the force behavior.

In the second part, the corrosion of the magnetic tips in several cell culture media was characterized. Obvious accelerated corrosion was observed in cardiomyocyte and neuronal cell media, but not in HEK cell medium. Both the electrochemical deposition of polypyrrole and the pyrolytical deposition of parylene-C were examined for passivation. It was found that the quality of polypyrrole deposition is insufficient in the area near the edges of the tweezers tips where they had been laser-cut. However, the parylene coating exhibits excellent isolation properties. Both cardiomyocyte and primary neuronal cell can be cultured on parylene-coated magnetic parts for a long time. In addition, the coated parts can also withstand repeated high magnetic field application.

In the third part, based on the magnetic tweezers setup, a novel optical 2D magnetic twisting cytometry was implemented, in which both the strength and direction of the twisting field can be controlled. In the MTC system, both polarization and twisting magnetic field were based on electromagnets. A separate high field electromagnet was utilized to magnetize the ferromagnetic particles bound on the surface of the cells. The existing hex-pole yoke electromagnet, but without tips, was used to apply the twisting magnetic field. When the twisting field is less than 100 G, good linearity and small phase error can be achieved. Using the heterodyning technology, the measurement frequencies were extended up to 1 kHz.

In the last part of the thesis, these developed microrheology tools were used to study the mechanical properties of rat cardiomyocytes and brain cells. Both the creep and the frequency response of cardiomyocyte HL-1 cells were characterized with the instrument operated in magnetic tweezers mode and in magnetic twisting cytometry mode, respectively. In both modes, the stiffness of HL-1 cells exhibits approximately log-normal distributions. High heterogeneity of single cell stiffness was also noticed. When HL-1 cells were cultured on a stiff substrate, there was an obvious stiffening effect at low frequency, which depends on the prestress generated by myosin activity. In addition, the mechanical properties of rat neuronal and glial cells were studied with magnetic tweezers. It was found that with increasing maturity, the stiffness of both neuron and glia increases. The power-law exponent of neuronal cells decreases with increasing cell maturity, but the one of glia cells does not change. Especially in early stage, it was found that there is high tension in neurites. Furthermore, the neuronal somas become stiffer with the applied stress. Both the elastic modulus of neurons and glia were also sensitive to the rigidity of the substrate.

Contents

Zusammenfassung	III
Abstract.....	V
Contents	VII
1. Introduction.....	1
2. Fundamentals	5
2.1 Magnetism Fundamentals	5
2.1.1 Basic Magnetism.....	5
2.1.2 Superparamagnetism.....	7
2.1.3 Magnetic Force and Torque.....	8
2.1.4 Magnetic Field Generation	9
2.2 Cell Mechanics Models	11
3. Materials and Methods	14
3.1 Magnetic Microrheometry System	14
3.1.1 System Configuration	14
3.1.2 Magnetic Actuator	17
3.1.3 Electronics	20
3.1.4 Particle Tracking.....	24
3.1.5 Magnetic Field Simulation.....	27
3.1.6. Inverse Force Model	28
3.1.7 Feedback Control.....	30
3.1.8 Force Calibration	32
3.2 Cell Culture and Experiments.....	33
3.2.1 Cardiomyocyte HL-1 cell	33
3.2.2 Primary rat brain cell	35
4. Results and Discussion	37
4.1 Multi-pole Magnetic Tweezers.....	37
4.1.1 Force Produced by Multi-pole Magnetic Tweezers.....	37
4.1.2 Tri-pole Magnetic Tweezers.....	39
4.1.3 Force Reduction in High Force Magnetic Tweezers	42
4.1.4 Summary on Multi-pole Magnetic Tweezers	52
4.2 Magnetic Tips Passivation	53

4.2.1 Corrosion in Cell Medium.....	53
4.2.2 Polypyrrole Coating	54
4.2.3 Parylene Coating	55
4.2.4 Cell Viability	57
4.2.5 Summary on Magnetic Tips Passivation	58
4.3 Magnetic Twisting Cytometry Based on Electromagnets	59
4.3.1 Configuration	59
4.3.2 Heterodyning Technique	60
4.3.3 Magnetic Field	62
4.3.4 Summary on Magnetic Twisting Cytometry	64
4.4 Characterization of Cell Mechanics with High Throughput Magnetic Microrheometries.....	64
4.4.1 Characterization of Cardiomyocyte Mechanics with Magnetic Tweezers	64
4.4.2 Characterization of Cardiomyocyte Mechanics with Magnetic Twisting Cytometry	68
4.4.3 Characterization of Brain Cells Mechanics with Magnetic Tweezers	73
4.4.4 Summary on the Mechanics Characterization of Cardiomyocyte and Brain Cells	82
5. Conclusion.....	84
6. Outlook.....	87
References	89
Abbreviations	95
Author's list of publications.....	96
Acknowledgments.....	97
Appendix	98

1. Introduction

For most living beings, cells are the basic structural and functional units. Both the mechanical properties of cells and their response to mechanical signals usually play a vital role in various biological processes, such as the maintenance of shape, migration, differentiation, and mechanical signal sensing [1-4]. The mechanical properties of cardiomyocytes are very important for the heart function. It is well established that the cytoskeleton in cardiomyocytes plays a pivotal role in sensing mechanical stress, mediating structural remodeling, and functional response in both physiological growth and pathological stimuli [5, 6]. Cardiopathy is usually relevant to abnormal mechanical properties of heart tissue [6-8]. There are evidences that the development of heart depends on the environmental stiffness [9, 10]. On the other hand, the growth and development of the brain tissue, which includes neuronal and glial cells, is a highly complex process involving various biochemical and biophysical interactions [11-13]. The mechanical interaction with the environment plays a key role in various important processes such as axon growth, foreign body reaction, and brain folding [14-16]. Therefore, it is very interesting to study the mechanical properties of these cells under different conditions.

Most living cells are small, fragile and can only be handled very carefully. Because of the small size and low elastic modulus of cells, the mechanical measurement technique needs to be capable of applying and monitoring deformations and forces in the range of μm to nm and pN to nN , respectively [17]. Therefore, it is difficult to characterize the viscoelastic properties of living cells with conventional rheometry. In the last decades, a variety of microrheology techniques have been developed to actively or passively investigate the mechanical properties of cells [17, 18]. The active rheology methods usually characterize the mechanical properties of a material by measuring the deformation of the material under an applied force, or vice versa. Tools such as atomic force microscopy (AFM) [19-21], optical tweezers (OT) [22-24], microplate rheometer [25, 26], and magnetic tweezers (MT) [27-29] can be used to measure the temporal evolution of cell strain under a constant stress. Besides that, the frequency-dependent mechanical properties of cells can be determined by oscillatory measurement methods such as magnetic twisting cytometry (MTC) [30, 31] and AFM [32, 33]. Furthermore, because of the high resolution, OT, AFM, MT are also widely used for single-molecule force spectroscopy techniques [34]. Without external stimuli, passive rheology methods such as particle tracking microrheology (PTM) [35-37] measure the intracellular mechanical properties by tracking the thermally driven motion of the embedded tracer particles.

It is well known that the elastic modulus of eukaryotic cells covers a broad range: from soft cells like fibroblast (few hundred Pa) to the hard cells like cardiac myocytes (several dozen kPa) [4]. Furthermore, nonlinear mechanical properties such as stiffening and fluidization at high stress have been observed in many cell rheology experiments [38, 39]. Therefore, a rheology tool which can apply a sufficiently high force is significant for the studies of cells with high stiffness and of the cell

behavior under high stress. The log-normal distribution of cell stiffness has been frequently reported [26, 33, 40]. One of the reasons for the large variation is the inherent complexity and high heterogeneity of cell structures [30, 41, 42]. Besides this, the linkage between probe and cell usually also has significant effects on the mechanical response of cells [18, 43]. Hence, there could be some large deviations in the cell stiffness measured by different microrheometric techniques. However, the frequency response of cells measured with different techniques can be compared by rescaling [18]. Therefore, high throughput and multi-frequency measurements are usually favorable for cell mechanics studies. Although high force can be achieved easily in AFM and microplate rheometer, usually only a single probe can be applied at a time in these tools. Optical tweezers have a similar low throughput and the high laser intensity could cause damage to the cell organelles [44]. PTM such as two-point microrheology inherently adopts multi-probe and multi-frequency measurements, however, it can be only used for low stiffness situations, and is also susceptible to experimental conditions [36].

In the various microrheology techniques, magnetic tweezers exhibit a number of advantages, such as relatively high force, multi-dimensional actuation, and high spatial and temporal resolutions [34, 45]. Superparamagnetic beads, which are non-hysteretic and do not agglomerate in the absence of a magnetic field [46, 47], are usually adopted as measuring probes in magnetic tweezers. Via a magnetic gradient field, magnetic tweezers generate a force on the magnetic particles. Due to their extraordinary advantages and because they are easy to implement, magnetic tweezers have become an increasingly important tool in the study of single molecules and cell biophysics. For example, magnetic torque tweezers are especially suitable for twisting measurement of single DNA molecules [48, 49], in which, besides the pulling force, a small torque can be generated because of particle's magnetic anisotropy. By binding the magnetic particle to components of cellular membranes, the mechanosensitive ion channels can be modulated or controlled [50, 51]. In addition, the mechanical properties of cell membrane, cytoplasm and nucleus can be analyzed by manipulating micro-magnetic probes [28, 52-54]. Recent advances in high resolution microscopy, sophisticated bead tracking algorithms, high speed camera, and novel magnetic particle syntheses lead this tool to multi-functionality and expand its potential application [55]. In general, a useful magnetic tweezers should: (1) be able to apply strong enough force, (2) have good maneuverability, and (3) have a structure applicable to biological experiments, e.g. cell culture. It is well known that the output force of MT can be enhanced by using beads with high magnetization or by generating a high magnetic gradient field at the bead's position [29, 56]. Usually, the magnetization can be improved by adopting large size beads with embedded magnetic nanoparticles (MNPs), and a high volume ratio of magnetic material. However, this is compromised by the magnetic properties such as coercivity, and by coating stability [57, 58]. In order to generate a high magnetic gradient field, two main methods are used: 1) adopting soft magnetic materials with high saturation magnetization M_s , and 2) employing small sharp structures. For example, with 5 μm magnetic beads, single-pole magnetic tweezers can apply up to 100 nN pulling force at 10 μm distance from its tip [56]. Most of the high force MTs were realized as single-pole electromagnets which limits their applicability because they do not allow manipulation of

magnetic probes in different directions. By using multiple magnetic poles, maneuverability can be achieved. With two opposing magnetic poles, bi-directional magnetic forces can be generated [59]. With three or four poles symmetrically placed in one plane, 2D actuation can be achieved [29, 60]. To generate magnetic forces in 3D direction, a six-pole magnetic actuator, with three poles each in the top and bottom plane, has been designed and implemented [61, 62]. With the help of gravity force, 3D manipulation can be achieved also with magnetic poles only in one plane [63]. Compared to single-pole MT, multi-pole MTs usually have a larger effective workspace in which the force changes more smoothly. However, in most available multi-pole MTs, the achieved forces are usually small [60, 63]. Although high force has been achieved in tri-pole magnetic tweezers by adopting a small workspace, only a single cell can be measured at a time like in the single-pole MT [29]. Furthermore, in practice, the achieved saturation forces are usually lower than predicted values. One cause for the force reduction is the thickness effect: the achievable force reduces with decreasing tip thickness [29, 64]. Besides the geometry of the front magnetic poles, the force also depends on their magnetic performance. For example, in the manufacturing of the magnetic parts, it is well known that the cutting strain can deteriorate the magnetic properties in the area near the cutting edge [65, 66]. As a matter of fact, there is a trade-off among high force, maneuverability, throughput, and manufacturing issue in practical design of magnetic tweezers.

As a high performance magnetic material, FeCo alloy possesses the highest saturation magnetization [67]. Hence, it is advantageous to implement this material for the sharp magnetic tip in MT. However, the findings from Pouponneau *et al.* show that this type of material is corrosive in a physiological solution [68]. In addition, most of the magnetic materials including elements, such as Fe, Co, and Ni, can induce cytotoxic effects when being released into extracellular fluid [69]. Hence, in order to prevent corrosion and to improve biocompatibility, appropriate passivation is essential. Because of good biocompatibility and elasticity, polydimethylsiloxane (PDMS) has been used in magnetic polymer membranes in microelectromechanical systems [70, 71]. However, due to its high viscosity, it is not suitable for conformal coating of 3D structures. Electroactive conducting polymers such as polypyrrole (PPy) have been widely used for corrosion isolation of metals [72]. Thanks to the unique conductivity and biocompatibility, PPy is a promising material for biomedical applications, especially for devices to interface with the nervous system [73, 74]. Moreover, it can be synthesized easily as a thin passivation film by electrochemical methods [75, 76]. On the other hand, parylene C has been widely used for microelectrode passivation in neuron stimulation and recording systems because of its favorable biocompatibility and excellent isolation performance [77-79]. Due to the pyrolytic vapor polymerization method, it is easy to achieve conformal, uniform and pin-hole free coating.

Unlike the high gradient magnetic field which is essential for high force MT, in MTC, only a small uniform magnetic field is used to twist the pre-polarized ferromagnetic beads [80]. Hence, there is no biocompatibility problem in MTC, in which the small twisting field can be generated remotely.

Besides, there is not such a rigorous tradeoff between high stress (torque) and throughput (size of workspace) in MTC. Therefore, it is much easier to implement a multi-cell measurement. Another advantage of MTC is that it allows multi-frequency measurement which is hard to achieve in MT. Since the appearance of this tool, it has been widely used to investigate the mechanical properties of individual adherent cells [30, 31, 81, 82]. Unlike the traditional MTC which used a magnetic field sensor to detect the bead rotation [81] [82], in the optical MTC, the lateral displacement of magnetic bead caused by rotation is detected by a camera [31]. Thus, it combines the advantages of high throughput and single cell studies. Moreover, thanks to the heterodyning technology, the measurement frequency of optical MTC has been extended to the kHz range [31]. In order to generate the twisting field, MTCs usually adopt Helmholtz coils which could cause too much heat with high coil currents. Because of the special structure of Helmholtz coils, most MTCs implement only a single pair of twisting coils, meaning that the beads can be twisted only in one direction. As in the multi-pole MT, a high performance magnetic yoke allows to decrease the coil's exciting current and to achieve better maneuverability. Therefore, it is reasonable and valuable to combine the advantages of MT and MTC in a single device, which can be easily configured into either MTC function or MT function.

2. Fundamentals

In this chapter, the theoretical aspects of magnetism and cell mechanics will be described. First a short overview of the relevant fundamentals of magnetism is given. Then there will be brief introductions of superparamagnetism, magnetic force (torque), and magnetic field generation. After that, several theoretical models of cell mechanics will be discussed.

2.1 Magnetism Fundamentals

2.1.1 Basic Magnetism

When a material is placed in a magnetic field, the magnetic field inside this material can be described as

$$\mathbf{B} = \mu_0 (\mathbf{H} + \mathbf{M}) \quad (2.1).$$

The magnetization \mathbf{M} can be interpreted as the induced volume density of magnetic dipole moment, μ_0 is the vacuum permeability, \mathbf{B} and \mathbf{H} refer to the magnetic flux density and the magnetic field strength, respectively. The magnetization \mathbf{M} usually depends on \mathbf{H} , which can be written as

$$\mathbf{M} = \chi_m \mathbf{H} \quad (2.2).$$

χ_m is the magnetic susceptibility which depends on the properties of the material. For example, the susceptibility can be a complex tensor for an anisotropic material, or a scalar for an isotropic material [83]. Based on Eqs. 2.1 and 2.2, the magnetic flux density inside a material can be expressed as the sum of the external field strength and the magnetization of the material

$$\mathbf{B} = \mu_0 \mathbf{H} + \chi_m \mathbf{H} = \mu_0 \mu_r \mathbf{H} \quad (2.3),$$

where μ_r (equals to $1 + \chi_m$) is the relative permeability of the material. As in the Table 2.1, according to the magnetization mechanism, all materials can be divided into diamagnetism, paramagnetism, ferromagnetism (also including antiferromagnetism and ferrimagnetism), and superconductor (a special state of material).

Table 2.1 Magnetic properties of materials [83, 84].

Type	Mechanism	Strength	Example substance (χ_m)
Diamagnetism	induced dipole moment	very weak	silicon (-0.41×10^{-5}), gold (-3.44×10^{-5})
Paramagnetism	permanent moment alignment	weak	manganese sulfate (3.7×10^{-3})
Ferromagnetism	exchange interaction	strong	silicon steel (1000 - 6500)
Superconductor	electron phonon interaction ¹	strong	Nb ₃ Al (-1), YBa ₂ Cu ₃ O ₇ (-1) @ $T < T_c$

¹applies for type I superconductor.

When a diamagnet is placed in a magnetic field, opposite magnetic moments will be induced in the atoms, which lead to a little lower field inside the material. Although all materials exhibit somehow diamagnetic response, the strength of diamagnetism is very weak, as seen in Table 2.1. Because of the intrinsic magnetic moment of elementary particle spin, both the electron and the nucleus in an atom possess a permanent magnetic moment. When there is an external field, these permanent dipole moments tend to align along the field. Nevertheless, the orientation of these dipoles is strongly affected by thermal fluctuations and is thus randomly distributed in absence of an external field. Furthermore, in diamagnets and paramagnets, there is no interaction among the individual moments; each moment acts independently of the others.

Unlike the aforementioned materials, there are strong dipole-dipole interactions in ferromagnetic materials, which result from the Pauli exclusion principle [83]. In the view of energy, the electrons in neighboring atoms should avoid to occupy the same state in order to keep the total energy as low as possible. The resultant interaction is also called exchange interaction. This interaction leads the neighboring spin moments to form magnetically ordered states. In ferromagnetic (antiferromagnetic) material, the individual moments tend to align parallel (antiparallel) with their neighbors'. In a bulk material, this alignment is restricted to a microscopic region which is referred as magnetic domain. However, in order to minimize the total energy, the magnetic domains throughout the material are not all along the same direction. As shown in Fig. 2.1, when a ferromagnetic material is subjected to an external field, the internal magnetic domains change depending on the field strength. With the field increase, the magnetic domains oriented along the field grow at the expense of the anti-oriented domains. Once the magnetic moments of all domains are oriented parallel to the field, the magnetization will level off and will not increase with the field any more. This magnetization level M_s is called saturation magnetization.

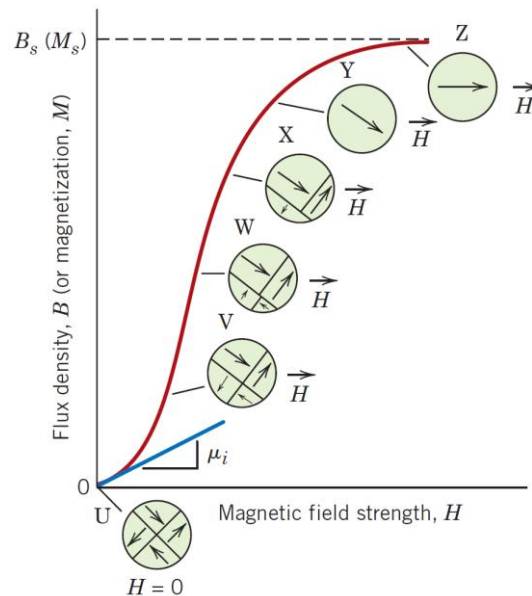


Fig. 2.1. The domain configurations and the B - H behavior of a ferromagnetic material in the initial magnetization (Adopted from [84]).

Because of the pinning of magnetic domain walls at impurities or grain boundaries within the material and the anisotropy of the crystalline lattice, in practice, there is a hysteresis phenomenon in the magnetization process of ferromagnetic material [85]. When the external field is turned off or reversed, the magnetization in materials does not follow the initial magnetization trace, as depicted in Fig. 2.2 (a). Once the material is magnetized to saturation, the remaining magnetization after removal of the field is named as remanence B_r . Accordingly, the external field needed to cancel out the magnetization in a material is referred to as coercivity H_c , seen in Fig. 2.2 (a). Materials that exhibit a small coercivity (like a few A/m in permalloy [83]) are called soft magnetic materials. In contrast, permanent magnets are made of especially hard magnetic materials. They exhibit a very high coercivity, for instance, the H_c of $\text{Nd}_2\text{Fe}_{14}\text{B}$ is about 8.48×10^5 A/m [84]. In general, the magnetization state of a ferromagnetic material also depends on its magnetization history, as seen in Fig. 2.2 (b). However, this memory effect can be wiped out by magnetizing the material with higher field. For example, the effect of an inner loop (see loop LM in Fig. 2.2 (b)) can be removed by running the material through the main B - H loop. By a demagnetization process, in which a damped alternating magnetic field is applied, the initial magnetic state can be retained.

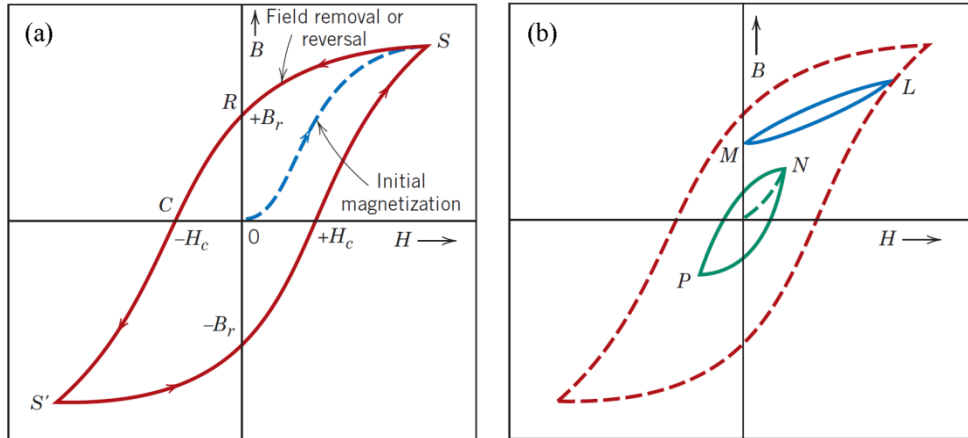


Fig. 2.2. (a) B - H curve for a ferromagnetic material that is subjected to forward and reverse saturations. (b) A hysteresis curve at less than saturation (NP) within the main (saturation) loop for a ferromagnetic material. The B - H behavior for field reversal at other than saturation is indicated by LM (Adapted from [84]).

Superconductivity is a special phenomenon, in which the material shows zero electrical resistance and expulsion of magnetic field when the temperature is lower than a critical temperature T_c . The behavior of classic superconductors (also as type I) can be described by the electron phonon interaction very well, which is known as Bardeen-Cooper-Schrieffer (BCS) theory [86]. However, the mechanisms of high temperature superconductors (type II), such as YBCO and recently reported iron-based superconductors, are very complex [87, 88].

2.1.2 Superparamagnetism

When there is no external magnetic field, the magnetic moment in single-domain ferromagnetic material can randomly flip because of thermal fluctuation, which is known as Néel relaxation. If the magnetic moment reverses at a time shorter than the measurement time scale, the material is in a

superparamagnetic state. The relaxation time depends on the competition between thermal energy and magnetic energy [85]:

$$\tau = \tau_0 \exp\left(\frac{\Delta E}{k_B T}\right) \quad (2.4),$$

where ΔE is the energy barrier to moment reversal, and $k_B T$ is the thermal energy. Usually the energy barrier is proportional to the volume of the particle. Therefore, superparamagnetism exists only when the particle is smaller than a critical size r_0 . The critical superparamagnetic size and single domain size of different magnetic particles are shown in Fig. 2.3 (a). Furthermore, the coercivity also depends on the size of the magnetic nanoparticle (MNP), as seen in Fig. 2.3 (b). For particles larger than r_0 , the coercive field increases with the single domain size. With further increasing size, the formation of a multi-domain structure becomes energetically favorable.

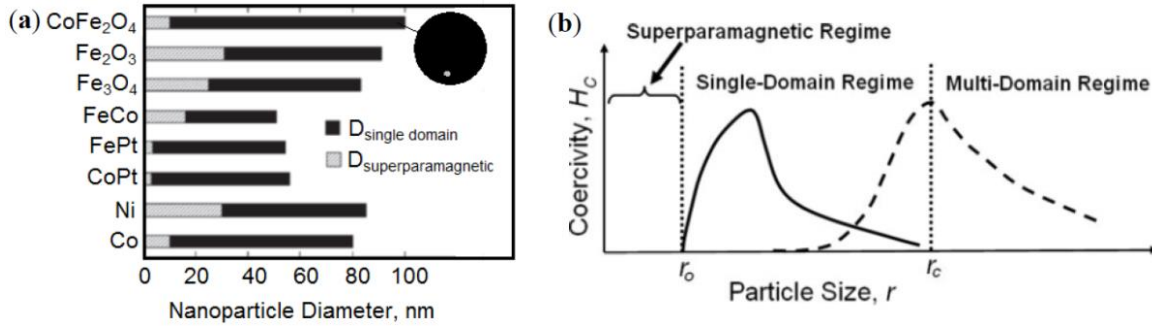


Fig. 2.3. Magnetic property and particle size (Adopted from [89] and [90]).

Like in ferromagnetic materials, the response of superparamagnetic nanoparticles to an external field follows a sigmoidal curve but shows no hysteresis. Its behavior can be approximately described by the Langevin function [91]:

$$m(H) = m_s \left(\coth\left(\frac{H}{a}\right) - \frac{a}{H} \right) \quad (2.5).$$

Here, H refers to the magnetic field strength, m_s is the saturated magnetic moment of the particle. Parameter a is related to temperature and the material's magnetic properties. When the magnetic field is small, the magnetic susceptibility of the bead can be approximated as being constant. When the magnetic field increases, the magnetic moment saturates very quickly.

2.1.3 Magnetic Force and Torque

In a non-uniform magnetic field, a magnetic force can be applied on a magnetic bead. This magnetic force obeys [85]

$$\mathbf{F} = (\mathbf{m} \cdot \nabla) \mathbf{B} \quad (2.6),$$

where \mathbf{B} is the magnetic flux density and \mathbf{m} is the magnetic moment of the bead. As in Eq. (2.6), the force is proportional to the magnetic moment of the bead and to the magnetic field gradient at the

bead's position. Superparamagnetic particles, which do not agglomerate in absence of an external magnetic field, are usually adopted as probes in magnetic tweezers because the ensuing magnetic force is independent of the magnetization history due to the absence of hysteresis.

When the particle's magnetic moment is not parallel to the magnetic field, a torque is acting on the particle which can be described as

$$\boldsymbol{\tau} = \mathbf{m} \times \mathbf{B} \quad (2.7).$$

In order to obtain a high torque, ferromagnetic particles with high remanence are usually adopted in magnetic twisting cytometry.

As in Eq. 2.6 and 2.7, both the magnetic force and the torque depend on the magnetic moment of the particle. In order to obtain a high magnetic moment, so-called microbeads with sizes in the μm range are usually synthesized from many small particles, so that the properties such as superparamagnetism and high remanence can be retained. The total magnetic moment of each bead equals the sum of the individual particles' moments. The small particles can be assembled around a polymer core or embedded in a non-magnetic matrix, as depicted in Fig. 2.4. The coating layer is used to protect the magnetic material and to facilitate functionalization of the beads [58].

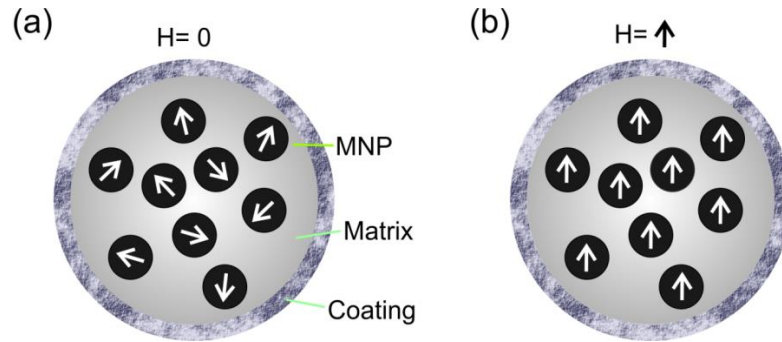


Fig. 2.4. Magnetic microbead. (a) $H=0$, (b) $H \neq 0$.

2.1.4 Magnetic Field Generation

Usually, there are two methods to generate a magnetic field. One method is using a permanent magnet, which is simple and easy to implement. However, the disadvantage of this method is its awkward maneuverability, which is limited by the mechanical actuation. The other method is using electromagnets, of which the magnetic field can be controlled by the coil current. In absence of a magnetic yoke, the magnetic field generated by a typical coil is weak. A high coil current could generate too much heat. Hence, materials with high permeability are usually adopted to enhance, transport, and concentrate magnetic flux from an electromagnet to the area of interest. When the magnetic flux is confined to a well-defined path like circular closed yoke, a law analogous to Ohm's law can be used in the magnetic circuit as in the electric circuit. Applying Ampere's law to the path of magnetic circuit gives [83]

$$NI = \oint H dl \quad (2.8).$$

Here the parameter NI , which is measured in Ampere turns, can be viewed as the magnetomotive force (MMF). The magnetic flux arising in the yoke is proportional to the MMF. With Eq. 2.3 and the magnetic flux definition

$$\Phi = BA \quad (2.9),$$

Eq. 2.8 can be written as

$$NI = \Phi \mathfrak{R} \quad (2.10a).$$

Here,

$$\mathfrak{R} = \int \frac{dl}{A\mu_r\mu_0} \quad (2.10b)$$

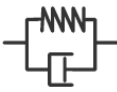

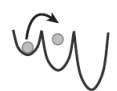
is the magnetic reluctance of the magnetic circuit. The reluctance depends on the cross section area (A), the magnetic permeability (μ_r) and length of the yoke, which is similar to the resistance of the conducting wire in an electric circuit. Compared to air, the soft magnetic materials (high μ_r) usually own much lower reluctance. Hence, in order to achieve a high magnetic field with a low coil current, a small air gap and a material with high permeability are beneficial. However, as mentioned in the section 2.1.1, there is nonlinear hysteresis in ferromagnetic materials. It is well known that the linearity of response is very important for the performance of any actuator [92]. Therefore, in order to reduce the nonlinearity of the magnetic system, both a material with a high permeability and an appropriate air gap are usually adopted. The high reluctance in the air gap balances out the nonlinearity of the material in the total reluctance.

In practice, except in some special situations, the magnetic flux in most magnetic systems is not well confined to the specific path. There are non-negligible flux leakages in these magnetic systems. Moreover, when the magnetic field in the yoke approaches high fields, magnetization saturation is occurring in the material. Therefore, accurate results cannot be obtained with the previous simple approximations. As a prevalent numerical technique, the finite element method (FEM) is very appropriate for problems with complicated geometries and material properties. In FEM, the system is subdivided to different domains, which can be designated with different properties, for example the B - H relation for magnetic materials [93]. Each domain is composed of many smaller bodies or units (finite elements). With special boundary values, the partial differential equations of the interesting variables can be approximately solved by minimizing the associated error functions [94].

2.2 Cell Mechanics Models

There are a number of theoretical models that have been developed to describe and to predict the mechanical properties of cells. However, no single model available to date can describe all the mechanical behaviors of cells [95]. In general, there are two fundamental types of models: the bottom-up and the top-down models. The bottom-up models compose the complex material (such as the cell) from simple elementary subunits (such as actin, microtubule, and intermediate filament) [96]. It is well known that the cytoskeleton of a cell is composed of cross-linked networks of semiflexible filaments. For example, the worm-like chain model attributes the elasticity of a semiflexible polymer to the entropy of the chain, in which a resistance force is generated upon stretching because the number of available conformations and therefore the entropy are reduced [95, 97]. On the other hand, the constitutive properties of cells can also be described with phenomenological top-down models, which are independent of the details of the microscopic structures of cells. Several common top-down models are listed in Table 2.2.

Table 2.2. Top-down models of cell mechanics (Modified from Ref. [95])

Model	Concept	Stress stiffening	Power-law rheology	Stress dependent exponent	
	Linear viscoelasticity	Equivalent circuit of elastic springs and viscous dashpots	No	Requires a large number of elements	No
	Tensegrity	Prestressed structure made of stiff rods and tensed cables	Stiffness proportional to prestress and external stress	No	No
	Soft glassy rheology	Elastic elements hopping between energy traps, effective noise temperature	No (softening at high stress)	Yes	Fluidization with stress

In the linear viscoelasticity model, the cells are intuitively simulated as mechanical systems which are composed of springs and dashpots. Although only few elements are used, the response from various cells can be fitted to this model very well [28, 29, 53]. For example, the creep compliance of a simple viscoelasticity model, which consists of a Voigt body and a dashpot in series (as depicted in the inset figure of Fig. 4.21 (d)), can be described with

$$J(t) = \frac{1 - e^{-t/\tau}}{\mu} + \frac{t}{\eta_0} \quad (2.11),$$

where

$$J(t) = g \frac{d(t)}{F} \quad (2.12).$$

Here μ and η_0 are the elastic and viscous coefficients of spring and dashpot, respectively. The relaxation time τ equals η_0/μ . The parameter g in Eq. 2.12 is a geometric factor which depends on the radius of the probe:

$$g = 6\pi r \quad (2.13).$$

In the viscoelasticity model, there are characteristic response time constants which depend on the specific coefficients of spring and dashpot elements. However, there are a number of observations that the creep responses of cells obviously deviate from the predictions of the viscoelasticity model, especially during the very short initial time [26, 98]. Moreover, the cell responses usually follow the power-law relaxation in frequency or time domain, which actually correspond to a lack of characteristic relaxation times [26, 30, 32]. This power-law behavior can be deduced from the soft glassy rheology (SGR) model, which was developed to describe the rheology of soft materials like slurries or foams [99]. In these soft glassy materials, the main characteristics are structural disorder and metastability, and the thermal motions of elements are not sufficient to achieve structural relaxation. In addition to the highly complex and heterogeneous structures inside a cell, there are also a number of nonlinear “glassy” characteristics such as aging and rejuvenation, which have been observed in cells [39, 100]. With the SGR model, both the creep and the frequency responses of cells can be well described. For example, the creep of a cell upon a stress usually follows

$$J(t) = J_0 \left(\frac{t}{t_0} \right)^\beta \quad (2.14),$$

where J refers to the creep compliance, which can be determined from the bead displacement as in Eq. 2.12. But here the geometrical factor $g = \pi r$ is adopted, r is the radius of bead, as in Ref. [101]. In Eq. 2.14, the time is arbitrarily normalized to $t_0 = 1$ s to get a dimensionless exponent. Therefore, there are only two free parameters J_0 and β in the model. $1/J_0$ can be assumed as a measure of cell stiffness. The power-law exponent can be interpreted as the viscoelastic state of the cell between a purely elastic solid ($\beta=0$) and a purely viscous fluid ($\beta=1$) [101]. On the other hand, in the frequency regime, the complex elastic moduli of cells obey [30, 31]

$$\tilde{G}(\omega) = G_0 \left(\frac{\omega}{\Phi_0} \right)^{x-1} (1 + i\eta) \Gamma(2-x) \cos \frac{\pi}{2}(x-1) + i\omega\mu \quad (2.15).$$

G_0 and Φ_0 are scale factors, ω is the angular frequency. The parameter η is a structural damping coefficient,

$$\eta = \frac{\tan(x-1)\pi}{2} \quad (2.16).$$

In Eq. 2.15 and Eq. 2.16, x and μ are the power-law exponent and the viscosity, respectively. The power-law exponent ($x-1$), similar as the β in Eq. 2.14, reflects the intracellular agitation, which

describes the transition from solidlike ($x=2$) to fluidlike ($x=1$) behavior. This exponent x is also expressed as the noise temperature.

However, the SGR model cannot explain the stress stiffening behavior in cells. There are active contractile components like myosin motors in cells, which can generate a tension force in cytoskeletal filaments. With the tensegrity model, which is adapted from architecture, both the internal prestress enhancement and the externally applied stress can justify the stiffness increase in cells [45, 102, 103].

3. Materials and Methods

In this chapter, the basic methods and techniques adopted and developed for this work will be discussed. First, the MT/MTC setup including system configuration, magnetic actuator, electronics, particles tracking algorithm and so on, will be described in detail. Then the cell culture and related biology experiments will be presented. The work described in this chapter has been published in Refs. [104, 105].

3.1 Magnetic Microrheometry System

3.1.1 System Configuration

The MT/MTC prototypes and bio-experiment setups developed within this work are shown in Fig. 3.1 (a) and (b), respectively. The customized magnetic actuation system includes a main hexapole magnetic yoke, a fluidic reservoir, and a group of actuating coils, as presented in Fig. 3.1 (a) and (b). The main yoke and fluidic reservoir form a closed magnetic circuit. In MT and MTC modes, the configurations of fluidic reservoirs are different, as seen in Fig. 3.1 (c). The tips in a MT fluidic reservoir symmetrically enclose a small workspace where samples are located. Usually, there are no magnetic tips needed in MTC. The main components of the prototype and bio-experiment setups are listed in Table 3.1. In the prototype setup, an objective (Plan Apo S 3.5× mono, Carl Zeiss AG, Germany) with far working distance (FWD 16 mm) was used with a stereo microscope (SterEO Discovery V8, Carl Zeiss AG, Germany). A high-speed monochrome CMOS (MQ042MG-CM, XIMEA GmbH, Germany) camera was attached to detect the magnetic particle. For the bio-experiment setup, in order to achieve good resolution, high magnification water immersion objective (W Plan-Apochromat 63× (40×) /1.0 VIS-IR, Carl Zeiss AG, Germany) mounted on an upright microscope (Axio Scope.A1, Carl Zeiss AG, Germany) was used. The fluorescence and bright field images of the cells were captured using an ultra-low noise sCMOS camera (Zyla 5.5, Andor Technology Ltd., UK). The light from a LED cold-light source (CL 6000 LED, Carl Zeiss AG, Germany) was used to illuminate the workspace by an optical fiber from the bottom of the fluidic reservoir. With this, the heat contribution from light on the fluid cell was reduced, especially at high light intensity. The magnetic actuator was mounted onto an XY and a Z stage (M-406 and MVN50, Newport Corporation, USA). A multifunction RIO card with an embedded FPGA (PCIe-7841R, National Instruments Corporation, USA) and a DAQ card (USB-6259, National Instruments Corporation, USA) were used to achieve input and output between computer and devices. The computers were equipped with a high performance CPU (Core i7 3770K, Intel Corporation, USA), 32 GB RAM, and LabVIEW (National Instruments, USA) software. In order to supply sufficiently high currents and to conveniently optimize the performance for the specific coils, multi-channel power amplifiers were designed and built. The coils were wound using enameled copper wire with a diameter of 0.5 mm. A multi-channel magnetometer based on hall sensors (A1302, Allegro

MicroSystems, LLC, USA) was developed to measure the magnetic field of the each yoke pole. In order to improve heat dissipation, passive heat sinks were mounted beneath the coils. A multi-channel thermometer using six Pt100 temperature sensors was set up to individually monitor the temperature of each coil. The system block diagram of MT is shown in Fig. 3.1 (d). As the main part of system, the feedback loop sketched in red was used to actuate magnetic beads. Accordingly, a similar block diagram of MTC is given in Fig. 4.16. The details of each part of the system will be presented in the following sections.

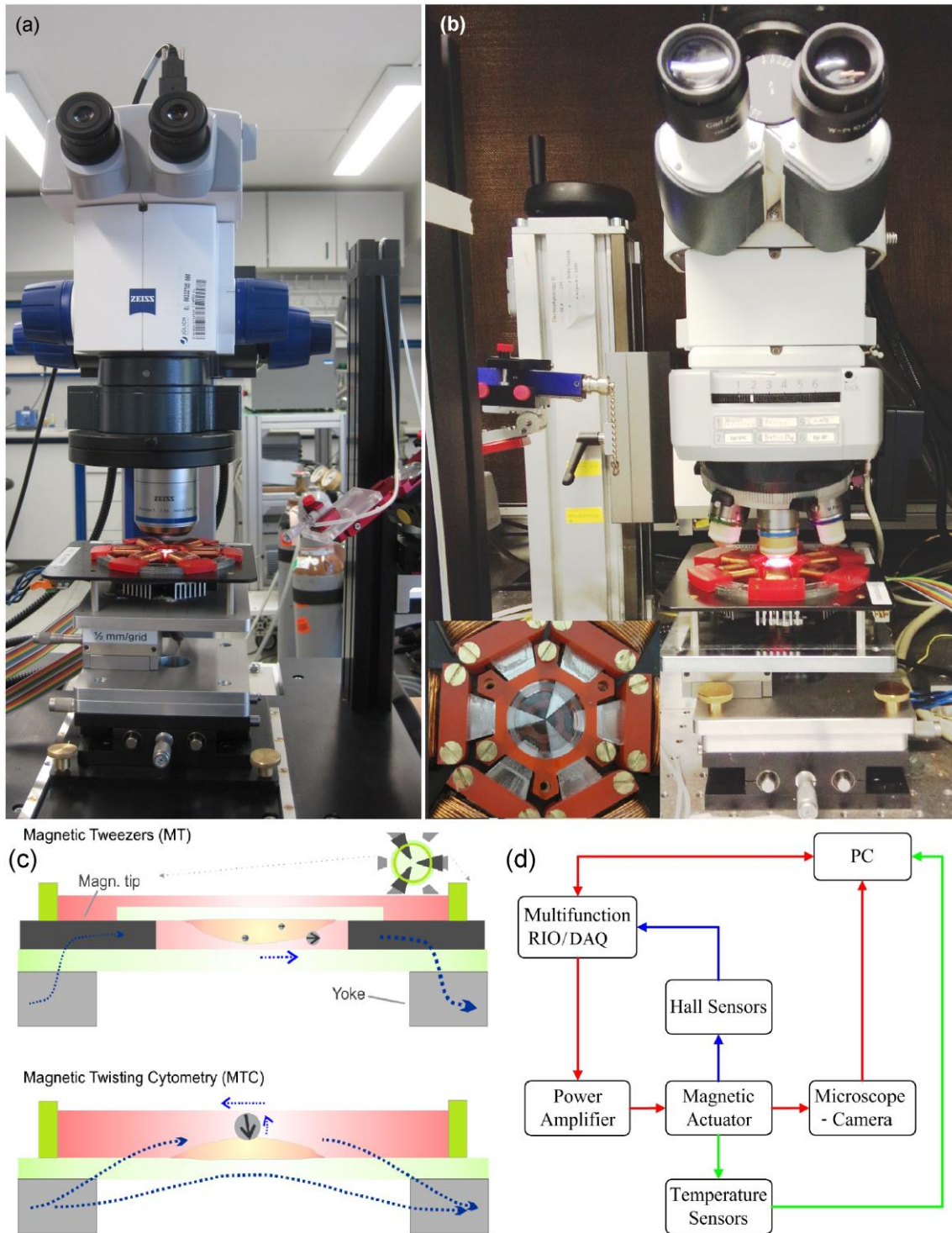


Fig. 3.1. (a) Prototype setup. (b) Bio-experiment setup. Inset: top view of the central area of the main yoke, on which there is a fluidic reservoir for MT. (c) Schematics of MT and MTC. (d) Block diagram of the MT system. (Adapted from [104]).

Table 3.1 Main components of the prototype and bio-experiment setups

Items	Prototype setup	Bio-experiment setup
Microscope	Stereo microscope: SteREO Discovery V8	Upright microscope: Axio Scope. A1
Objective	Plan Apo S 3.5× mono	W Plan-Apochromat 63× (40×) /1.0 VIS-IR
Camera	CMOS: MQ042MG-CM	sCMOS: Zyla 5.5
Magnetic actuator	Share	Share
Power amplifier	Power amplifier II with transformer power supply	Power amplifier II with primary switched power supply
Magnetometer	Share	Share
Input /Output	PCIe-7841R (share) and USB-6259	PCIe-7841R (share) and USB-6259
Computer	i7 3770K, 32 GB RAM, 32-bit LabView	i7 3770K, 32 GB RAM, 64-bit LabView

3.1.2 Magnetic Actuator

As mentioned in the section 2.1.4, the coils of main yoke serve as the magnetomotive source of the magnetic circuit. The magnetic tips in the fluidic reservoir are used to conduct and concentrate the magnetic flux into the workspace. All of the main yoke parts and tips in the fluidic reservoir were cut by laser to form the designed geometry, and then were annealed under dry hydrogen atmosphere (manufactured by SEKELS GmbH, Germany).

The main hexapole yoke is composed of 10 layers of 0.5 mm thick laminated magnetic parts (PERMENORM[®] 5000 H2, Vacuumschmelze GmbH & Co. KG, Germany), as shown in Fig. 3.2 (a) - (b). This soft magnetic material has a very small hysteresis, a high permeability in a wide magnetization range, and a high saturation field of 1.55 T. These magnetic parts were isolated by a thin layer of varnish (MR8008, Electrobule, UK). The coating processes were performed as follows: 1) dip the clean yoke sub-units into the varnish; 2) withdraw the coated sub-units slowly with only a small amount of varnish left; 3) let them drain off on a wire racket in air for 2 hours; 4) cure the varnish completely in a 60 °C oven for half a day; 5) remove the bulges of cured varnish. Although this isolation method is convenient and low cost, the final coated films were not very flat, which caused small air gaps between yoke layers. Besides, the cured varnish is vulnerable to dissolution by organic solvents such as acetone and ethanol. As in Fig. 3.2 (b), the yoke layer parts were assembled in an alternate crisscrossing pattern, which helps to enhance the flux conduction. On each magnetic pole of the main yoke, an actuation coil was affixed. Each coil has three taps to be configured with 80, 160, or 240 windings. Each coil has its own Hall probe and temperature sensor. Their installation

positions are indicated as A and B in Fig. 3.2 (c). The optical fiber's installation position is marked as C. The mechanical framework of yoke holder, coil former, and heat sink (on the back side, position D in Fig. 3.2 (c)) were all fabricated from aluminum alloy and were subsequently anodized. The yoke was fixed by plastic clamps. Underneath the yoke holder, there are the sockets for amplifier and sensor connectors, as seen in Fig. 3.2 (d). All of these modules are replaceable.

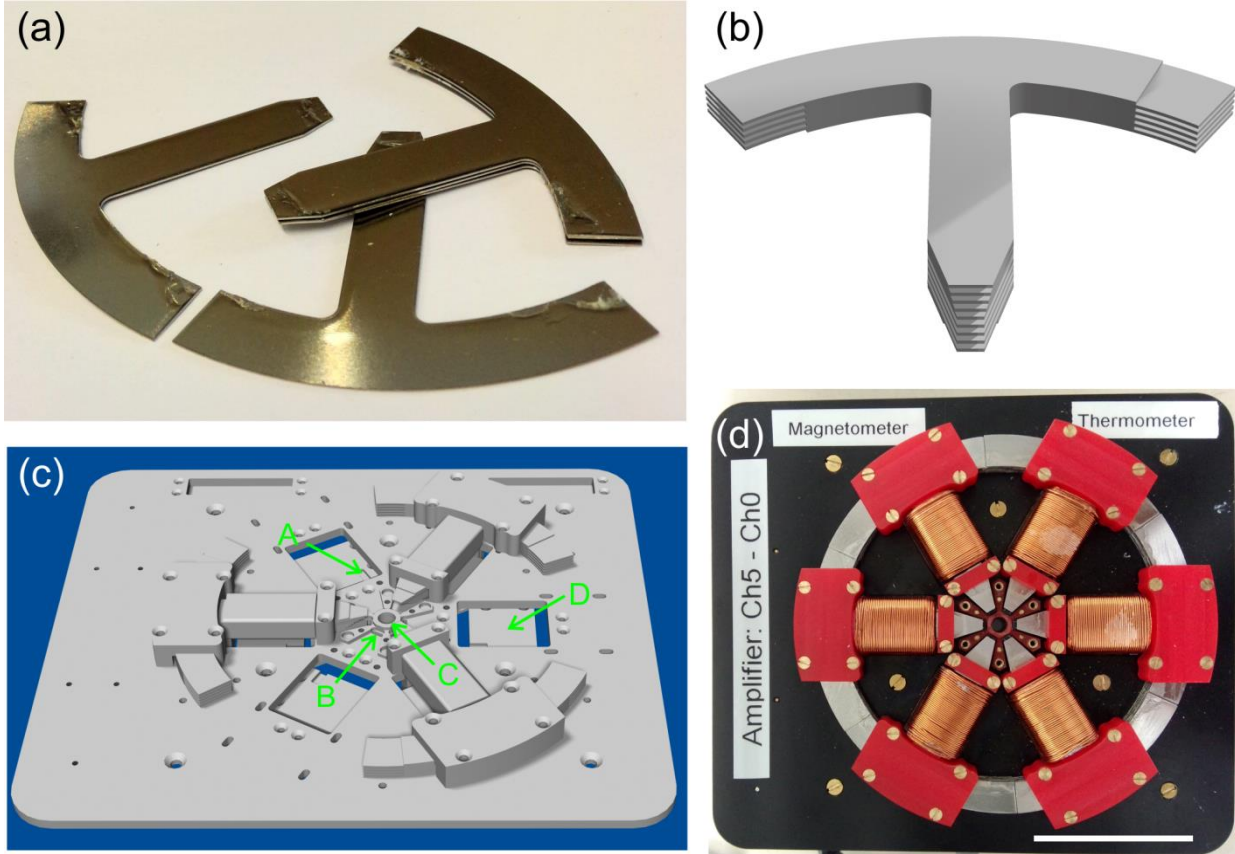


Fig. 3.2. (a) Main yoke sub-unit. (b) CAD drawing of one pole of the yoke, assembled from 10 pieces, bottom view. (c) The CAD drawing of the actuator. (d) Photograph of the actuator. Scale bar is 50 mm.

The small fluidic reservoir can be installed directly on the central area of main yoke poles with a specific plastic holder, as shown in Fig. 3.1 (b). In order to obtain a high magnetic field, the FeCo-V alloy VACOFLUX[®] 50 (Vacuumschmelze GmbH & Co. KG, Germany) was used for the magnetic tips in the fluidic reservoir, which has a very high saturation field of 2.33 T. The distance among tips was a design variable, determined by the trade-off among the dimension of workspace, maximum amplitude and accuracy of magnetic field (force), and so on. Here, the shapes of all tips are like isosceles trapezoid, and the protrusion angles of the tips were set to around 35° to achieve the maximal magnetic field at workspace center [64]. In order to implement the desired configuration, the individual magnetic tips were firstly aligned and pre-fixed on a circular cover slip under the microscope with a small amount of slowly setting glue, as Fig. 3.3 (a) - (d). In the alignment process of tips, a customized LabVIEW program which can generate auxiliary lines was used, as shown in Fig. 3.3 (e). By a calibration slide, the scales of the imaging systems can be determined. Once the scale was determined, the radius of workspace, width of tip, and rotation angle can be set up within the

software. It is well known that there is a strong magnetostriction effect in FeCo alloys [67]. In order to avoid the emerging of cracks between the tips and the glass cover slip upon application of strong magnetic fields, the glue should not be smeared on the cover slip close to the sharp ends of tips. Besides, after the glue dried out, polydimethylsiloxane (PDMS, Sylgard 184, Dow Corning Corporation, USA) was used to fix a glass ring on the cover slip as a reservoir, see the Fig. 3.3 (f). With the help of capillary force, the PDMS flows to fill the gap between the tips and the cover slip. In order to speed up the curing of the PDMS, the samples can be put in a heating furnace, as shown in Fig. 3.3 (g). After the PDMS cured, the final fluidic reservoirs look like in Fig. 3.3 (h). Thanks to the good elasticity of PDMS, these fluidic reservoirs are durable to high force operation. On the other hand, in MTC, the workspace of fluidic reservoir is usually very large. It is not easy to locate the center of workplace under a high magnification microscope. Thanks to the LabVIEW program and the zoom microscope, a small mark spot can be easily made by a manipulator (Unit MRE / MLE: 3 axes Mini 25, Luigs & Neumann GmbH, Germany) and a micropipette, see the Fig. 3.3 (i). The micropipettes were pulled from glass capillaries (BF150-86-10, Sutter Instrument, USA) by a laser-based pipette puller (P-2000, Sutter Instrument, USA).

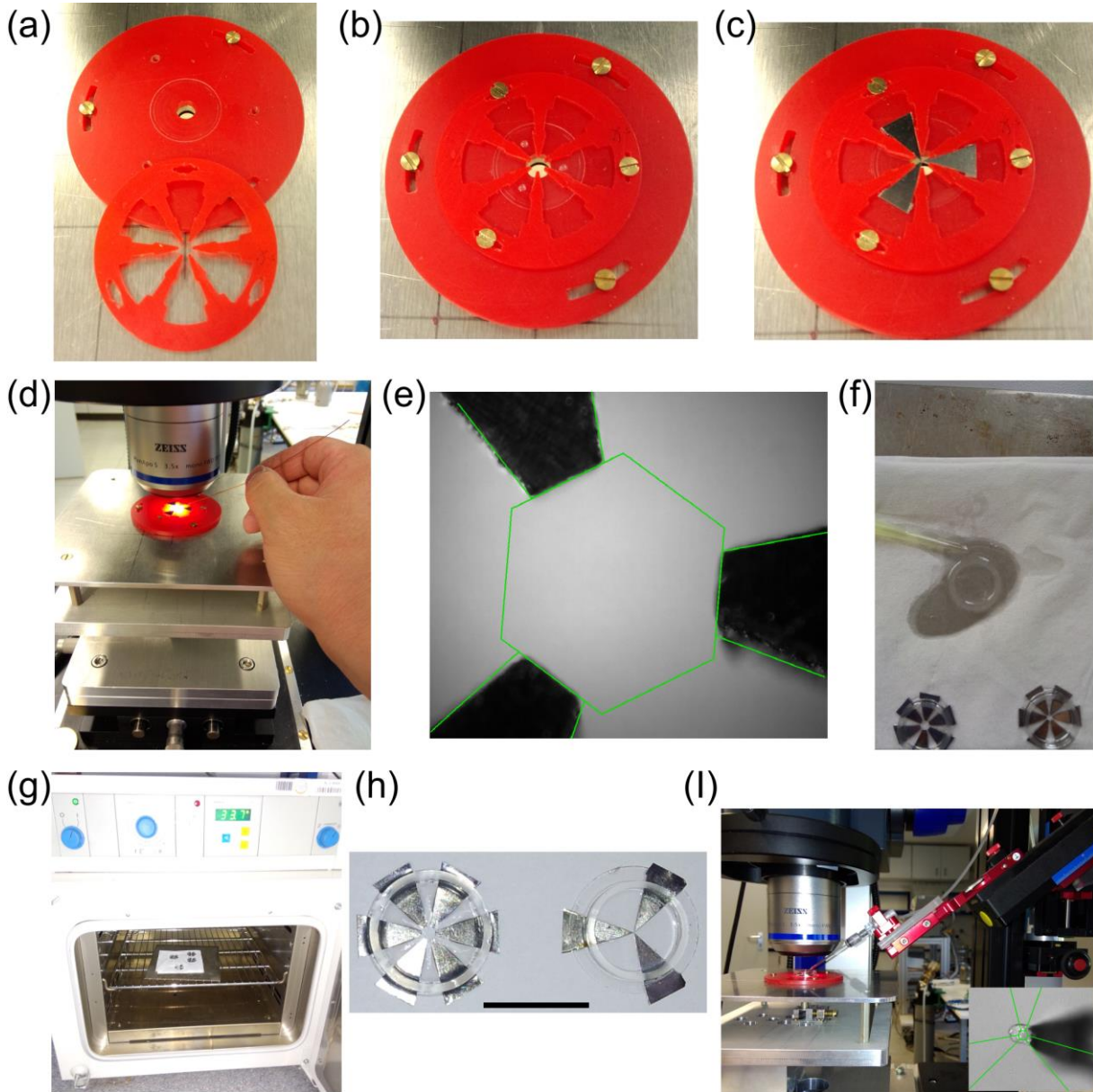


Fig. 3.3. Procedures of fluidic reservoir fabrication. (a) A clear cover slip was put onto the bottom part of a special aligner. (b) The cover slip was fixed by installing the upper part of the aligner. Subsequently, small amount of glue was smeared on the cover slip at each magnetic tip aligning well. (c) Cleaned magnetic tips were set up on the cover slip. (d)- (e) With the help of auxiliary lines in a custom Labview program, the magnetic tips can be adjusted to the defined structure with a thin copper wire under microscope. After 12 hours of the glue setting, the tips were fixed. (f) The glass ring was firstly dipped into PDMS. Then the ring was withdrawn slowly until a small amount of PDMS was left on the ring, and put on the magnetic tips. For 0.5 mm thick tips, usually additional PDMS was needed to mend the gap between the cover slip and glass ring. (g) The fluidic reservoirs were put into an oven to cure the PDMS at 110 °C for two hours. (h) Fluidic reservoirs with 6 and 3 tips. Scale bar 15 mm. (i) For the fluidic reservoir used in MTC, a mark spot can be made by a micropipette with a small amount of glue on its tip, which can facilitate locating the workspace center.

3.1.3 Electronics

As mentioned in the theory part 2.1.3, the applied magnetic force or torque on beads are dependent on the magnetic field. Therefore, the electronics for magnetic field generation is very important for the performance of magnetic particle actuation. Due to the high permeability of FeNi alloy PERMENORM[®], the main yoke with a coil of 240 turns exhibits a high inductance of 8.86 mH at 100 Hz. When using a normal amplifier to drive such high inductive load, it is very easy to cause

oscillation, and it is not easy to optimize the performance. Therefore, a multi-channel power amplifier and a special power supply were built, as seen in Fig. 3.4 (a). Furthermore, a multi-channel magnetometer based on hall probes and a multi-channel thermometer were built to measure the magnetic flux through the core and to monitor the temperature of the coils, as shown in Fig. 3.4 (b).



Fig. 3.4. (a) The power amplifier II. Top: amplifier, bottom: bipolar DC power supply. (b) Thermometer and magnetometer.

The prototype amplifier circuit and its transfer function model are shown in Fig. 3.5. In order to achieve high currents, high power operational amplifiers OPA541 (Texas Instruments Inc., USA), which have a maximum dissipation power of 125 W, were used as the final stage amplifiers. Besides, the high-speed precision operational amplifier OPA602A (Texas Instruments Inc., USA) was employed as voltage-to-current conversion amplifier. In Fig. 3.5 (a), the components R7, R8, C4, and C5 were used as a specific stability compensation circuit for the inductive load (coil). Due to the eddy currents inside the yoke, the inductance of the coil decreases when the frequency goes up, as shown in Fig. A.1 (see Appendix), which was measured by LCR meter (ST2826A, Sourcetric GmbH, Germany). At around 300 kHz, there is a sharp drop in inductance and the dissipation factor increases at the same time. However, for the sake of simplicity, the coil was modeled as a network including a capacitor CC, a resistor CR, and an inductor CL, see the Fig. 3.5 (a). Moreover, the operational amplifiers were approximated as linear components with a single pole, see Fig. 3.5 (b). The transfer function model was established and calculated using Matlab/Simulink (MathWorks, Inc., USA).

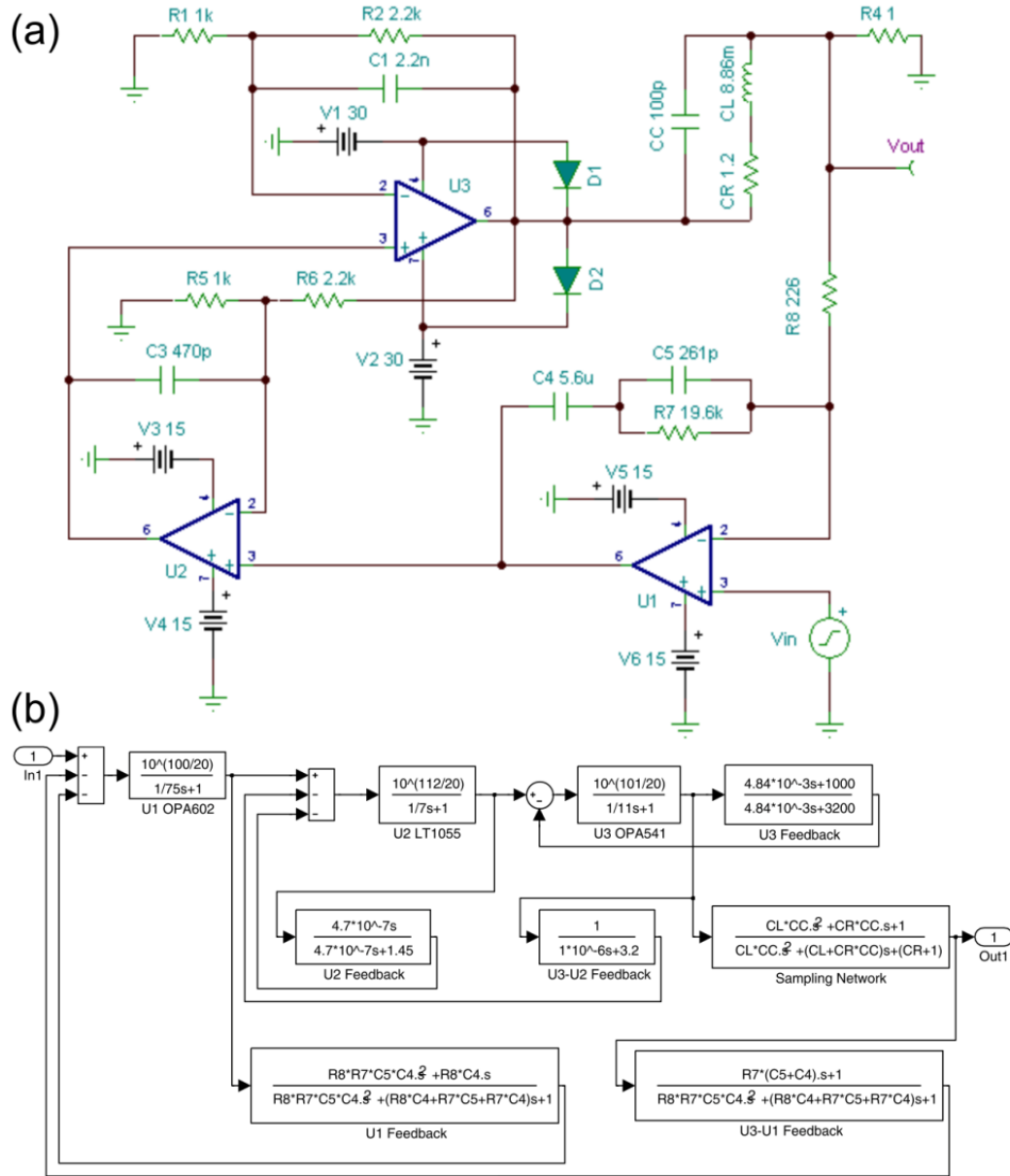


Fig. 3.5. (a) The prototype amplifier circuit, and (b) its transfer function model.

With the help of a Genetic Algorithm toolbox [106], the performances of the circuit were optimized according to

$$fitness = \left(1 - e^{-\frac{gbw}{GBW0}} \right) \left(1 - e^{-\frac{pm}{PM0}} \right) \left(1 - e^{-\frac{st}{ST0}} \right) \left(1 - e^{-\frac{OVSH0}{ovsh}} \right) \quad (3.1).$$

In Eq. 3.1, GBW0, PM0, ST0, OVSH0 are the tuning factors of gain bandwidth, phase margin, settling time, overshoot, respectively. In order to achieve a good performance for each coil configuration (80, 160, and 240 turns), three stability compensation circuits were used. An example of the optimization for 240 turns coil is shown in Fig. A.2. The optimized values of R7, R8, C4, C5 are presented in Fig. 3.5 (a). In experiments, R7, R8, C4, C5 were adjusted around the predicted values, as 47 k Ω , 334 Ω , 4.7 μ F, 33 pF respectively. Besides, two primary switched power supplies of 1200 W each (EXW 24.50 installation unit, Kniel GmbH, Germany) were adopted. With this power supply,

the fluctuation of the current output was limited to less than 1 LSB (Least Significant Bit) of the 16 bit DAC, corresponding to $150 \mu\text{A}$. The amplifier noise curves with different power supply configurations are presented in Fig. A.3.

The experimental step responses of current and magnetic field upon an input signal of 1 V are shown in Fig. 3.6 (a). The rise time of the current is less than $50 \mu\text{s}$ for the low inductance coil (80 turns, I_{LI}) and $200 \mu\text{s}$ for the high inductance coil (240 turns, I_{HI}). The maximum overshoot is less than 10%. All of these signals were acquired synchronously by the DAQ card at 100 kHz. The frequency response is presented in Fig. 3 (b), which was measured by a dynamic signal analyzer (HP 35670A, Hewlett Packard, USA). The bandwidth is 22.4 kHz for the low inductance coil and 10.4 kHz for the high inductance coil. The respective phase margins are 72.6° and 70° . It is obvious that the experimental results of the high inductance coil are very close to the results of the simulation, as seen in Fig. A.2.

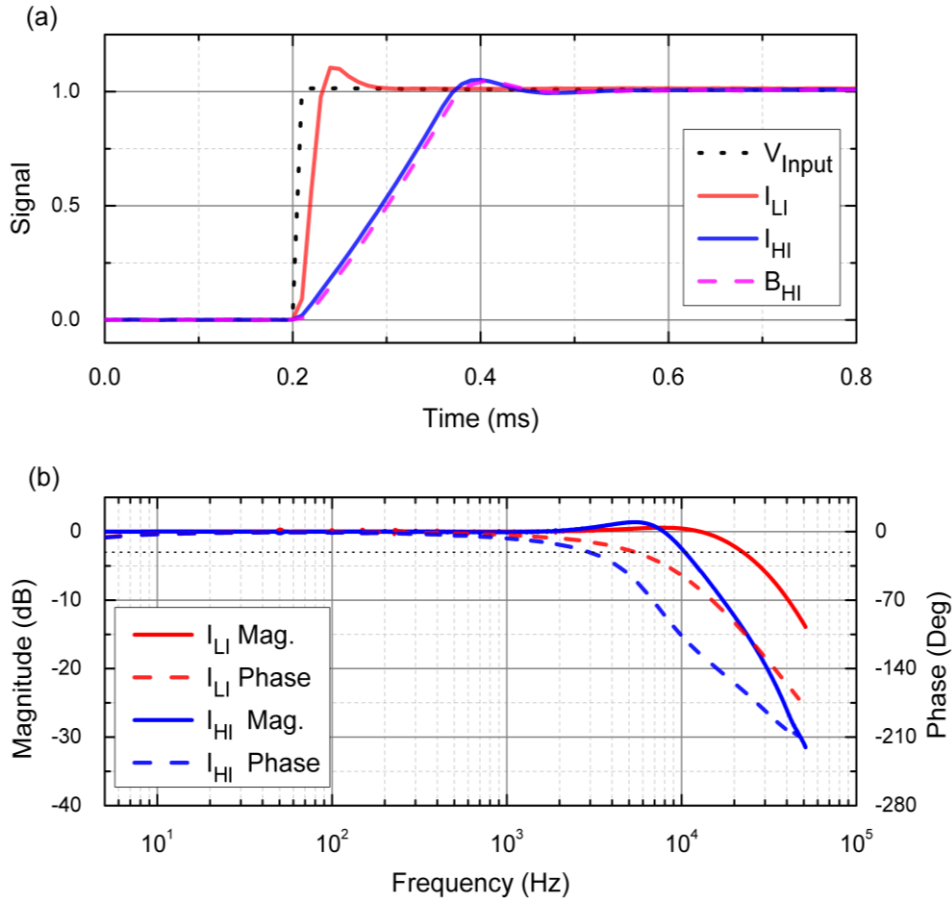


FIG. 3.6. (a) Step response of coil current and magnetic field at low inductance (80 turns, LI) and high inductance (240 turns, HI) coil configurations. The input signal voltage is 1 V. For clarity, the current (0.5 A) and the magnetic field (147 Gauss) were normalized to 1. (b) Frequency response of amplifiers at different coil configurations (Adapted from [104]).

As shown in Fig. 3.6 (a), the measured magnetic field follows the coil current very well. The magnetic field step response for the low inductance coils is not shown because it is limited by the bandwidth of the Hall sensors (20 kHz). With these sensors, no hysteresis was observed, which can be ascribed to the low coercivity (3.41 A/m) and high permeability of the yoke material ($\mu_r > 8000$ up to

1 T). Between experiments, the main yoke can be degaussed by applying sinusoidal currents with rotating decaying amplitude, which quench the residual magnetism in every part of the soft-magnetic yoke.

Thanks to the heat sink and the aluminum mechanical framework, even with continuous 4 A current lasting for 10 minutes, the highest temperatures measured at coil, heat sink and fluidic reservoir were 112.5°C, 78.0°C and 35.5°C, as shown in Fig. A.4. Before this measurement, 0.25 ml milli-Q water was put in the fluidic reservoir, and then the temperature sensor was immersed in the water.

3.1.4 Particle Tracking

In order to determine the position and to measure the velocity of micro beads, a video based particle tracking system was implemented, which allows for high flexibility and is easy to use. This system includes high speed digital cameras mounted on the microscopes and image acquisition and analysis software. The CMOS camera in the prototype setup can acquire 90 frames per second (FPS) at the full resolution of 2048×2048 pixel². Speeds as high as 2,000 FPS can be achieved when adopting a small region of interest (ROI) of 100×100 pixel². The speed limiting factor for small ROIs is the rate at which data can be read off the pixel sensor. The image acquisition and analysis software was developed in LabVIEW, and was performed on the CPU. In the live acquisition mode (software trigger), which is the only mode that can be used in feedback control, the sCMOS camera in the bio-experiment setup cannot achieve the same high speed as the camera in the prototype setup. Hence, only the prototype setup was used for feedback control and MT calibration. In order to obtain a good image quality especially at short exposure times, the fluidic reservoir is illuminated with transmitted light and the pixel binning technique was also used if necessary. To address the different application conditions, several position tracking algorithms have been implemented, as given in Table 3.2.

Table 3.2 Particle tracking algorithms (Adapted from [104]).

Algorithm	Speed*	Resolution	Comment
Center of Mass	fast (6520 Hz)	medium	sensitive to image quality
Cross-Correlation (2D XCor)	slow (991 Hz)	high	robust
Optical Flow Based	medium (4397 Hz)	high	multi-object tracking

* The speed values are given as typical values for single bead tracking with an image size of 200×200 pixel², the size of 2D XCor template image is 30×30 pixel², and the search window of optical flow algorithm is 30×30 pixel². The 2D XCor tested is based on the built-in subprogram, computing in parallel.

In the center of mass (COM) algorithm, the profile of the micro bead was detected based on the weighted pixel value. If the background is very clean, the parameter free Eq. 3.2 can be used. Here just the formula for x dimension is given, the y dimension is similar. In order to extend the dynamic range, the pixels were normalized before calculating. However, if there are some interference spots near the bead, as seen in Fig. 3.7 (a): i, it will cause a deviation in the result. When there is an obvious difference in brightness between the bead and the background, a threshold based filter such as Eq. 3.3

can be used. As shown in Fig. 3.7 (a): ii-iii, the threshold filter works like a mask, only the pixels within the mask are included in calculation. Because of the simple calculation, this method is very fast, see Table 3.2, and can be easily implemented with hardware like FPGA. However, this method can only be used for good optical conditions with a clear contrast between particle and background. The threshold value also has some effects on the tracking results [107].

$$x = \frac{\sum_{i,j} i \cdot \left((P_{i,j} - \overline{P_{i,j}})^2 - \overline{(P_{i,j} - \overline{P_{i,j}})^2} \right)}{\sum_{i,j} \left((P_{i,j} - \overline{P_{i,j}})^2 - \overline{(P_{i,j} - \overline{P_{i,j}})^2} \right)} \quad (3.2)$$

$$x = \frac{\sum_{i,j} i \cdot P_{i,j}}{\sum_{i,j} P_{i,j}}, \quad (P_{i,j} \leq P_{threshold}) \quad (3.3)$$

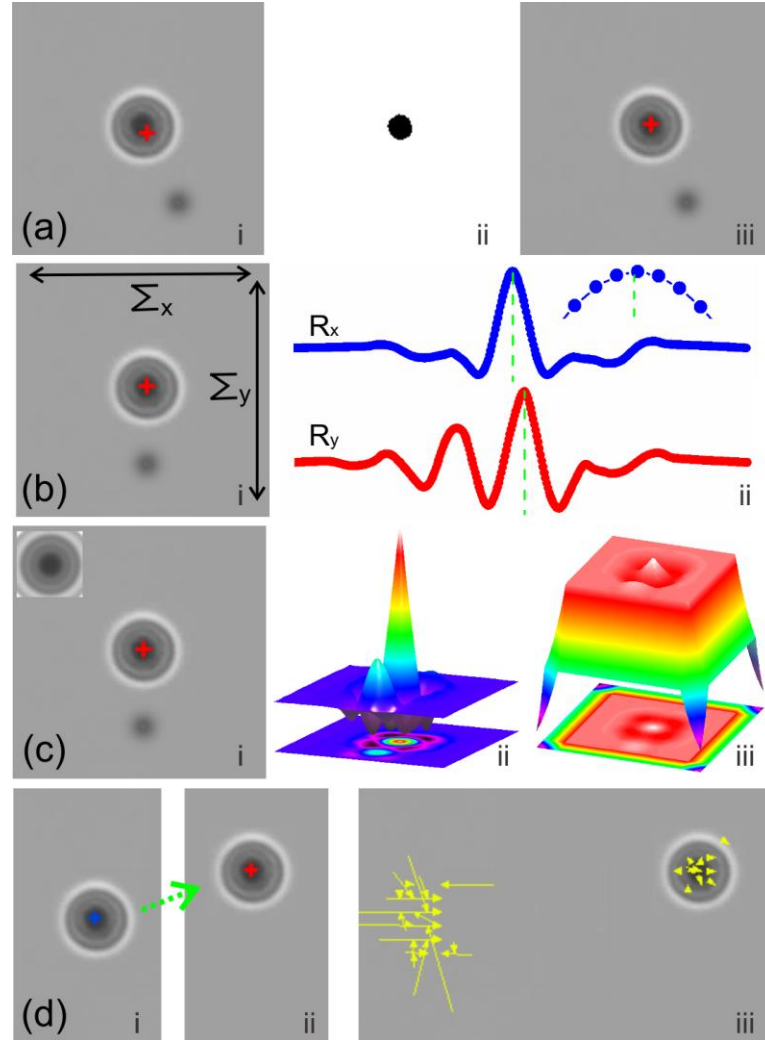


FIG. 3.7. (a) Center of mass. i: result of parameter free method, ii: extracted mask (threshold: pixel intensity = 90), iii: result of threshold based method. (b) 1D cross-correlation. i: summarize the pixels in x and y dimension respectively, ii: self cross-correlation, inset shows the polynomial fitting. (c) 2D cross-correlation. i: particle image and particle template, ii: normalized 2D XCor, iii: Labview embedded 2D XCor. (d) Optical flow. i: previous position, ii: current position, iii: optical flow velocity field.

Due to its robustness against brightness variations and noise, normalized cross-correlation (XCor) has found numerous applications in image processing, such as pattern recognition and template

matching. In general, the NCC is more robust and has a higher resolution than COM [107, 108]. In the situation with a good signal-to-noise ratio (SNR), 1D XCor can be adopted because of the circular symmetry of the bead, as in Eq. 3.4. The pixels are firstly summarized in x or y direction, as seen in Fig. 3.7 (b): i. Then the cross-correlation $R(h)$ is calculated between the each pixel array and its inverse array [63]. As in Eq. 3.4, the exact position in x or y direction is determined by fitting a second-order polynomial using five points around the maximum value in the result. However, when there is a strong noise in the image or some large interference in the background, sometimes the algorithm 1D XCor could not track accurately. In order to address such situation, the 2D XCor algorithm was implemented, as illustrated in Eq. 3.5. The current bead image $P(i, j)$ is cross-correlated with a small template image $T(i', j')$ of the bead, which can effectively eliminate background disturbance [109]. The template image is built by interpolating along radial direction with mean intensity profile along four radial directions $x-$, $x+$, $y-$ and $y+$, as shown in the inset figure in Fig. 3.7 (c): i. Before every experiment, the template image of the bead can be manually selected by an annulus tool. As presented in Fig. 3.7 (c): ii, the output of 2D XCor has a very high peak at the strongest correlation site. Although normalized 2D XCor has a high accuracy and robustness, the computational effort is very high. In order to increase the speed in practice, this algorithm can be implemented directly with the built-in subprogram in Labview (nearly $10\times$ speedup), in which both parallel computing and integer representation (8 bit) are adopted. However, as shown in Fig. 3.7 (c): iii, the correlation peak is not as high as in the original method. This may be caused by the integer representation instead of the double-precision floating-point representation in the customized program.

$$\begin{cases} P^x(i) = \sum_j P_{i,j} - \overline{\sum_j P_{i,j}} \\ R^x(h) = P^x(i) \otimes P^x(i_{\max} - i), \quad h = 0, \dots, 2i_{\max} - 2 \\ x = i_{\max} - \max_{\text{ind}} \langle R^x(h) \rangle / 2 \end{cases} \quad (3.4)$$

$$\begin{cases} P^N(i, j) = \text{Nor}(P(i, j)), T^N(i', j') = \text{Nor}(T(i', j')) \\ R(i'', j'') = T^N(i', j') \otimes P^N(i, j), \quad i'' = 0, \dots, i_{\max} - i'_{\max} - 1, j'' = 0, \dots, j_{\max} - j'_{\max} - 1 \\ x, y = \max_{\text{ind}} \langle R(i'', j'') \rangle \end{cases} \quad (3.5)$$

The optical flow (OF) method [110], as depicted in Fig. 3.7 (d), is widely used in motion detection applications. It is easy to track multiple objects even when they overlap on the image. However, the resolution of this algorithm is low, and the absolute error will accumulate continuously. In order to combine the advantages of OF and XCor, a multi-particle tracking algorithm was customized, as shown in Fig. A. 5. Each frame is first analyzed with OF. Then XCor is carried out in a small local area based on the result of OF, which will decrease the interference from the particle's nearby background and enhance the speed. Finally, the XCor result is taken as the actual position of the bead, which is also used to update its initial position in the OF algorithm for the next frame.

The resolutions of these tracking algorithms were benchmarked in the bio-experiment setup with a 63 \times objective and immobilized 2.8 μm beads. Thanks to the high magnification objective and the low noise camera, the 1D XCor algorithm gives the best result, about 3 nm in y direction, as seen in Fig. 3.8 (b). This agrees well with the findings of Ref. [108]. The comparatively large error in x direction can be attributed to disturbances originating from cables and water cooling tubes which induce external vibration noise. Here, the resolution of 2D XCor was reduced because of the integer representation in digitization, and the corresponding crosstalk between x and y dimension. In the bio-experiment setup, the tracking algorithm OF-1D XCor can be used in most situations, which combines the advantages of high speed, high resolution and multi-particle tracking. For the prototype setup, the 2D XCor algorithm was frequently used because of the low quality of optical imaging. In order to shorten the time for particle tracking, a moving sub ROI for single bead tracking was adopted for each algorithm, so that only the pixels in this region are analyzed. In addition, for convenience of post-processing, the images from cameras are compressed into a video.

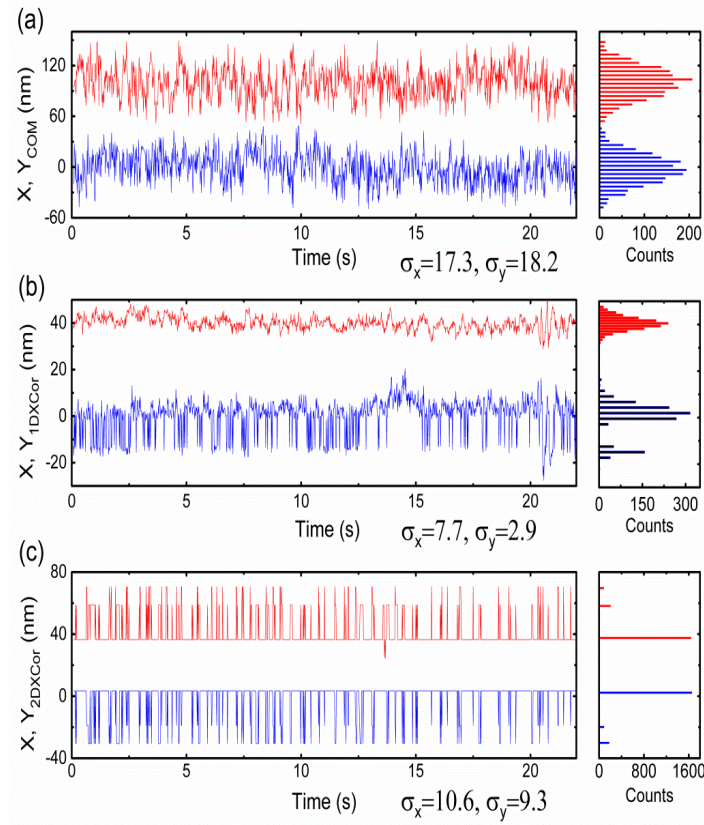


FIG. 3.8. Resolutions of different tracking algorithms. (a) COM parameter free algorithm. (b) 1D XCor algorithm. (c) 2D XCor algorithm based on the built-in subprogram.

3.1.5 Magnetic Field Simulation

Because of the small size of the fluidic reservoir, it is not possible to measure the magnetic field distribution in the workspace. In this work, finite element simulation (COMSOL Multiphysics, Magnetic Fields module, COMSOL Inc., USA) was used to calculate the magnetic field and to model the tip geometry and material effects. The default magnetic insulation boundary condition was applied to the external boundaries. The nonlinear B - H data of magnetic materials were adopted from the

measurement results supplied by the manufacturer, as shown in Fig. A.6. In order to decrease magnetic flux leakage, the sum of all active coil currents was always restricted to zero. The positive coil current was referred to as injecting magnetic flux into the workspace, and vice versa. In order to obtain an accurate distribution of the magnetic field in the workspace, a high density mesh was adopted in simulation, especially for the workspace domain. Typical meshes of 2D and 3D simulation models consisted of 62442 and 2225193 elements, respectively. The geometrical models for the simulations were built according to the real mechanical dimensions. The nonlinear B - I curves were obtained by 2D model simulations. Because of the heavy computational effort, 3D simulations were only carried out for single current values.

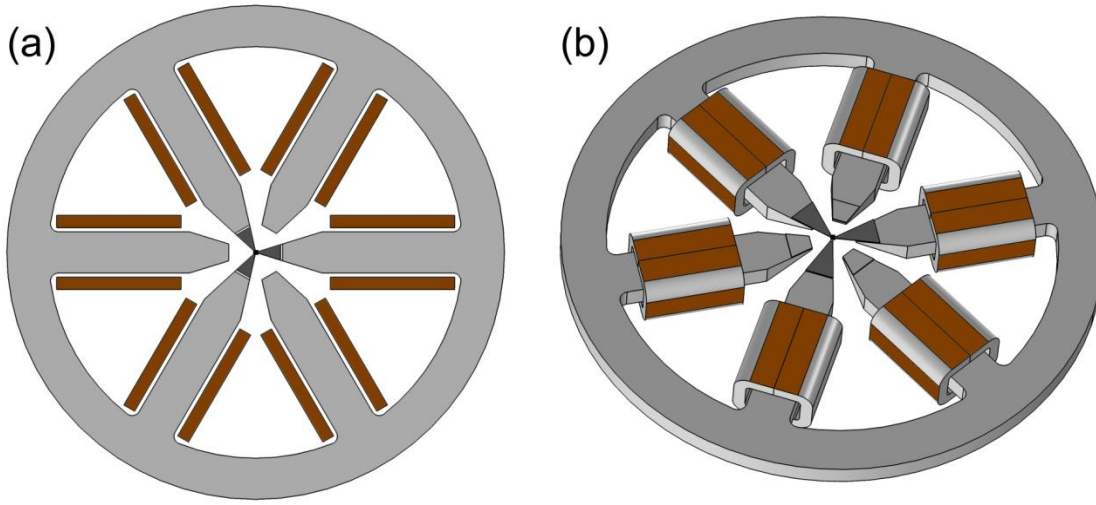


Fig. 3.9. Simulation geometry model. (a) 2D model, (b) 3D model. The main yoke, tips and coils are colorized in light grey, dark grey and brown, respectively.

3.1.6. Inverse Force Model

As mentioned in the introduction chapter, single-pole magnetic tweezers are widely implemented. Because of their simple structure, analytical formulas can be used to accurately model the force distribution [56]. For magnetic tweezers with multiple poles, an approximate model can be applied when the magnetic field and force is small and changes smoothly in the workspace [60, 62]. However, it is difficult to find a simple analytical model for 2D and 3D magnetic tweezers with high force output, because the magnetic force is generally a nonlinear function of position and coil currents. In this work, an inverse force model was developed and calculated based on a numerical solver. With this solver, the coil currents that produce the desired magnetic force can be determined accurately. Firstly, based on the magnetic field simulation, a lookup table (LUT) of coil currents to the magnetic field in the workspace of MT was obtained. Because of the symmetry of magnetic poles, the final magnetic field can be composed by rotating and then superimposing the field generated by each coil current, as in Eq. 3.6

$$\begin{cases} \mathbf{B}_x(x, y) = \sum_p q_p^x(x, y) I_p \\ \frac{\partial \mathbf{B}_x}{\partial x}(x, y) = \sum_p r_p^{x_x}(x, y) I_p \end{cases} \quad (3.6).$$

Here, q_p and r_p are position dependent parameters, and index p is the number of the magnetic pole. In practice, parameters q_p and r_p are adopted as a LUT with $2 \mu\text{m}$ grid spacing. With this LUT, the magnetic field of any position in work space can be bi-linearly interpolated using the four nearest neighbor grid points.

As in Eq. 2.5, the magnetic moment of superparamagnetic beads can be described by a Langevin function. The force components are coupled within this nonlinear function, of which it is difficult to obtain an analytic solution. In order to find a way to compose any desired force vector, a piece-wise linear approximation was adopted to describe $\mathbf{m}(\mathbf{B})$ of the magnetic bead, as in Eq. 3.7

$$\mathbf{m}(|\mathbf{B}(x, y)|) = k_i |\mathbf{B}(x, y)| + b_i, \text{ when } B_i \leq |\mathbf{B}(x, y)| < B_{i+1} \quad (3.7).$$

The space between boundary points B_i is chosen based on the slope change of $\mathbf{m}(\mathbf{B})$. Hence, the accuracy of the piecewise function can be improved easily by increasing the number of pieces. For example, a piecewise function with 18 segments can characterize the magnetization of the bead (Dynabeads[®] M-270 Carboxylic Acid, Thermo Fisher Scientific Inc., USA) very well, as shown in Fig. 3.10. The bead's data supplied by the vendor are quoted as: magnetic susceptibility: $6 \times 10^{-4} \text{ m}^3/\text{kg}$, saturation magnetization: $13 \text{ A} \cdot \text{m}^2/\text{kg}$, density: $1.6 \text{ g}/\text{cm}^3$, diameter: $2.8 \mu\text{m}$. The results of a fit to Langevin function are: $\mu_0 a = 0.021$, $m_s = 2.23 \times 10^{-13} \text{ A} \cdot \text{m}^2$.

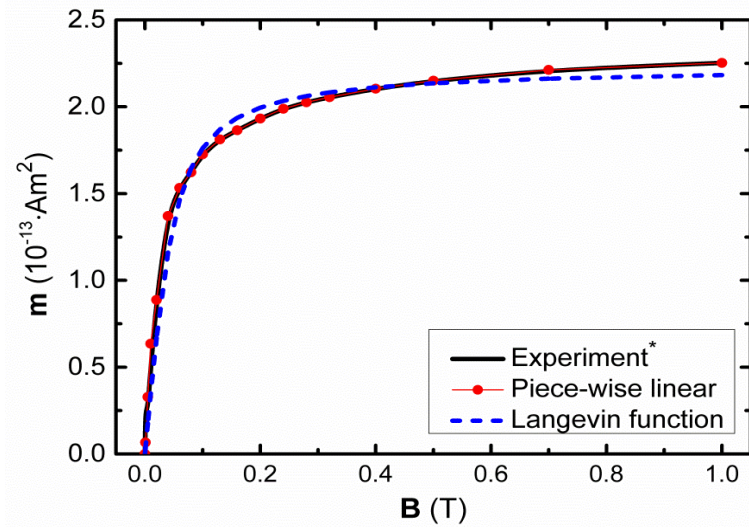


Fig. 3.10. Magnetization of a single M-270 bead. (*The experimental data are quoted from the vendor.) (Adopted from [104].)

By combining Eq. 2.6, Eq. 3.6 and Eq. 3.7, the following force-current formula can be obtained

$$\begin{cases}
 F_x(x, y) = \left(\frac{b_i}{|\mathbf{B}(x, y)|} + k_i \right) \sum_{p, p'} \left(q_p^x(x, y) r_{p'}^{x_x}(x, y) I_p I_{p'} + q_p^y(x, y) r_{p'}^{y_x}(x, y) I_p I_{p'} \right) \\
 F_y(x, y) = \left(\frac{b_i}{|\mathbf{B}(x, y)|} + k_i \right) \sum_{p, p'} \left(q_p^x(x, y) r_{p'}^{x_y}(x, y) I_p I_{p'} + q_p^y(x, y) r_{p'}^{y_y}(x, y) I_p I_{p'} \right) \\
 |\mathbf{B}(x, y)| = \sqrt{B_x(x, y)^2 + B_y(x, y)^2} \\
 \sum_p I_p = 0
 \end{cases} \quad (3.8).$$

Based on Eqs. 3.6 - 3.8, it is easy to solve for the coil currents from a desired force in a recursive way. By iterating through the linear sections starting from the first section with k_0 and b_0 , it is checked if the variable \mathbf{B} resolved from Eq. 3.8 and Eq. 3.6 also satisfies Eq. 3.7. If yes, this result is the solution, if not, the iteration is continued. For quadratic equations, there are usually two solutions. Here, the smaller one was adopted to keep currents as low as possible. Because Eq. 3.6 holds only for very good linearity between B and I , the inverse force model should only be used when no magnetization saturation occurs in the magnetic tips. An example of Matlab script to implement this inverse force model is presented as Script 1 in the Appendix.

3.1.7 Feedback Control

According to Eq. 2.6, the magnetic particles in MT are always attracted towards the magnetic tips where the highest magnetic field is achieved. Hence, there is no stable state at which the particle can stay with constant currents applied. In order to stabilize and control the motion of the magnetic particle, an active feedback controller is essential. With the inverse force model deduced as previous, the force output of magnetic tweezers can be linearized. As a result, the controller design was greatly simplified. The remaining dynamics of the system can thus be handled with a linear controller. In order to decrease the steady state error, a proportional integral (PI) controller was deployed. Using Simulink with trial-and-error design method, the parameters of the PI controller can be determined. Then this continuous controller was converted to a digital controller by using the trapezoid rule [92]. Moreover, when the output of this controller reached some set value, the integrator part was reset to avoid large overshoot (anti-windup) [92]. A schematic of the control loop is shown in Fig. 3.11.

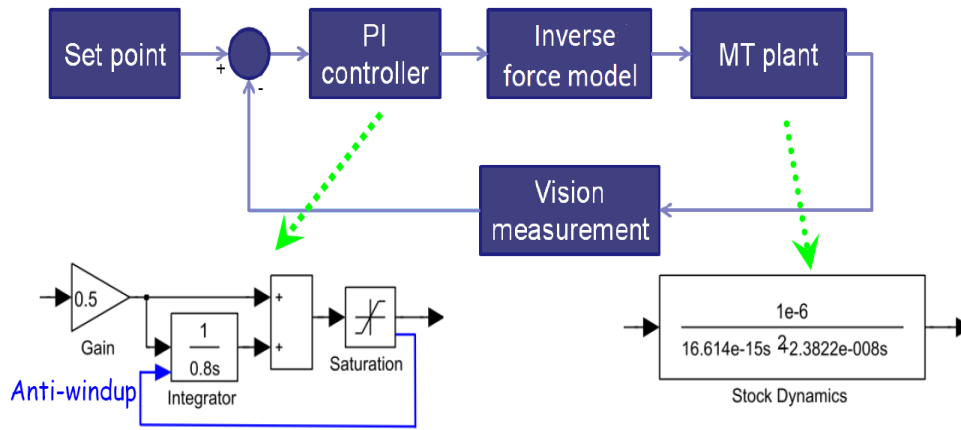


Fig. 3.11. Block diagram of feedback control in MT.

It is well known that in a feedback control loop, the delays of each block play an important role regarding the performance. A detailed analysis on the effect of delay in MT can be found in Refs. [60, 63]. Usually, the speed of the control loop strongly influences the positioning accuracy and maneuverability. Therefore, a multifunction RIO card was adopted with which the output delay from the computer can be decreased to about 20 μ s. The biggest delay in the control loop comes from the camera. Thanks to the high speed of the camera, the fast particle tracking code (COM) and the very low delay of RIO card, the speed of the actual control loop is 303 Hz at a ROI of 600×600 pixel² and 870 Hz at 200×200 pixel². Faster speeds than 1 kHz can be achieved easily by adopting a smaller ROI. A snapshot of the control program is shown in Fig. 3.12.

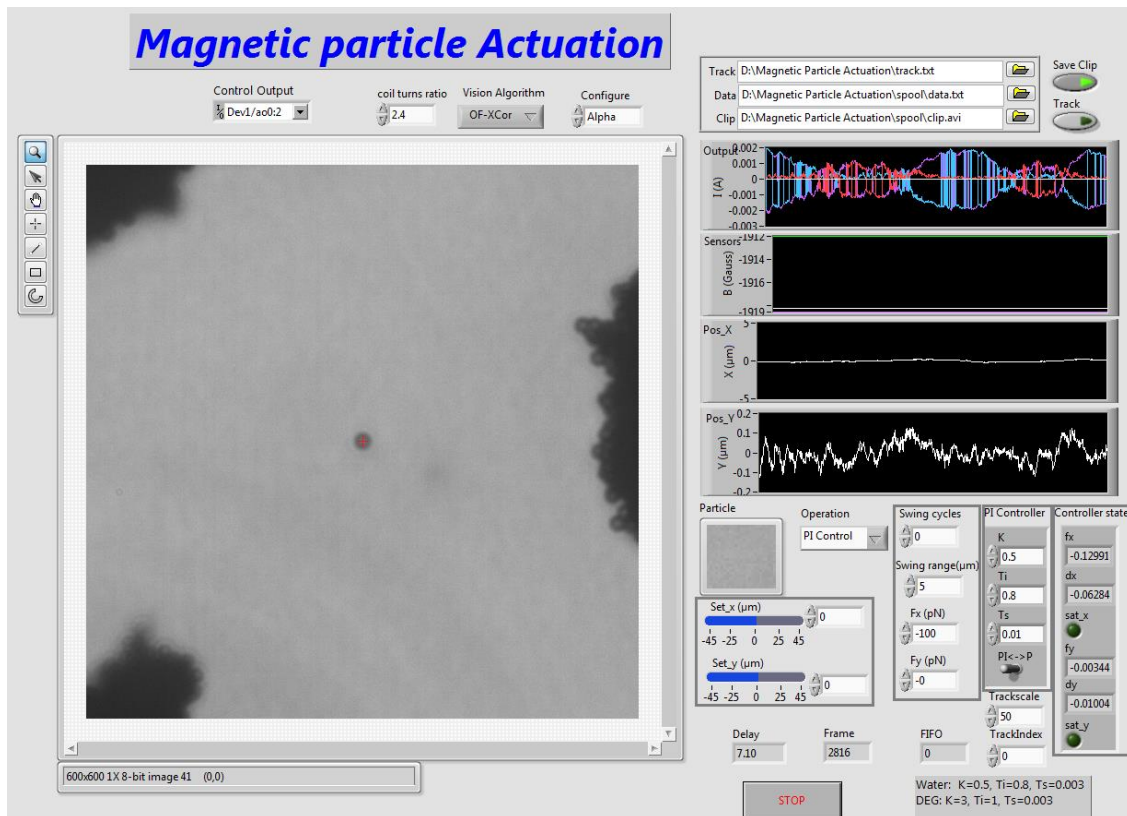


Fig. 3.12. The control program of MT.

3.1.8 Force Calibration

In this work, the magnetic force was calibrated using the classical viscous drag approach. The force was deduced by measuring the motion of bead at a constant coil current. According to Stokes' formula, the force \mathbf{F} on a bead with hydrodynamic radius r , moving with velocity \mathbf{v} in a fluid with viscosity η , is given by

$$\mathbf{F} = 6\pi\eta r\mathbf{v} \quad (3.9).$$

In Newtonian fluid approximation, the viscosity of the fluid can be regarded as a constant. The velocity of a bead moving through a viscous fluid is proportional to the force. In order to achieve high accuracy, the measurements were performed in two fluids with different viscosities. The low viscosity fluid is diethylene glycol (DEG, puriss, 99.0%, Sigma-Aldrich, USA), which was mixed with the magnetic particle solution at a ratio of 200:1. The viscosity of DEG was 31.4 ± 0.16 mPa·s at 23°C, as measured by a viscosity meter (microVISC, RheoSense INC., USA). The high viscosity fluid was made from high concentration glycerol (99.0%, Alfa Aesar GmbH, Germany) mixed with water at a ratio of $\geq 4:1$. The actual viscosity of higher viscous fluid was deduced from the comparison of the bead's speed at the same low force in the low viscosity fluid. Before every experiment, 0.2 ml of these mixing solutions were injected into the fluidic reservoir with a pipette. After 10 minutes of sedimentation, drag experiments were performed. In order to decrease the failure of particle tracking, 2D XCor algorithm was used here [104].

For the force-current calibration, the bead was dragged along the x direction in the central area from $(-15 \mu\text{m}, 0 \mu\text{m})$ to $(15 \mu\text{m}, 0 \mu\text{m})$. Before measurement, the bead was actuated to the start point $(15 \mu\text{m}, 0 \mu\text{m})$ by the PI controller. Then the controller was turned off and the bead was actuated by constant coil currents. The movement of the bead was tracked until the bead arrived at the final border (for example $x=16 \mu\text{m}$). After that, the PI controller was activated and the bead was actuated towards the start point again. Only the motion data between $x= -10 \mu\text{m}$ to $10 \mu\text{m}$ were analyzed. The velocity was deduced by fitting the displacement as a function of time with a linear function. The force acting on the bead during the constant current-on phase was then computed from the velocities based on Eq. 3.9. Similarly, with the help of the controller, the force distributions on a grid in the workspace can be measured very easily, as shown in Fig. 3.13.

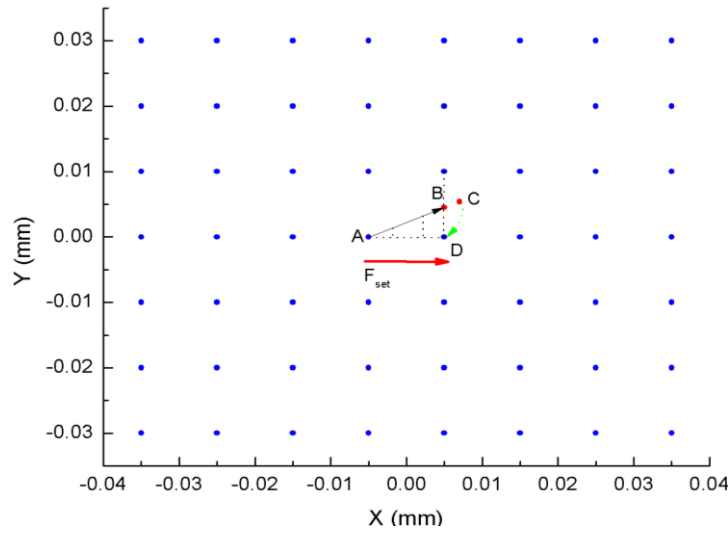


Fig. 3.13 The measurement of force distribution in MT workspace (7×7 , x: from $-30 \mu\text{m}$ to $30 \mu\text{m}$, y: from $-30 \mu\text{m}$ to $30 \mu\text{m}$, each with $10 \mu\text{m}$ step). The force on $(0 \mu\text{m}, 0 \mu\text{m})$ is measured as: firstly the bead was moved to A with the controller; then a force F_{set} was applied on the bead with constant coil currents; the bead may move from A to C actually, not as the set path A - D; finally when the bead approached C, it was pulled back to D with the controller.

3.2 Cell Culture and Experiments

3.2.1 Cardiomyocyte HL-1 cell

The cardiomyocyte-like HL-1 cell line is derived from a mouse atrial cardiomyocyte tumor persisting in culture [111]. When they are mature and reach confluency, these cells exhibit the essential characteristics of adult cardiomyocytes such as spontaneous electric activity and mechanical contraction. Hence, HL-1 cells have been widely used for studies of structure, function and pathology of cardiac muscle cells [112]. According to Ref. [113], the HL-1 cells were cultured as follows: a maintenance culture was kept at 37°C and 5% CO_2 in a T25 tissue-culture plastic flask. The medium was usually exchanged with fresh warm medium daily. The standard culture medium consists of Claycomb's medium (Sigma-Aldrich, USA) supplemented with 10% fetal bovine serum (FBS), $100 \mu\text{g/mL}$ Penicillin, $100 \mu\text{g/mL}$ Streptomycin, 2 mM L-glutamine (all from Life Technologies, USA), and 0.1 mM norepinephrine (Sigma-Aldrich, USA). When the cells grew to confluency, the culture was digested with trypsin/EDTA solution and seeded to a new flask or other culture dish.

Preparation of cell sample for MT experiment

Small cover slips were sterilized with flame before cell seeding. HL-1 cells were cultured on the cover slips for 2-3 days. The nuclei of living cells were stained with 4',6-diamidino-2-phenylindole (DAPI, Sigma-Aldrich, USA). Dynabeads® MyOne Carboxylic Acid beads (Thermo Fisher Scientific Inc., USA) were mixed in advance with cell medium, and kept at 4°C . One night before mechanical measurement, the cells were fed with cell medium which includes both magnetic beads and DAPI. The final concentrations of beads and DAPI in medium were $7\text{-}12 \times 10^6/\text{ml}$ and $10 \mu\text{g}/\text{ml}$, respectively. With the amide bonding reaction of carboxylic acid, the small beads bound to proteins and were easily

endocytosed by the cells. Before the experiment, the cover slip with cells was rinsed with warm phosphate buffered saline (PBS) to remove free beads.

Preparation of cell sample for MTC experiment

Cells were cultured on cover slips like in the MT experiment. The ferromagnetic beads (CFM-40-10, Spherotech, Inc., USA) were coated with 50 $\mu\text{g/mL}$ fibronectin (Sigma-Aldrich, USA) according to the procedure recommended by the manufacturer. Before experiments, the cell culture medium was replaced by warm Dulbecco's Modified Eagle Medium (DMEM, Sigma-Aldrich, USA), in which the coated beads were mixed at a concentration about 2×10^6 beads/mL. After 15 minutes of incubation, the unattached beads were washed out with fresh warm DMEM twice.

Preparation of PDMS substrate for HL-1 cell culture

Silicone base and curing agent of PDMS were mixed thoroughly in a ratio (m/m) of 10:1, 40:1, and 60:1. Afterwards, the mixtures were poured on cover slips for spin coating. Each cover slip was spin coated with a speed of 1000 rpm for 1 minute, which resulted in a thickness of 50- 55 μm . The curing procedure was carried out for 4 hours at 80 $^{\circ}\text{C}$ followed by a slow cool down to room temperature, as given in Ref. [114]. The resulted elastic modulus for samples PDMS10:1, PDMS40:1, and PDMS60:1 were 1697.9 kPa, 30.3 kPa, 1.7 kPa, respectively. Before protein coating, the samples were sterilized by UV light for half an hour. To promote cell adhesion, the PDMS substrates was incubated with a protein solution containing 5 $\mu\text{g/mL}$ fibronectin and 0.02 $\mu\text{g/mL}$ gelatin (Fisher Scientific, USA) for approximately 60 minutes at 37 $^{\circ}\text{C}$. Then these substrates were rinsed once with distilled water and kept for cell culture.

Preparation of cell sample for scanning electron microscope (SEM) and focused ion beam (FIB) experiment

Firstly the cells were cultured on a silicon substrate or glass cover slip under the same conditions as mentioned before. According to Ref. [115], cells were washed two times with warm PBS and then chemically fixed with 3.2% glutaraldehyde (Sigma-Aldrich, USA) in PBS for 15 minutes at room temperature. After that, the cells were washed with PBS again and dehydrated via a series of solutions of starting from 10% up to 100% ultrapure ethanol in ultrapure water. Every step was performed for 5 minutes. The 95% ethanol solution was exchanged 3 times with 5 minutes for each exchange. The cells were finally kept in 100% ultrapure ethanol until critical point drying (CPD) experiment was performed. In order to preserve the cell morphology, the ethanol in cells was exchanged with CO_2 via the CPD method. Before the SEM experiment, the samples were sputter-deposited with iridium. In order to determine the real position of a bead, FIB milling was performed on the silicon substrate samples.

Drug treatment

For drug treatment samples, the cells were first cultured and bound with beads in the same way as the control samples. The cells were then treated with either blebbistatin or paraformaldehyde (both

from Sigma-Aldrich, USA). For Myosin inhibition, after washing the unbound beads, fresh DMEM with 50 μ M blebbistatin was added to the cell culture and incubated for additional 20 minutes. In order to fix the cells, they were washed two times with warm PBS, and chemically fixed with 4% paraformaldehyde in PBS for 30 minutes at room temperature. Then they were washed three times with PBS.

3.2.2 Primary rat brain cell

Preparation of cell sample for MT experiment

Primary cortical-striatal co-cultures or mixed glia cultures were prepared from E18 Wistar rats. Cortices with striatum were isolated in ice cold Hanks Balanced Salt Solution without Mg^{2+} and Ca^{2+} (HBSS-, Gibco, USA). Tissue was mechanically triturated approximately eight times in 2 mL HBSS- with a fire polished, silanized glass pipette until the cell suspension was homogeneously turbid. 4 mL HBSS+ (HBSS with Mg^{2+} and Ca^{2+} , Gibco, USA) were added into the cell suspension. After incubation on ice for 3 minutes, the top 3 mL of the suspension (neuron cell suspension) were transferred to a new tube and subsequently the bottom 2 mL of the suspension (mixed glia suspension) were transferred to separate tubes, subsequently. After a 200 g centrifugation (1100 rpm) for 2 minutes at 25°C, neurons were resuspended in supplemented NB medium: 10 mL NeuroBasal (Gibco, USA), 100 μ L B27 (Gibco, USA), 0.25 mM Glutamax (Gibco, USA), 50 μ g/mL gentamicin (Thermo Fisher Scientific Inc., USA). Glial cells were resuspended in supplemented 10 mL Dulbecco's Modified Eagle Medium (DMEM+F12, Glutamax, Gibco, USA), 10% fetal bovine serum, 100 μ L non-essential amino acid (x100, Biochrom GmbH, Germany), 1 mM sodium pyruvate (Invitrogen, USA), and 50 μ g/mL gentamicin. Trypan blue staining was used to estimate viable cell density. 50 k – 100 k cells were seeded on flame sterilized, 0.01 mg/mL poly-D-lysine coated (PDL, Sigma-Aldrich, USA) in Gey's balanced salt solution (GBSS, Sigma-Aldrich, USA) cover slips in 24-well cell culture plate. Cultures were incubated at 37 °C, 5% CO₂. Half of the culture medium was changed in every 3-4 days. The Dynabeads® M-450 Epoxy beads (Thermo Fisher Scientific Inc., USA) were coated with 25 μ g/mL fibronectin according to the procedure recommended by the manufacturer. After stirring by a vortex mixer, the fibronectin-coated beads were diluted in DMEM and then added to each well (1x10⁵ beads, 0.5 ml). The plate was then incubated for another 30 minutes at 37 °C. The samples were rinsed twice with fresh warm DMEM to eliminate the unattached beads [105].

Preparation of PDMS substrates for brain cell culture

The same PDMS as in the HL-1 cell experiment were used. Round cover slips with 12 mm diameter were spin coated with a speed of 3000 rpm for 1 minute, which resulted in a thickness of around 35 μ m. After 1 hour sitting time to make the PDMS on cover slip flat, the curing procedure was carried out as in the HL-1 cell experiment. To promote cell adhesion to the PDMS substrates, the samples were treated in oxygen plasma for 3 minutes. Afterwards, the samples were sterilized by UV light for

half an hour. Then the protein coating and cell culture were performed the same way as for the normal cover slip samples.

Live-dead staining

The cell medium was first washed with warm PBS. Then the cells were cultured in a staining solution for 15 minutes at 37°C. After that, the cells were washed with PBS. The staining medium was made of PBS with calcein AM for living cells (shown in green, Sigma-Aldrich, USA) and ethidium homodimer-1 for dead cells (displayed in red, Sigma-Aldrich, USA) at a concentration of 4 μ M each.

Immunostaining

The cell samples were washed three times with isotonic warm PBS and then fixed with 4% paraformaldehyde in PBS for 10 minutes at room temperature. After washing these cells with PBS three times, the cell membranes were permeabilized with 0.3% Triton X100 (Sigma-Aldrich, USA) in blocking buffer (BB, including: 50 ml PBS, 0.5 g bovine serum albumin, and 1 ml heat inactivated goat serum) for 10 minutes at room temperature. After washing with PBS three times again, BB was added and the samples were incubated overnight at 4°C. Then the substrates were rinsed three times with PBS. The cell samples were incubated with primary antibody in BB in a dark chamber for 1.5 hours. After that the substrates with cells were washed three times with PBS. The secondary fluorescent antibodies and DAPI were used together in BB. After 1.5 hours incubation in the dark chamber, the substrates were subsequently rinsed with PBS and bidest water. The detailed information of primary and secondary antibodies is listed in the Table A.1 (See Appendix). Finally, the cover slips were mounted on the object slides with mounting media and stored in the dark at 4°C [105].

4. Results and Discussion

In this chapter, the results of this work are discussed in detail. In the beginning, high throughput multi-pole magnetic tweezers are inspected by both simulations and experiments. Then the biocompatibility and passivation of magnetic tips is examined. After that, the implementation of magnetic twisting cytometry is presented based on the MT setup. At last, with these developed microreology tools, the mechanical properties of both HL-1 cells and brain cells are characterized. Parts of the work described in this chapter have been published in Refs. [104, 105, 116-119].)

4.1 Multi-pole Magnetic Tweezers

4.1.1 Force Produced by Multi-pole Magnetic Tweezers

As stated in the introduction chapter, single-pole MT can apply a very high force. However, usually only a single cell can be characterized at a time because the force drops quickly with the distance, so that the throughput is relatively low. Consequently, it will be beneficial to develop multi-pole (≥ 3 poles) high force MT which exhibit good maneuverability and high throughput. In order to determine the suitability on being selected for the specific applications, the forces produced by different structures (3, 4, 6 poles) were inspected using finite element simulation. The simulations performed were limited to 2D geometrical models. The magnetic fields in the workspace were evaluated by a nonlinear constitutive relation for magnetic materials. The forces were calculated based on the magnetic moment of Dynabeads® M-270 particles. Unless otherwise indicated, the shapes of all tips were like isosceles trapezoid, and the protrusion angles of the tips were around 35° . The distance from the center of the workspace to the tip was $100\ \mu\text{m}$, each tip had a width of $60\ \mu\text{m}$ and each tip corner had a $10\ \mu\text{m}$ radius. The results are presented in the table 4.1. Here, the currents actually refer to the current ratio among coils. The coil current of the source pole is set to 1. The center of workspace is denoted with O. B_0^S means the saturation magnetic field at workspace center. F_0^S refers the magnetic force at O on particle upon the magnetic field of B_0^S . The isotropy is deduced from the ratio of saturation forces F_0^S at points $(-50\ \mu\text{m}, 0\ \mu\text{m})$ and $(50\ \mu\text{m}, 0\ \mu\text{m})$.

Table 4.1. Comparison among different magnetic pole configurations

Pole	Currents (clockwise)	B_0^S (T)	F_0^S (pN)	Isotropy
3	1 : -1/2 : -1/2	0.62	1060	0.942
4 ^a	-1/3 : 1 : -1/3 : -1/3	0.467	860	0.379
4 ^b	-1/2 : 1 : -1/2 : 0	0.32	1156	0.602
6 ^a	-1/2 : 1 : -1/2 : 0 : 0 : 0	0.114	548	0.246
6 ^b	1 : 0 : 0 : 0 : 0 : -1	0.235	656	0.348

The magnetic field and force distributions of MTs with 4 and 6 poles in the workspace are shown in the Fig. 4.1. The situation of 3 poles will be introduced in detail in the next section. Because of the superparamagnetism of magnetic bead, the magnetic force always directs along the gradient of the

magnitude of magnetic field, independent of the direction of the magnetic field. For 4 and 6 poles, all the best configurations are that the current of anti-source pole (the pole opposite to the source pole) is zero, namely 4^b and 6^b , as seen in Table 4.1, Fig. 4.1 (b) and Fig. 4.1 (d). When the current of anti-source pole is not zero, the particle in workspace is even dragged along the inverse direction, see in Fig. 4.1 (a). As in the Table 4.1, the highest force at the center of workspace is achieved in the four-pole configuration of 4^b , however, the force at the area far away from source tip drops quickly, which is similar to the finding in Ref. [64]. In the areas indicated by a black squares ($1/2$ area, $0.1 \text{ mm} \times 0.1 \text{ mm}$), the forces are relatively homogeneous, which is important for control. In other hand, although the amplitude of force is much low in the 6 poles situation, the force direction shows a very even distribution, as seen in Fig. 4.1 (d). Because of higher degree of freedom, higher flexibility for complex actuation can be achieved with 6 poles. For example, a 6 poles structure can be adopted for 3D actuation and twisting [63].

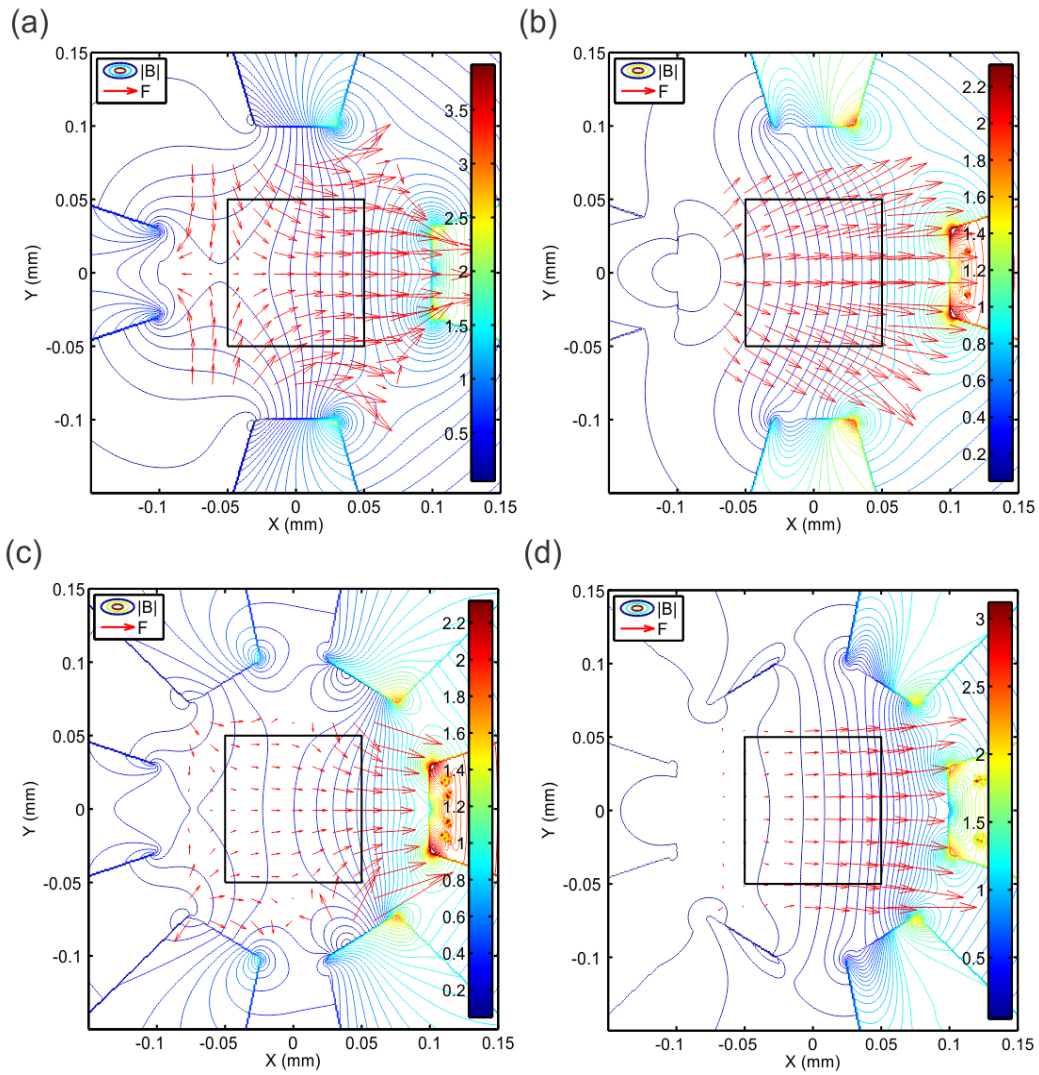


Fig. 4.1. (a)- (d) Simulated magnetic field (magnitude) and force for 4^a , 4^b , 6^a , 6^b poles configurations respectively.

In conclusion, for 2D actuation, the 3 poles structure MT was chosen because of its high force and good force homogeneity. Considering the flexibility and expansibility of the 6 poles structure, the main yoke was configured with 6 poles, with a larger air gap among the poles. When operating in the tri-pole MT mode, only 3 of the 6 poles were used. Every adopted pole was equipped with a sharp magnetic tip, as seen in Fig. 4.2.

4.1.2 Tri-pole Magnetic Tweezers

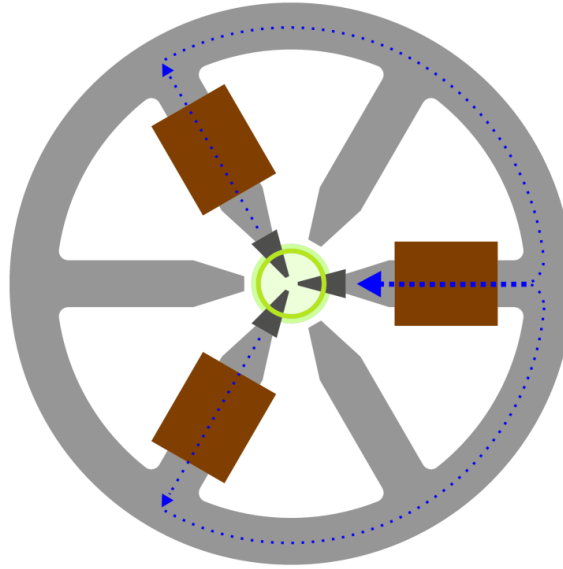


Fig. 4.2 Schematic of tri-pole magnetic tweezers. The main yoke, magnetic tips, cover slip, glass ring, and coils are shown in light gray, dark gray, light green, green, and brown, respectively. The unused coils at the other three fingers are not shown. Blue dashes indicate the magnetic flux when the right pole is employed as the main source pole. This drawing is not to scale. (Adopted from Ref. [117].)

A schematic of the tri-pole MT is shown in Fig. 4.2. The fluidic reservoir, also presented in Fig. 3.1, is composed of a cover slip, 3 magnetic foil tips, and a glass ring. The magnetic field and force distribution of an example of tri-pole MT are presented in Fig. 4.3 (a). The data was obtained from simulations of 80 μm wide tips, with a workspace of 100 μm in radius, and with currents of 174 Ampere turns in the right source coil and -87 Ampere turns in the two other counter coils. The center of the workspace is marked as O, with a force of 1219 pN along the x axis. Because the right tip is located close by, the force at point B is maximum in the upper half square, with $|F(B)|/|F(O)| = 1.24$. In the area between the corners of the tips, despite a high magnetic field, the magnetic force is low because of small magnetic field gradients. So, the minimum force in the upper half square is located at A, with $|F(A)|/|F(O)| = 0.69$. The ratio F_y/F_x is the highest at point C, namely 0.69. Here, too high a ratio F_y/F_x means the force component directing outward from the left-up tip is low. So it is hard to actuate the bead in the nearby area. According to the symmetry, there are similar features in the bottom half square. Outside of this square, the force changes rapidly. Although higher force can be achieved when approaching the tips, the resultant higher nonuniformity will also deteriorate the maneuverability. In particular, there are some “dead zones” near the tips, where the particles are

always pulled toward the tips at any nonzero input currents. Due to the limited accuracy of the manufacturing process, some tips may exhibit deformations. In order to inspect this effect, the right tip was shifted in the simulation by $20\ \mu\text{m}$ along the y axis, as shown in Fig. 4.3 (b). It is obvious that there is a large change of the magnetic field distribution in the area near the right tip. The percentage error of force induced by this deformation is depicted in Fig. 4.3 (c) as a surface plot of the $1/2$ area. The error is highest at the upper and lower corner towards the right tip. However, the error decreases with distance from the deformed tip. Within the inner $1/4$ area ($50\ \mu\text{m} \times 50\ \mu\text{m}$), the error is less than 18.7%. But the maximum error increases to 41.4% in the $1/2$ area. In order to optimize the width of the tip, the simulations were done for tips with a width of 30, 60, 80, 100, and $120\ \mu\text{m}$. The results are presented in Fig. 4.3 (d). With a wider tip, the saturation current increases, hence higher magnetic flux can be applied to the workspace, which also enhances the force. When the tip has a width of $100\ \mu\text{m}$, which equals the distance from the central point to the tip, a maximum force of $1378\ \text{pN}$ can be exerted on a M-270 bead. This result agrees well with the findings presented in Ref. [29, 64].

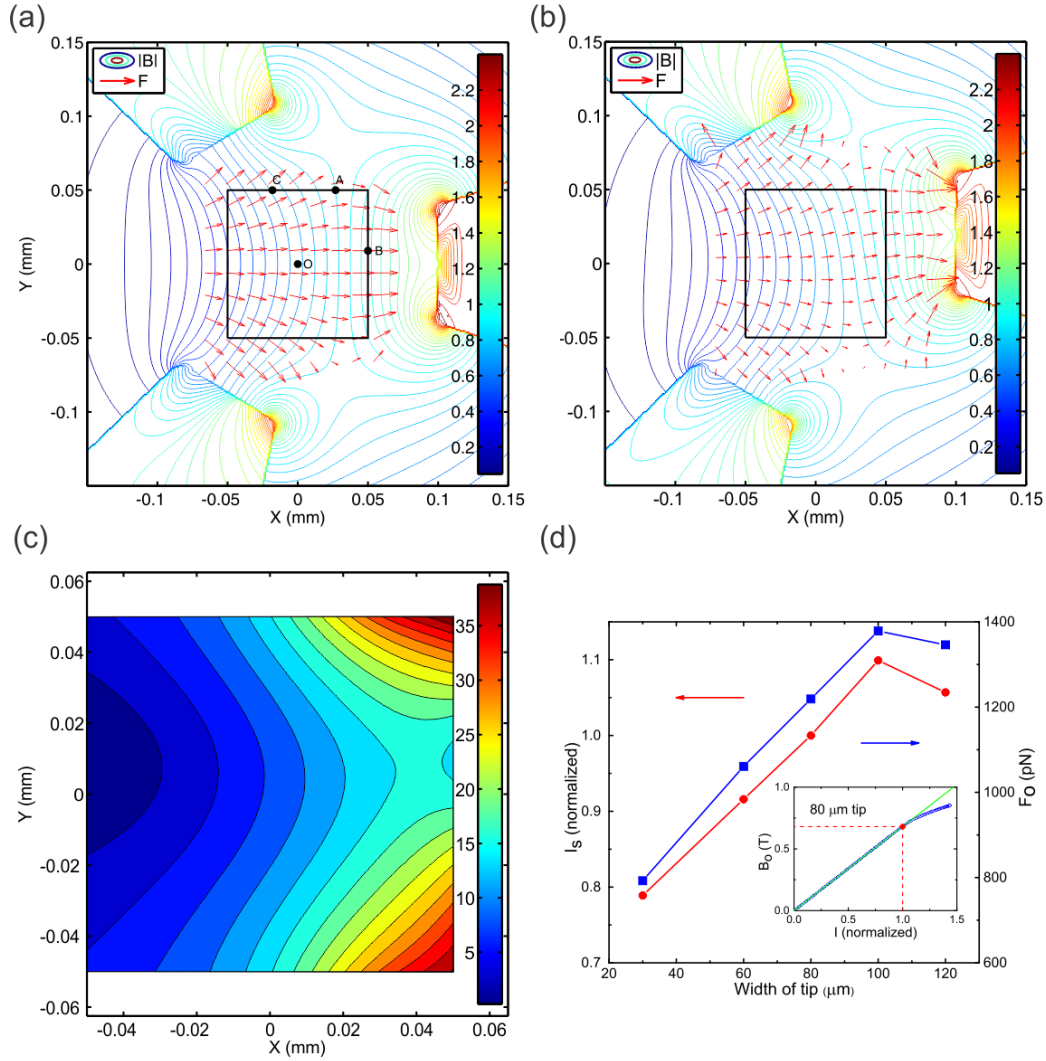


FIG. 4.3 (a) Simulated saturation magnetic field (magnitude) and force with $80\ \mu\text{m}$ wide tips. (b) Simulated saturation magnetic field (magnitude) and force field with $80\ \mu\text{m}$ wide tips, the right tip has a displacement of $20\ \mu\text{m}$ along y axis. (c) Simulated force error (in percent) of the displaced tip geometry in (b) vs. the symmetric tip geometry in (a). (d) Simulated forces at workspace center (O) and saturation currents for different width of tips. The dependence of the magnetic field at O on the current for $80\ \mu\text{m}$ tips is presented in the inset figure. The

saturation currents are normalized by the saturation current of 80 μm tips (174 Ampere turns, as indicated by the red dot in the inset figure). (Adopted from Ref. [104].)

In order to verify the simulation and the inverse force model, the magnetic force was calibrated according to the approach described in the section 3.1.8. Before experiment, the fluidic reservoir was aligned manually under microscope by adjusting the XY stage with the help of overlaying the designed tip contours. As shown in Fig. 4.4 (a), the actual tips were not very well defined. Because of laser cutting, all tips have a smaller width than desired, especially the tip at bottom right. Also the top right tip was a little thinner than designed. A bead was positioned near the center of the workspace. With the help of feedback control, the bead was dragged along x direction in the central area. The magnetic force on a bead that was held at the central point was compared to the force model as a function of the coil current. The viscous solution used was DEG. The results are presented in Fig. 4.4 (b). As predicted by the model, the measured magnetic force increased with coil current. Considering the actual shape of tips, the experimental result agrees well with the force model in the low force range (< 400 pN). When the set force was larger than 400 pN, some fluctuations were observed in practical force output, which are probably due to the high speed of the bead. In order to clarify this, another fluid of 85% glycerol with higher viscosity was used for this high force measurement. With this fluid, the bead shows a clear saturation behavior towards 360 pN. Several causes like smaller width of tips can be ascribed to this early saturation. A detailed discussion will be given in the next section 4.1.3. Thanks to the sharp structure and the high permeability of magnetic parts, just a very low current (≤ 60 Ampere turns) is sufficient to achieve a high force.

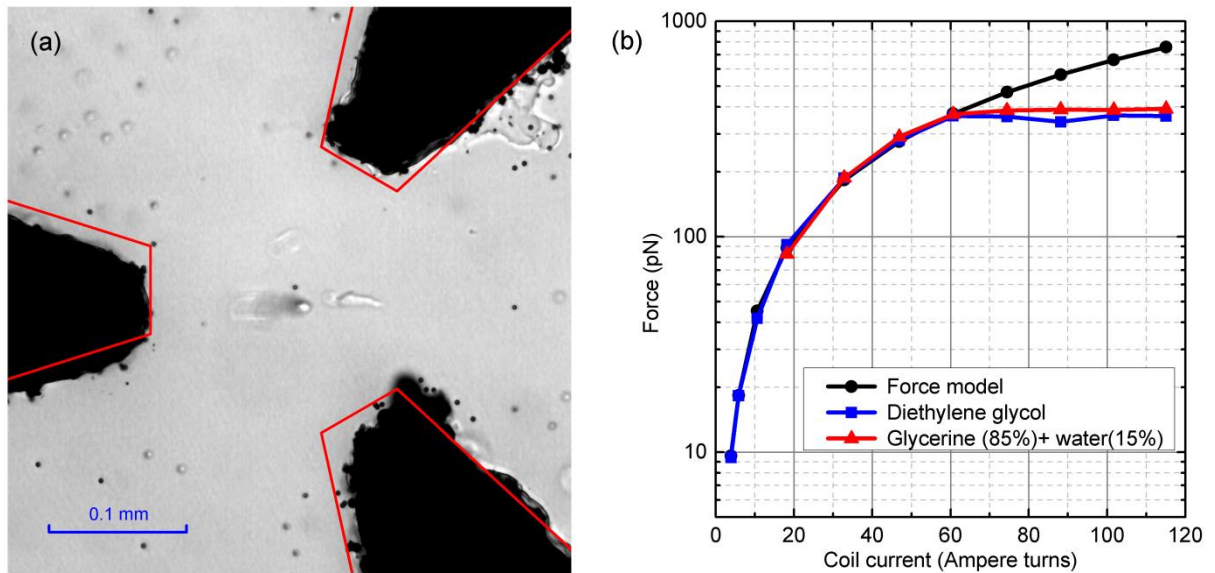


FIG. 4.4 (a) The fluidic reservoir under the microscope. In the workspace, there are several spots in PDMS. (b) Calibration of force at center of workspace. (Adapted from Ref. [104].)

In order to evaluate the actual effect of tip deformation, the force distribution was measured on a 7×7 grid, as seen in Fig. 3.13. In experiment, the force model was activated to set a constant force of 20 pN along x direction at each grid point. A map of the force error is shown in Fig. 4.5 (a). The error was calculated by the formula $100\% \times (F_{\text{exp.}} - F_{\text{mod.}}) / F_{\text{mod.}}$. As in simulation (see Fig. 4.3 (c)), the

deviation is small in the central area and far away from deformed tips. It is obvious that the error in upper right area is high, which can be inferred from the upper right thinner tip. In addition, in order to inspect the feedback control, the magnetic bead was actuated to follow a predefined trajectory in 1/4 area by a few set points, as shown in Fig. 4.5 (b). Here, the output force of PI controller was limited to 30 pN in both x and y direction. When the bead got closer than $0.5\ \mu\text{m}$ to each set point, then it was actuated towards the next set point. In the trail of ‘F’, there was a little bending towards the left in the vertical line. Similar behavior was observed in the slash of ‘Z’. This may result from the unbalance of the tips. The force component from the left tip was higher than desired. Although there were several spots in the workspace as shown in Fig. 4.4 (a), the bead could be tracked very well by 2D XCor algorithm (COM did not work in this situation). Few tracking points were missed at the center of the ‘Z’. This is because of a spot in that area with a very similar optical pattern as the bead’s, which caused the polynomial fits of cross-correlation fail.

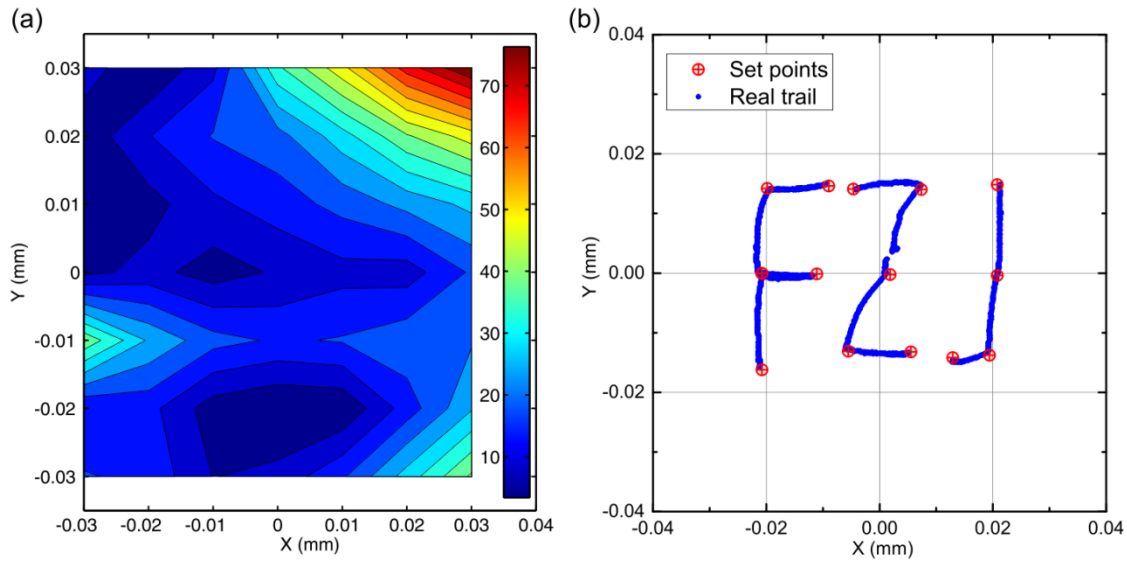


FIG. 4.5. (a) Force error (percent) between experiment and force model was mapped at a 7×7 grid with steps of $10\ \mu\text{m}$. (b) A M-270 bead was actuated to move along predefined set points in DEG. For the clarity, the intermediate segments between letters were not shown. (Adopted from Ref. [104].)

4.1.3 Force Reduction in High Force Magnetic Tweezers

As pointed out in the previous section, the practically achieved saturation force in MT is lower than the predicted value. As indicated by the simulations, geometry errors such as a smaller width of tips or tip deformation can lead to deviations. Besides these, there are also some other factors which contribute to the force reduction.

In contrast to traditional mechanical punching, laser beam machining can avoid shear deformation at the cutting edges. However, in electrical steel machining, there are numerous reports that the high temperature shock caused in the cutting process can modify the microstructure in the area near the cutting edge [66, 120]. Like the shear deformation, this can also induce some degree of deterioration in the material’s magnetic performances [65]. In order to inspect the effect of laser cutting, the

morphologies of the tips were characterized by SEM (Magellan 400, Nanolab Technologies, USA) equipped with an energy dispersive x-ray spectroscopy system (EDS) for element analysis. Some SEM pictures of tips are shown in Fig. 4.6.

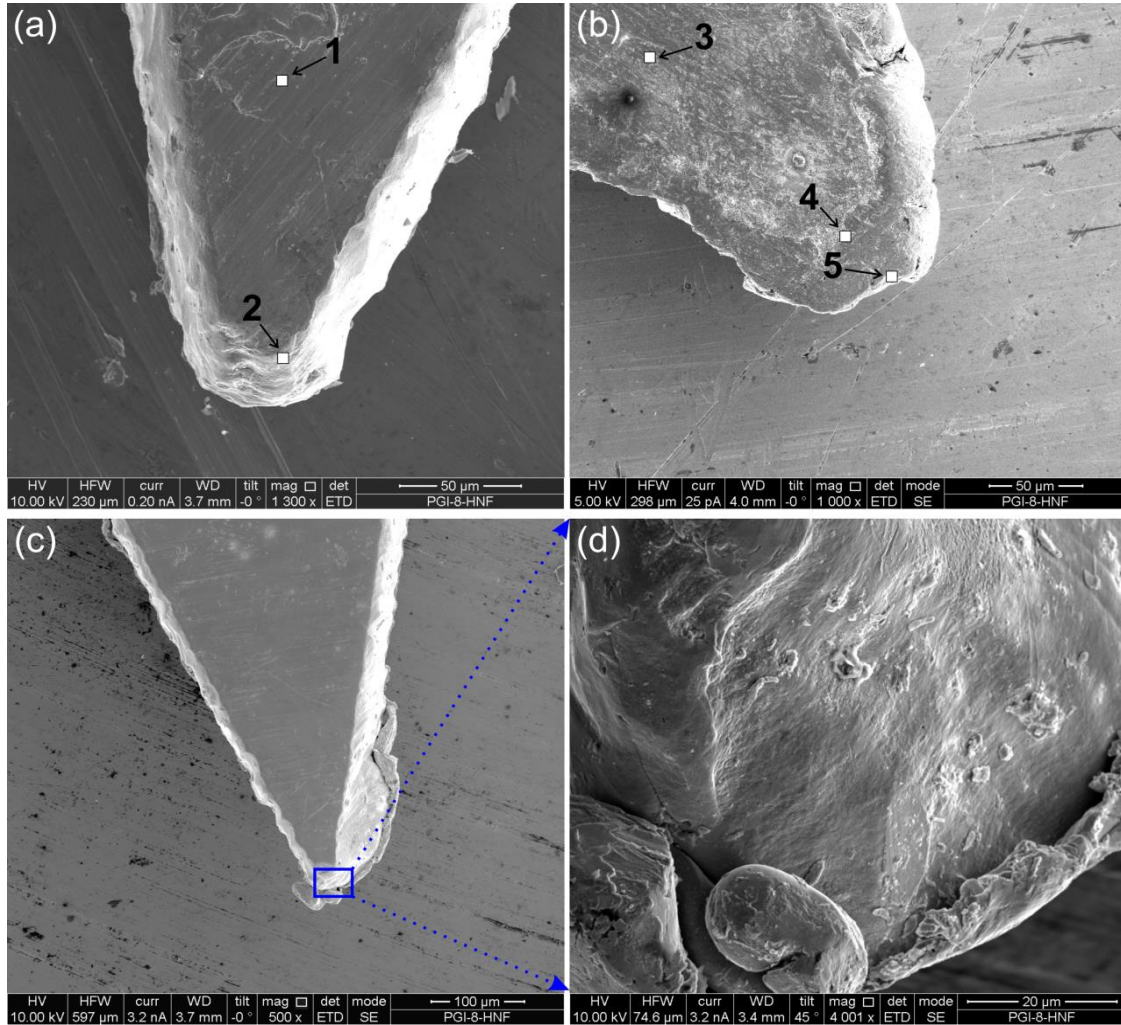


Fig. 4.6. Magnetic tips after laser cutting: (a) top view, (b) bottom view (not the same tip), (c) a tip with large deformation, (d) a local zoom view of (c). (Adapted from Ref. [117].)

As shown in Fig. 4.6 (a), the surface planar slip texture of the tip indicates that the material is partially ordered in its crystal structure [67]. During the cutting process, the top surface of tip melts at first. As can be clearly seen in Fig. 4.6 (b), some molten material flowed down and solidified near the bottom edge. Hence the magnetic tip usually exhibits a narrower width at the top side than at the bottom side. A magnetic tip with large deformation at its front part and a zoom view are presented in Fig. 4.6 (c) and (d). All the vertical cutting planes are a little rough, which is similar as in electrical steel cutting [65]. The compositions of sites marked as 1-5 in Fig. 4.6 (a) – (b) were analyzed by EDS, and are listed in Table 4.2. Only the elements Fe, Co and V were analyzed, and the measured signal intensities were normalized. The composition on each site was measured 3 times. In the area far away from the cutting edge such as sites 1 and 3, the compositions are more consistent with the original ratio ($\text{Fe}_{49.1}\text{Co}_{49}\text{V}_{1.9}$). Due to a few μm penetration of EDS, the data deviates somewhat from the nominal composition. At the sites close to the cutting edge, the segregation becomes more obvious.

For example, higher cobalt and lower iron weights were found at the outer points 5 and 4 than at the inner points 1 and 3. Nevertheless, the vanadium content in the area near the cutting edge revealed a large fluctuation. Except for site 5, all sites showed a higher ratio of vanadium than nominal. Besides, some oxygen was found in the area near the cutting edge, which may be evidence of some residual oxide after annealing. An example of an EDS spectrum is shown in Fig. 4.7.

TABLE 4.2 Element composition at different sites (Adopted from Ref. [117].)

Inspection site	Fe (at.%)	Co (at. %)	V (at. %)
1	46.2 ± 0.67	49.17 ± 0.71	4.81 ± 0.24
2	40.51 ± 0.72	49.51 ± 0.67	9.98 ± 0.28
3	44.83 ± 0.77	49.82 ± 0.73	5.35 ± 0.26
4	39.63 ± 0.82	55.35 ± 0.78	5.01 ± 0.28
5	38.01 ± 0.90	60.85 ± 0.85	1.15 ± 0.23
Average*	45.14 ± 2.84	50.33 ± 4.08	4.53 ± 3.76

* Statistics on 36 sites on 20 μm layer near cutting edge from 9 tips. 3 sites with Vanadium > 20% are not included.

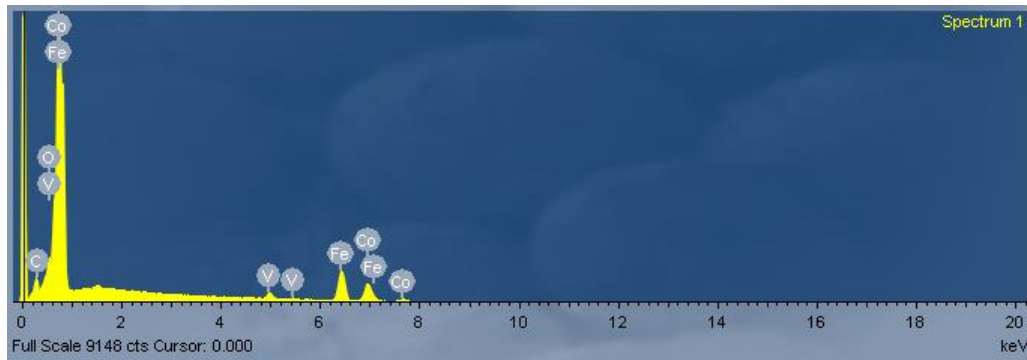


Fig. 4.7. An example of EDS spectrum.

Usually, FeCo-V alloys have a tendency to crystallize in γ phase (fcc) or α phase (bcc), depending upon the alloy composition and the heating process [67]. The segregation, such as the generation of a vanadium rich phase, could lead to a dilution effect due to non-magnetic precipitates. In addition, the deviation from near-equiatomic FeCo ratio can increase the magnetic anisotropy [121], and reduce the permeability and saturation magnetization [122]. In Fe-Si electrical steels, it is frequently observed that the laser cutting can induce high stress in the area near the cutting edge [66]. This large internal stress usually distributes over several grains and can be released partly during the annealing process. The residual stress tends to induce additional magnetic anisotropy and hence a lower permeability, and increases the coercive field. Compared to electrical steel, FeCo based alloys are usually more sensitive to strain because of a higher magnetostriction value [67]. Although recrystallization takes place during annealing, the crystal structures near the cutting edge cannot recover totally at the annealing temperature (800-820 $^{\circ}\text{C}$) recommended by the material vendor.

In order to model these effects on the force output of MT in 2D simulation, the tips were divided into a bulk part and a layer near the cutting edge. In the case of tri-pole MT, the maximum magnetic field or force can be achieved when the width of tips have the same dimension as the radius of the workspace, as in the previous section 4.1.2. Here, both r and w equal $60\text{ }\mu\text{m}$, as depicted in Fig. 4.8 (a). Depending on the annealing time and temperature, the grain size of FeCo-V alloy ranges from few to dozens of μm , and the coercivity usually decreases with the size of the grains [123]. Although the area practically affected by laser cutting may be larger than one grain, here the affected layers were modeled with thicknesses d of $10\text{ }\mu\text{m}$ and $20\text{ }\mu\text{m}$, as shown in Fig. 4.8 (a). The experimental magnetization (B - H) curve was fitted to a piecewise Langevin function, as given in Eq. (4.1). The parameters a and M_s are mainly related to the permeability and saturation magnetization, respectively. The parameters H_i and M_i were adjusted to join the low magnetic field section and the section described by Langevin function. The values adopted from the fitting result are $a= 53.82$, $M_s= 2.2\text{ T}$, $H_i= 22.76\text{ A/m}$ and $M_i= 0.0456\text{ T}$. The B - H fitting curve for $H < H_i$ was adopted directly from the experimental data. The experimental B - H curves and the fitting result are shown in Fig. 4.8 (b).

$$M(H) = M_s \left(\coth\left(\frac{H - H_i}{a}\right) - \frac{a}{H - H_i} \right) + M_i, \quad H > H_i \quad (4.1)$$

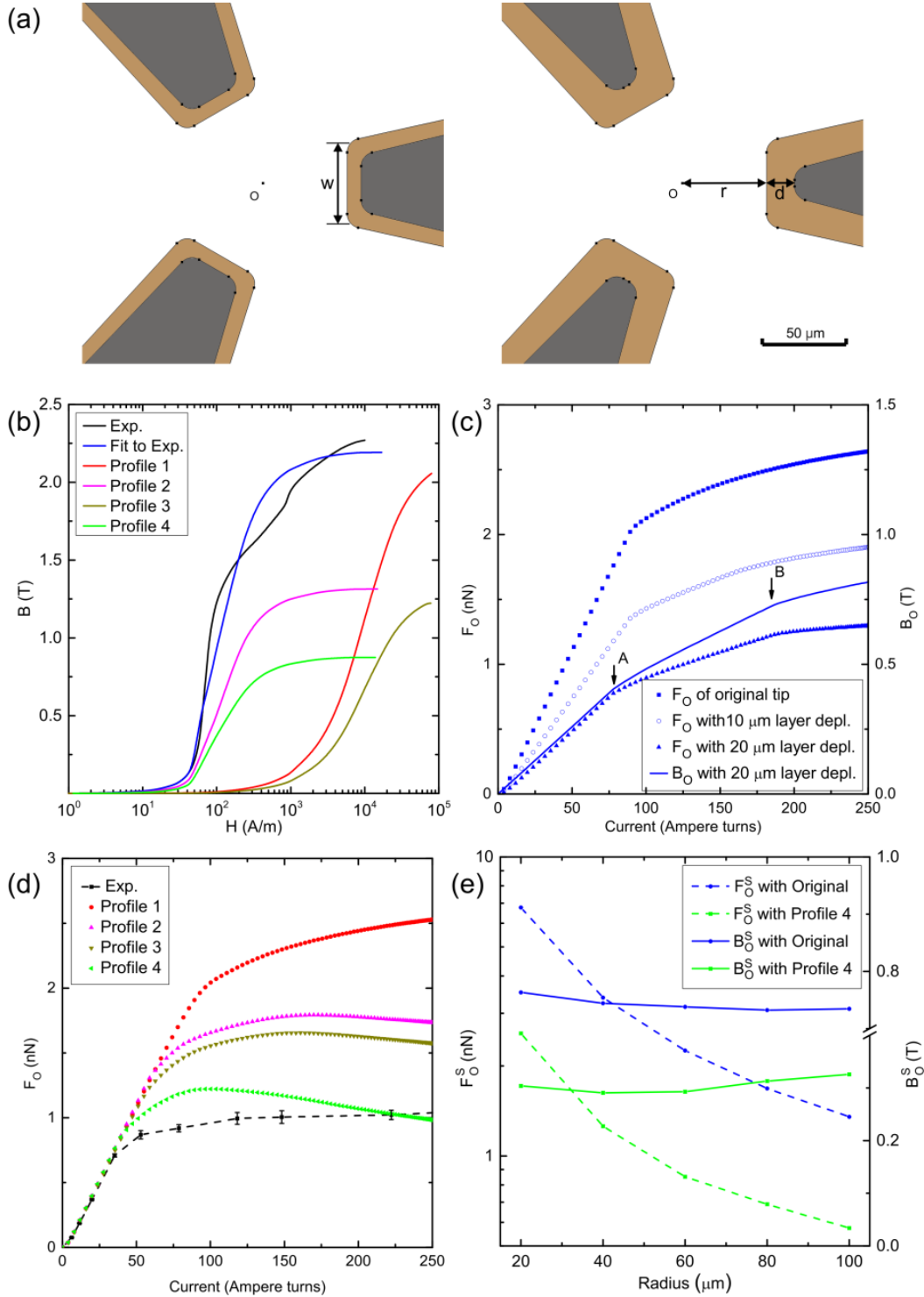


Fig. 4.8 (a) Simulation structures used for modeling the magnetization deterioration effect. The unaffected bulk is sketched in dark grey, the affected area near the cutting edge is shown in light brown. The central point of the workspace is marked as O. (b) Different tuned $B-H$ curves used for simulating the layer near the cutting edge. (c) The simulated force-current curves for different geometries. Blue line represents the magnetic field of tips with 20 μm edge layer depleted. The knee points A and B are explained in the text. (d) Simulated force-current curves for different material properties in the 20 μm edge layer. The black curve shows a typical experimental result. (e) The saturation force and magnetic field for different workspace radii were calculated with original and tuned magnetic properties of the edge layer. The widths of tips were chosen to equal the workspace radius. For the structure with 20 μm wide tips, only a 10 μm thick edge layer was adopted. (Adopted from Ref. [117].)

In order to simulate the magnetization of the affected areas, the magnetization parameters a , M_s and M_i of these areas were tuned. For modeling the deterioration of saturation magnetization, the original M_s and M_i in Eq. (4.1) were multiplied by a reduction factor. The $B-H$ curves at low H were reduced

by the same factor. The B - H curve with M_s reduced to 0.6 times is plotted in Fig. 4.8 (b) as Profile 2. Similarly, the permeability can be tuned by the parameter a . As shown in Fig. 4.8 (b), both parameters a and M_i in Profile 1 were reduced 100 times at $H > H_i$. As a simple approximation, the B - H at $H < H_i$ was modeled as a linear function only depending on M_i . All the parameters for modeling are listed in Table 4.3.

Table 4.3 Reduction factors used for B - H tuning at cutting edge (Adopted from Ref. [117].)

	$H > H_i$			$H < H_i$
	a	M_s	M_i	
Original*	1	1	1	scale from exp.
Profile 1	0.01	1	0.01	linear
Profile 2	1	0.6	0.6	scale from exp.
Profile 3	0.01	0.6	0.006	linear
Profile 4	1	0.4	0.4	scale from exp.

*Fitting of experimental data

As the first step, the outer layer of the tips was depleted, and treated like air. The results are shown in Fig. 4.8 (c). In all cases, the magnetic force at the workspace center O firstly increases linearly with the coil current. The linear relation between force and magnetic field can be explained by the magnetization of the bead (M-270), which has a small linear magnetization range at magnetic fields < 10 mT. The knee point of magnetization (the crossover to saturation) is very low, around 50 mT, as shown in Fig. 3.10. Consequently, the nonlinear force-current relation only exists at very low magnetic field. Beyond the knee point, the magnetic moment of the bead saturates very quickly, thus the contribution to increasing magnetic force mainly comes from the increasing magnetic field gradient. Because of high magnetic flux output, the intact tips without depleted edge layers exhibit the highest slope and the highest saturation force. In the situation of a $20\text{ }\mu\text{m}$ depleted layer, the magnetic field at O shows two saturation points noted as A and B, seen in Fig. 4.8 (c). Point A corresponds to the magnetization saturation happening at the vortexes of the tips. When the saturation area expands with increasing coil current, the second knee point B emerges, at which the whole front area of the tip gets saturated. As a result, the change of force follows the magnetic field. Beyond point B, the force on the bead levels off. Fig. 4.8 (d) presents the force-current curves of tips with different magnetic properties in the $20\text{ }\mu\text{m}$ thick edge layers. Unlike the previous situation with depleted edge layers, all force-current curves have the same slope. In case of reduced permeability, the force above the first saturation only decreases a little. Compared to the permeability, the parameter M_s has a stronger effect on the high force. As shown in Fig. 4.8 (d), it is obvious that the saturation force measured in experiment is close to the tips with B - H property of Profile 4 in the edge layer. However, the saturation magnetization (0.88 T) here is much lower than the estimated value (~ 1.8 T) based on the average composition in Table 4.2 and the data shown in Ref. [67]. In order to clarify this, three other contributing factors should be considered: 1) The very low permeability at high magnetic field also has an important role on the saturation force, as shown in Fig. 4.9 (with the same model as in the $20\text{ }\mu\text{m}$ affected layer situation). 2) The real B - H data of the material is much more complicated than the

formula adopted here. 3) Unlike the uniform layer modeled in the simulation, the magnetic deterioration in practical tips varies with the distance from the cutting edge.

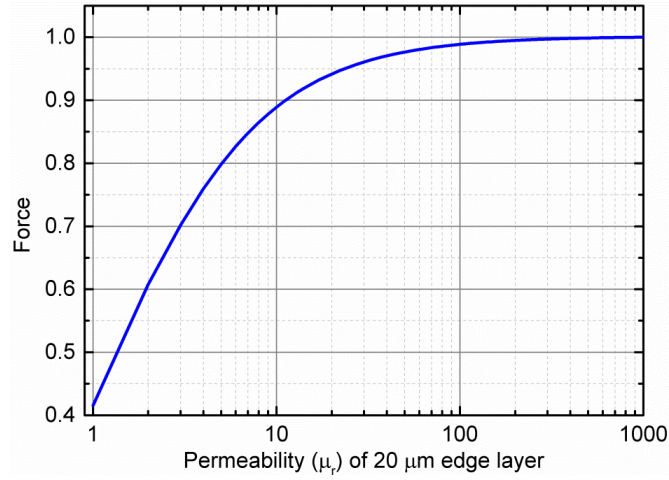


Fig. 4.9 Impact of permeability on force. The force is scaled according to the force when $\mu_r=1000$.

As shown in Fig. 4.8 (d), the experimental tip exhibits a complex magnetic behavior with three saturation stages. The first saturation stage is very short, which may arise from the 3D structure. The vertexes of the front tip get saturated firstly, and then the saturation spreads quickly around these vertexes. When the saturation area extends more deeply into the bulk of the tip, the second stage appears. In experiment, because of permeability reduction, this progress is more like in Profile 3 situation but slower than Profile 4. As in simulation, when the whole front tip gets saturated, more magnetic flux flows directly among the tips without passing through the workspace. As a result, in the workspace, the magnetic field gradient and the force even start to decrease with coil current increasing. However, the force in experiment still increases very slowly with current in the third saturation stage. This can be ascribed to the strong magnetic anisotropy and high coercivity because of the crystal defects induced by the laser cutting.

As in the introduction chapter, the saturation force of MT can be enhanced by adopting a small sharp structure. Fig. 4.8 (e) presents the calculated saturation force and magnetic field of MT with different tips width and workspace radii. In addition, the saturation forces with the magnetic properties in the 20 μm edge layer tuned by Profile 4 are also displayed. It is observed that the saturation magnetic field at workspace center almost remains constant at a value close to $1/3 B_s$ of the tip. With a sharp tip and a small workspace, a high magnetic field gradient and hence a high force can be achieved. For example, with a workspace of 40 μm in radius, a saturation force of 3.38 nN can be achieved with the original tips, whereas the tip with tuned magnetic properties can only apply 1.26 nN. The force ratio between original and tuned tips varies around 2.3- 2.6.

Because of the finite thickness of the tips and the focused laser beam used in cutting, the deterioration is different in vertical direction and dependent on the thickness of tip. The structure of the 0.5 mm thick tip at the front is not as well defined as for the 0.1 mm thick tip. In experiments, the fluidic reservoir prepared with 0.5 mm thick tips exhibits an obvious remnant magnetization when

coil current is turned off. A sample of a fluidic reservoir made of 0.1 mm tips is shown in Fig. 4.10 (a). As can be seen, the real profiles of tips have small deviations from the symmetrical contours (green). Tip 1 has a width larger than 60 μm at the front edge. Besides this, there is an indentation on the front top surface, as in the inset image. The front part of tip 2 is sharper than designed. Ahead of tip 3, there is an obvious burr, which is a remnant of the molten material during cutting.

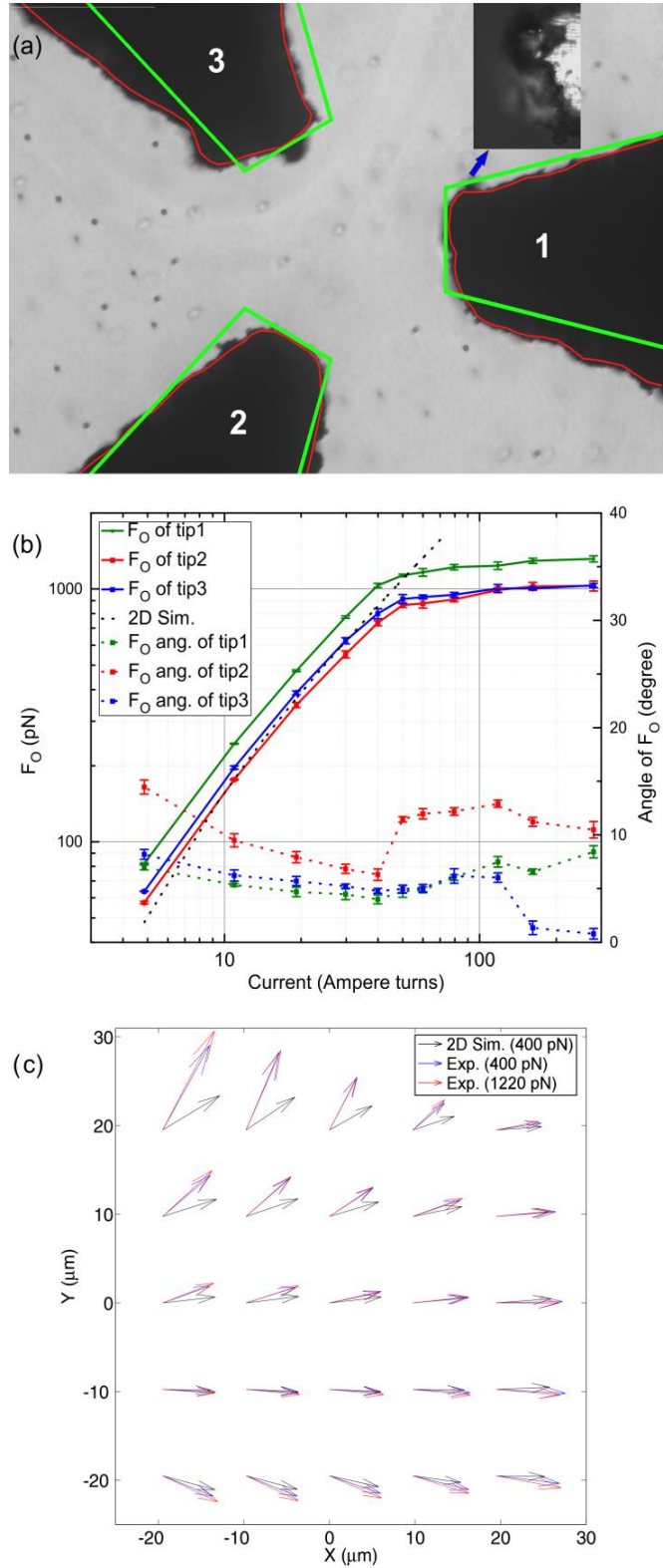


Fig. 4.10 (a) A fluidic cell with 60 μm workspace radius. The thick green line is the symmetrical contour. Red lines are used as the structure in 2D simulation. The inset figure shows the top surface of tip 1. The scale bar is

50 μm . (b) Force-current curves and force directions of different tips at workspace center O. (c) Force distribution in the central area of the workspace, with tip 1 as the main source tip. All force distributions are scaled to O. (Adopted from Ref. [117].)

In order to revalue the impact of tip profile, the forces towards each tip at the workspace center were measured. At first, tip 2 was measured, then tip 3 and tip 1. As in Fig. 4.10 (b), the forces start to saturate at a coil current of around 50 Ampere turns. Before saturation, the forces of tip 2 and tip 3 agree very well with simulation. The force of tip 1 is a little higher than that of tip 2 and tip 3. This may be attributed to the larger size of the tip. Besides, the viscosity of the DEG solution is sensitive to temperature. After some time, the illumination light will induce a small temperature rise (the contribution from the coil is small) in the fluid. It is obvious that all the experimental forces are a little bit higher than the simulated values at forces < 100 pN (see Fig. 4.10 (b)). This could result from the underestimation of the bead's magnetic moment at low magnetic fields. Moreover, all the directions of forces change very little before saturation. As mentioned before, there are three saturation stages. In these saturation stages, the magnetic field distribution among the tips fluctuates lightly with the increase of coil current. As a result, the force directions also exhibit some fluctuations. Compared to tip 1 and tip 3, the fluctuation of the force direction of tip 2 is a little larger. This can be deduced from the irregular structures of tip 1 and tip 3. However, the fluctuation in force direction is small and less than 9 degrees. In addition, a simulation of the force distribution was performed based on the real 2D contours of the tips, the red curves as depicted in Fig. 4.10 (a). In experiment, the force distribution on a 5×5 grid (x: from $-20 \mu\text{m}$ to $20 \mu\text{m}$ and y: from $-20 \mu\text{m}$ to $20 \mu\text{m}$, each with $10 \mu\text{m}$ step) was measured. The results are shown in Fig. 4.10 (c). In the upper left corner, the largest difference between experimental force and simulation can be noted, which comes from the extruded part of tip 3. However, the sharp structure only displays a strong impact in the local area. Like at the center of workspace, the forces' directions in other areas are also not sensitive to the coil current or the magnitude of force. However, compared to the simulation, the experimental force deflected lightly away to bypass tips in up and down areas.

In 2D simulation, the vertical dimension is assumed to be infinite. In reality, the magnetic field bypassing along both sides of the tip will decrease the magnetic field in the workspace. In order to explain the observed difference between experimental and simulated force, 3D simulation is necessary. Because of the heavy computational effort and the difficulty to achieve convergence at high field, 3D simulation was performed only for a single coil current. As shown in Fig. 4.11 (a), except for the middle plane, the forces at other places display some vertical components, which become more obvious far away from middle plane and close to the source tip. The force in the bottom half space is symmetrical to the top half space. As shown in Fig. 4.11 (b), the force distributions exhibit some difference in the three different situations. It is obvious that all force distributions are very similar near the source tip. As in the experiment, the forces in the corner away from the source tip are deflected more to the bypass tips, which becomes more significant far away from the middle plane. Like the 2D simulation in section 4.1.2, all force errors caused by position and width deviations

of tips are local, as seen in Fig. 4.11 (c) and (d). Besides, the defect on one side of the tip has very little effect on the force on the other side. For example, the obvious notch on the top surface of tip 1, as seen in the inset figure in Fig. 4.10 (a), has little effect on the force distribution in the middle plane (the practically measured plane). Therefore, when the workspace is large, the effects from small shape defects of tips, such as position and size deviation and convex-concave roughness, can be neglected. Nevertheless, when the tips are in very close distance, the effective workspace of a real fluidic reservoir depends on the quality of the tips.

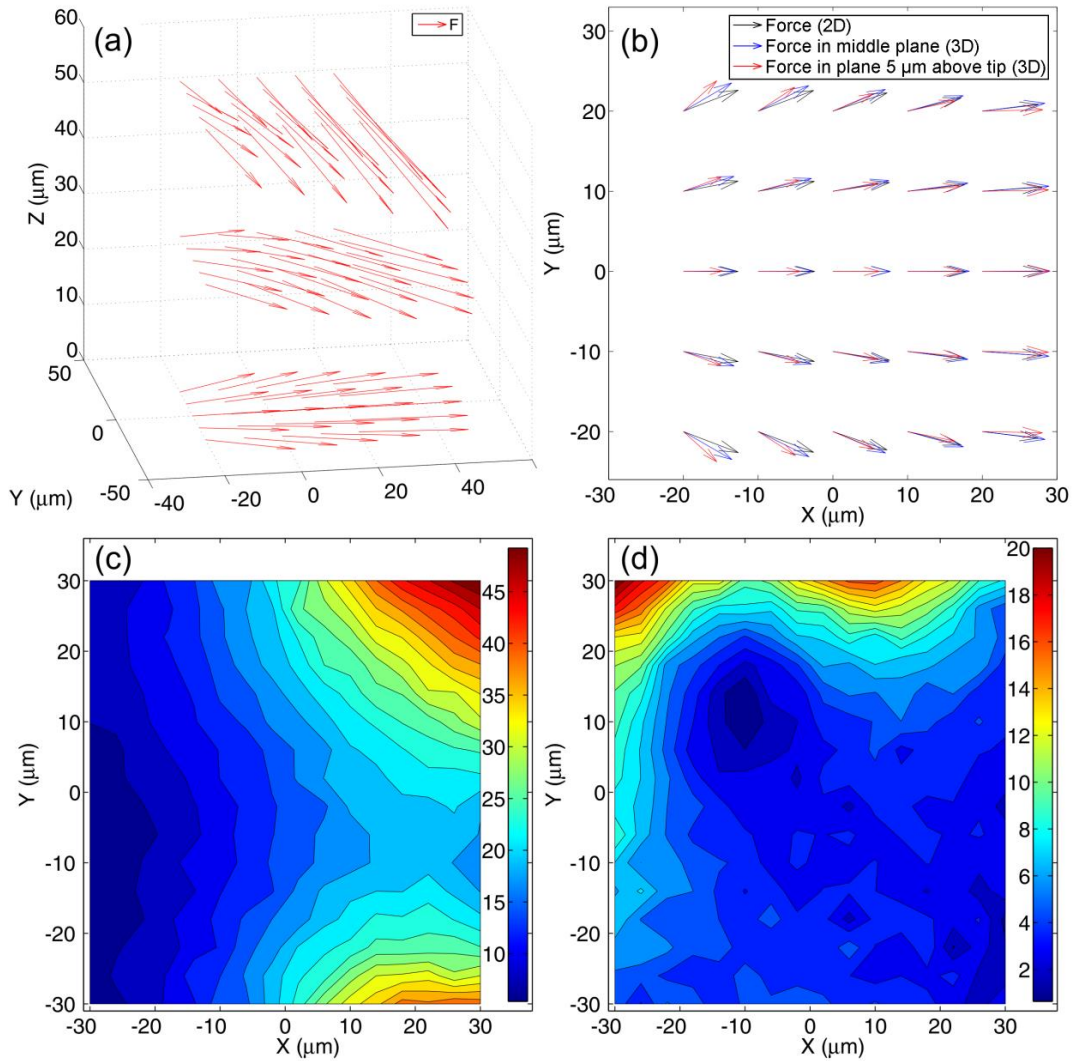


Fig. 4.11 (a) Force distributions at top plane, intermediate plane and middle plane. The right tip is set as source tip. The coil current is set to 40 Ampere turns. (b) Force distributions in different situations. The forces are scaled to the central point. (c) The force error caused by 20 μm displacement along y axis on the right tip. (d) Force error caused by left top tip, which has a width of 40 μm. (Adopted from Ref. [117].)

In reality, besides the permeability and M_s , the strength of force also depends on the thickness of the tips. As shown in Table 4.4, the force at the center of the work plane 5 μm above tip surface decreases with the thickness of the tip. The force of a 100 μm tip is a little higher in 3D simulation (1076 pN) than in 2D simulation (860 pN) and in the experiment, which may come from the different configurations. In order to avoid convergence problems due to the nonlinear material properties, the forces of 50 μm and 25 μm tips at 40 Ampere turns are scaled from 30 and 20 Ampere turns,

respectively. Although the F_H/F_O increases a little with the tip thickness, the force components located inside the work plane (F_H) decrease. This phenomenon of force reduction due to small thickness was also observed in Refs. [29, 64]. However, when the distance among tips is comparable to the thickness of the tips, this force reduction becomes negligible, which is similar to permanent magnet MT [124]. In addition, except a scaling factor, the force distribution of thinner tips in 3D simulation is more close to that of 2D simulation, which means that the 2D simulation, in case of structures with a large aspect ratio, can be adopted without inducing too much error.

Table 4.4 The tip thickness effect on force* (Adopted from Ref. [117].)

Thickness (μm)	F_O (pN)	F_H (pN)	F_H/F_O	F_V/F_H
100	1076.4	759.95	0.71	0.64
50	686.97	533.74	0.77	0.57
25	420.72	368.74	0.88	0.46

* F_H refers the force component in plane 5 μm above tip surface. F_V refers the force component in vertical direction. All the forces are deduced with a coil current of 40 Ampere turns.

4.1.4 Summary on Multi-pole Magnetic Tweezers

Among different multi-pole MTs, tri-pole MT exhibits advantages regarding high strength and good homogeneity of force. The maximum magnetic field or force of tri-pole MT can be achieved when the width of tips has the same dimension as the radius of the workspace. With an optimized MT, up to 1 nN can be applied on a 2.8 μm bead in any direction within a plane. This force is comparable to the result of Ref. [29] and amounts to about half of the force achieved by single-pole MT [56]. However, the MT here has a large workspace of $60 \times 60 \mu\text{m}^2$, which allows to achieve multi-cell measurements for high throughput.

The high power laser used in manufacturing can cause segregation and morphological roughness near the cutting edge of tips. The induced reduction in saturation magnetization and permeability plays a vital role in the high force reduction in MT. Compared to the permeability, the reduction of M_s has a stronger effect. In addition, the 3D geometry of tips also has a strong effect on the magnetic force. For example, the MT force may be reduced due to the small thickness of tips and the narrowing on the top side of the tips. All the force errors caused by the shape deviations of tip are local and decrease with increasing distance from the deformed tip. As a matter of fact, there is a trade-off among high force, maneuverability, throughput, and manufacturing issues in practical design of magnetic tweezers. For instance, although the maximum magnetic force can be enhanced by using a smaller workspace, it may deteriorate the accuracy of force (maneuverability). However, both the potential maximum force and maneuverability could be improved by optimizing the manufacturing process of magnetic tips.

4.2 Magnetic Tips Passivation

As discussed in the previous section, FeCo alloy is adopted as the material for the sharp magnetic tips because of its high saturation magnetization. However, Pouponneau *et al.* showed that magnetic part made of FeCo is corroded in a physiological solution [68]. Moreover, the metal elements such as Fe, Co, and V can induce cytotoxic effects when being released over dose into extracellular fluid [69]. Hence, in order to prevent corrosion and to improve biocompatibility for long time living cell experiment, appropriate passivation is essential.

4.2.1 Corrosion in Cell Medium

Usually, physiological fluids such as cell culture media include various salt ions. When magnetic material is exposed to these physiological fluids for some time, it may corrode, i.e. metal atoms are dissolved into the fluid. In this work, the concentrations of metal ions released in two typical cell culture media for HL-1 and HEK cells (supplemented Dulbecco's Modified Eagle's Medium) were measured. The initial ratio between surface area of magnetic tip and volume of the medium is 7.68 mm²/ml. 6 tips were immersed in the cell culture media. Liquid samples of 0.1 ml each were collected after 1 day, 2 days and 3 days *in vitro* (DIV). Then the media were refreshed. The last samples were collected after another 3 days *in vitro*. All these samples and the pure cell medium were analyzed with inductively coupled plasma mass spectrometry (ICP-MS, Agilent 7500ce, Agilent Technologies Inc., Japan). From each sample, two dilutions were prepared and measured. As shown in Fig. 4.12 (a) - (c), the concentrations of metal ions among samples collected at the same time exhibit very large fluctuations. The corrosion of Fe and Co in HL-1 medium sped up from day 4 to day 6, when no intermediate samples were collected. This corrosion acceleration phenomenon was also noticed in neuron medium, which is not shown here. However, the tips treated in HEK cell medium have slower corrosion rates, indicating passivation after first 3 days *in vitro*. It is obvious that there is a strong relation between Co and Fe corrosion. However, the concentrations of V in media did not exhibit the same tendency as Co and Fe, but become smaller during the last 3 days in all media. This agrees well with the V enrichment phenomenon observed at the magnetic material surface caused by specific processes during laser cutting, see the previous section 4.1.3. In sample HL-1-S2, the highest speed of Co and Fe corrosion was observed. As shown in Fig. 4.12 (d), there is a very obvious corrosion spot near the cutting edge of HL-1-S2 tip. Compared to Fe ions, mammalian cells are more sensitive to Co ions [69]. The Co concentration in HL-1-S2 is about 1.8 mM after 3 days *in vitro*, which is about 2 times higher than the toxicity threshold of 0.6 ~ 0.8 mM given in Ref. [69].

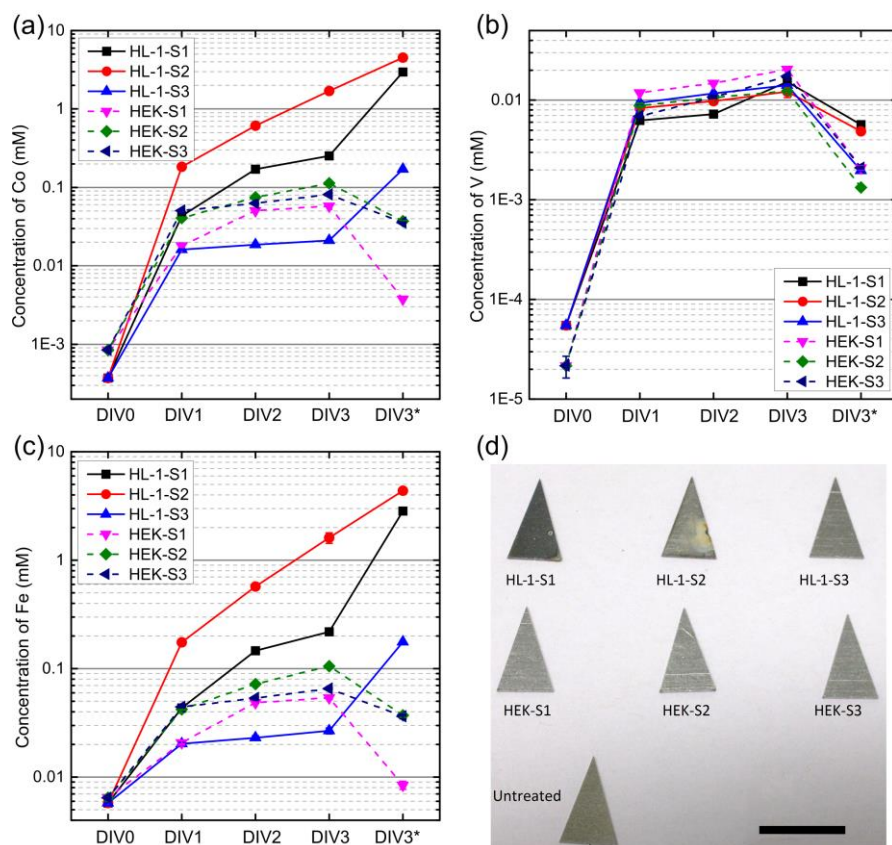


Fig. 4.12 (a) Co ion concentration. (b) V ion concentration. (c) Fe ion concentration. (d) Photo of treated and untreated tips. Scale bar is 10 mm. (Adopted from Ref. [118].)

4.2.2 Polypyrrole Coating

FeCo without passivation cannot be used for experiments with cells. Fortunately, the FeCo alloy has a good conductivity. Hence, polypyrrole (PPy), a conducting biocompatible polymer matrix that can easily be electrodeposited, is a possible candidate for passivation. The electrochemical deposition of PPy on the magnetic tips was performed utilizing a potentiostat (Bio-Logic VSP 300, Bio-Logic SAS, France). During electrodeposition, a small Ag/AgCl reference electrode (Drifref-2, World Precision Instruments, USA) was immersed into the fluidic reservoir. Before deposition, the magnetic tips were ultrasonically cleaned with acetone, isopropanol and ethanol successively, and blown dry with nitrogen. The PPy was deposited onto the magnetic tips according to Ref. [75]. The electrolyte consists of 0.35 M NaNO_3 , 0.12 M Na_2MoO_4 and 0.5 M pyrrole. The pH value of the electrolyte was adjusted to 12 with NaOH and HNO_3 . Two protocols for potential steps were applied. In the first one, 5 initial voltammetric sweeps between 0V and 0.8 V vs. Ag/AgCl with 200 mV/s were applied, and then a constant potential of 0.8 V was kept for the remainder of the 3 minute total deposition time. In the second protocol, only a constant potential of 0.8 V vs. Ag/AgCl was applied for 3 minutes. The morphology of the deposited PPy film was characterized by SEM and light microscope. The results of the electrochemical PPy deposition are shown in Fig. 4.13.

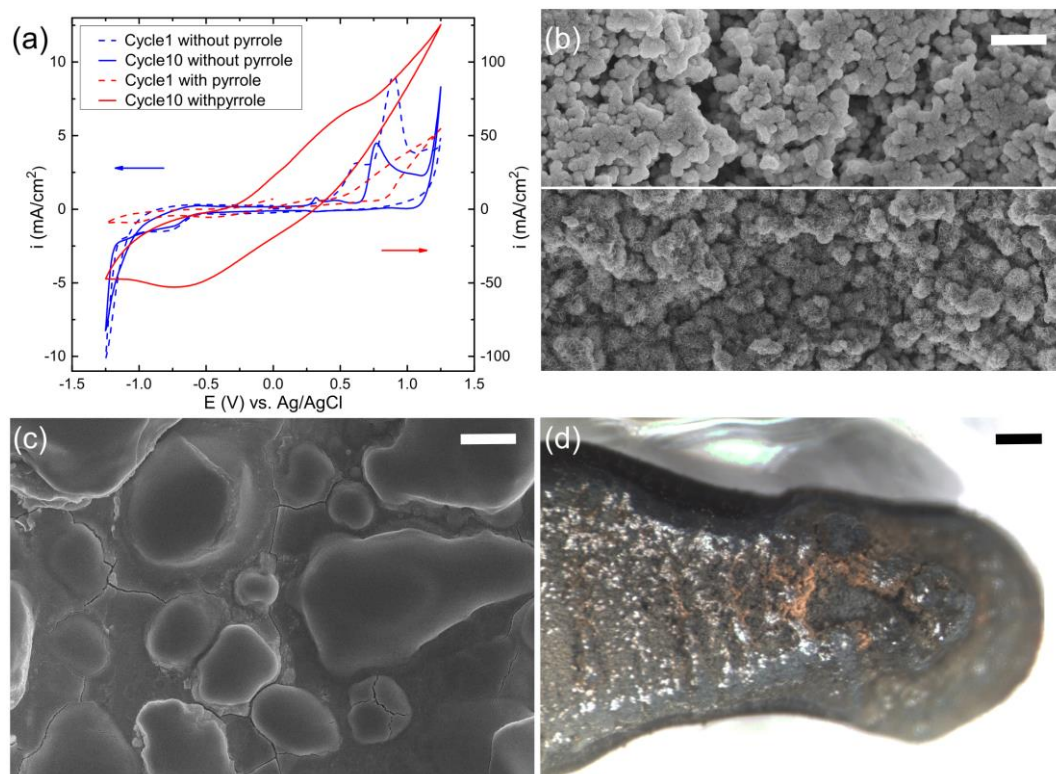


Fig. 4.13. (a) Cyclic voltammograms, with a scan rate of 50 mV/s. (b) SEM image at the middle surface of a tip with electrodeposited PPy, away from the cutting edge. The upper half was deposited with initial voltammetric sweeps before constant applied potential, the lower half with constant applied potential. (c) SEM image at an area near the cutting edge, with constant deposition. (d) Light microscope image of a tip after PPy deposition. All scale bars represent 20 μ m. (Adopted from Ref. [118].)

In the cyclic voltammograms without pyrrole (see Fig. 4.13 (a)) the oxidation peak at around 0.7-0.9 V may be related to the iron redox processes of $\text{Fe}^{2+}/\text{Fe}^{3+}$. In the presence of pyrrole, a current increase at 0.8 V denotes the onset of the pyrrole oxidation on the tip surface. As in the top half of the image in Fig. 4.13 (b), there are some holes among grains of PPy when voltammetric sweeps were applied before the constant potential. Without these potential sweeps, as presented in the bottom half of the image Fig. 4.13 (b), the quality of PPy shows some improvement. This agrees with the finding of the iron oxidation peak which moved toward low potential with time. The constant potential protocol lowered the oxidation. However, the surface of PPy was still not very tight, and can be easily peeled off with scotch tape. Especially, the morphology of PPy changed significantly at the area near the cutting edge, as shown in Fig. 4.13 (c). This can be attributed to the segmentation from laser cutting. Moreover, the deposition speed was usually faster at the sharp part than at other areas as depicted in Fig. 4.13 (d). The tip grew a PPy bulge in the front area. Besides this, there was some brown powder on the tip after deposition, which may be iron oxide.

4.2.3 Parylene Coating

Because of conformal coating and good barrier properties, parylene C is widely used for moisture isolation and anti-corrosion in electronics and medical devices. In this work, the magnetic tips were coated with 3 and 6 μ m thick parylene C. The parylene C layer was coated in a SCS Labcoater[®] 2

(PDS 2010, Specialty Coating Systems, Inc., USA) according to the distributor specifications: 1) dimers were first evaporated at 175°C, 2) dimeric gas was then introduced into the pyrolysis chamber at 690°C where they decayed into monomers, 3) finally monomers were introduced into the vacuum chamber at room temperature and react to polymerize onto the substrate. After coating, the magnetic parts were rinsed with tap water for 1 day. Then the corrosion tests were carried out. The results are shown in Fig. 4.14 (a) - (c). Compared with the uncoated tips, the numbers of metal ions released from all samples were orders of magnitude lower. Take Co for example, the concentration decreased from a few mM to the μM range, which is very close to the background concentration in the medium. It should be noted that the initial concentrations of Co and V ions in Fig. 4.14 are a little lower than the medium background concentrations at DIV0 in Fig. 4.12. This small difference may be caused by the limited resolution of the instrument. As shown in Fig. 4.14 (a) -(c), the thickness of the parylene C coating did not make any difference in its isolation performance. Therefore, a thickness of 3 μm is enough. Because of the excellent isolation, the concentrations of Co were not equal to Fe as in the uncoated tips. The vanadium concentration also did not decrease after the first 3 days.

It is well known that FeCo alloy shows a large magnetostriction, which can cause considerable strain under high magnetic fields [67, 121]. The magnetostriction will cause small deformations at the sharp tips because of the much higher magnetic field. Moreover, when a high magnetic field is applied, a significant attracting force among the tips is observed. These effects could cause failure of the isolation. In order to inspect the durability of the coating, the magnetic tips in the reservoir filled with cell medium were exposed to on-off periodic coil current pulses. Each current cycle, with amplitude of 320 Ampere turns, lasted for 10 s, with an on-off-ratio of 1:1. More than 1000 cycles were performed. The concentrations of cobalt before and after coil current cycling are shown in Fig. 4.14 (d). Although there was a small increase in the ion concentration, the amount of released ions was still very low. This good durability should be attributed to the high fracture strain of parylene C [77]. The inset in Fig. 4.14 (d) shows two samples of the reservoirs. The reservoir with two tips can be used for single direction particle actuation, and the reservoir with three tips can be used for 2D particle actuation.

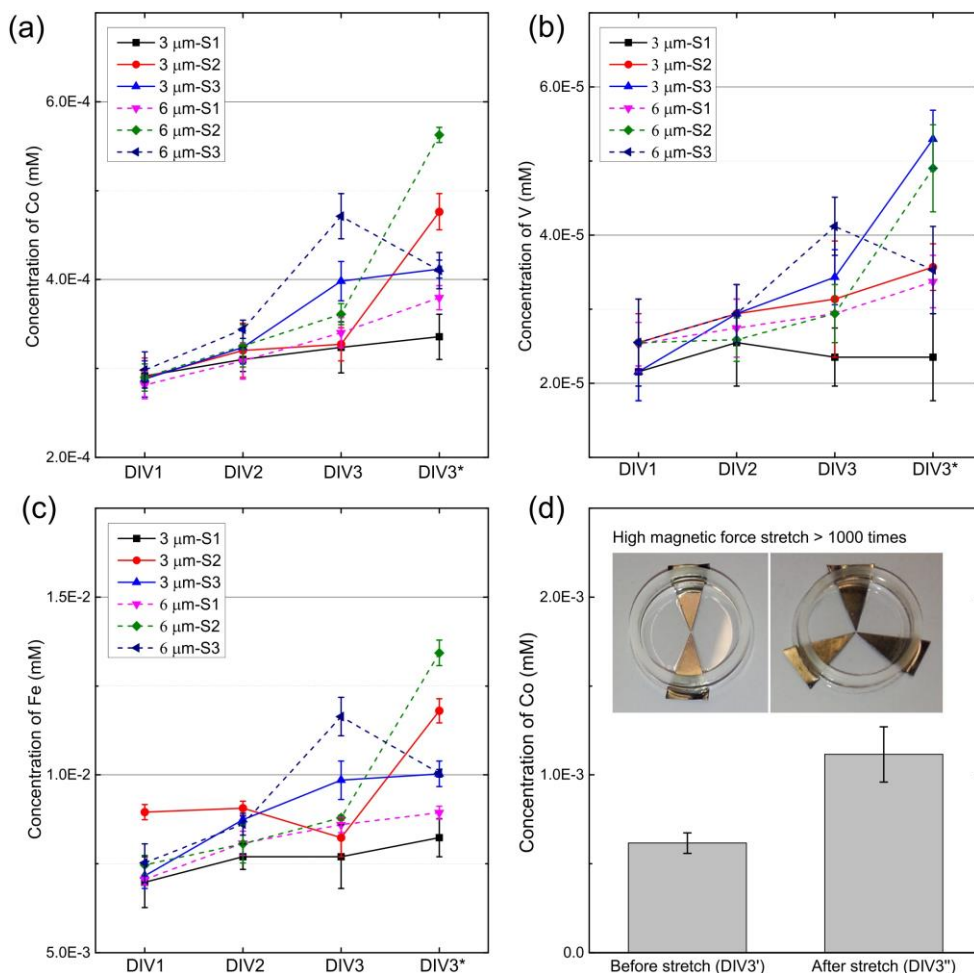


Fig. 4.14 Magnetic tips with different thickness parylene coatings were treated with HL-1 medium: (a) Co ion concentration. (b) V ion concentration. (c) Fe ion concentration. (d) High force durability test. DIV3' refers to the time from DIV7 to DIV9, and DIV3'' refers to the time from DIV11 to DIV13. The inset shows samples of reservoirs with two tips and three tips. (Adopted from Ref. [118].)

4.2.4 Cell Viability

In order to evaluate the biocompatibility of different reservoirs, the viability of HL-1, HEK-293, and primary rat neuronal cells were tested. Here, only uncoated and parylene coated magnetic tips in culture reservoirs were included in the test. The dead/living experiments of HL-1 and HEK cells were carried out after 2-3 days in culture. The neuron experiments were done after 1 week. The results are presented in Fig. 4.15. As shown in Fig. 4.15 (a) - (c), compared to the control, HL-1 cells with uncoated magnetic parts have small round body morphology and lower cell density. This indicates the pathological state and the low proliferation of cells. In the coated reservoir, HL-1 cells maintained their extended phenotype and spread well on fibronectin coated parylene C. A small fraction of HL-1 cells on these substrates exhibited large bodies. The results of rat neurons are shown in Fig. 4.15 (d) - (f). Both the neurons on control and parylene C coated samples show normal cell shape and good viability (>70%). Almost all neurons in the uncoated reservoir were dead. The existence of cell clusters was due to insufficient dispersion during cell preparation. Unlike HL-1 cells, there are a number of dead cells deposited on the samples during the initial cell plating. This is due to the isolation of the primary cells from brain tissue. Unlike HL-1 and neuronal cells, even with uncoated

magnetic parts, HEK cells still show a good viability, as presented in Fig. 4.15 (g) - (h). The result agrees well with the passivation of material found in HEK medium.

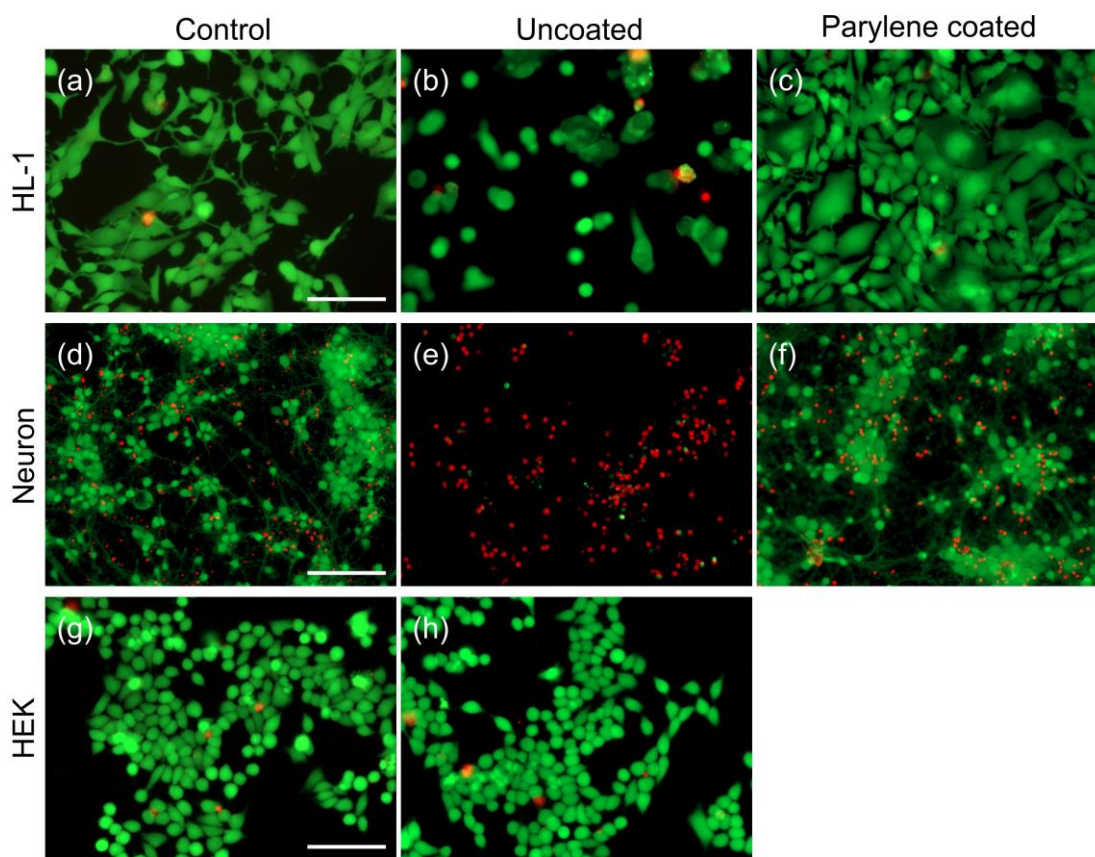


Fig. 4.15 Dead/living cell staining. All images share the same scale, the scale bars are 100 μm . The living cells are stained with calcein, shown in green. The dead cell are stained with ethidium homodimer, shown in red. (a) Control HL-1 cells cultured on a glass cover slip. (b) HL-1 cells cultured in a reservoir with uncoated magnetic tips. (c) HL-1 cells cultured in a reservoir with parylene C coated magnetic tips. (d) Control primary neuronal cells cultured on a glass cover slip. (e) Primary neuronal cells cultured in a reservoir with uncoated magnetic tips. (f) primary neuronal cells cultured in a reservoir with parylene coated magnetic tips. (g) Control HEK cells cultured on a glass cover slip. (h) HEK cells cultured in a fluidic reservoir with uncoated magnetic tips. (Adopted from Ref. [118].)

4.2.5 Summary on Magnetic Tips Passivation

Except for the HEK cell medium, obvious accelerated corrosion of magnetic tips was observed in cardiomyocyte HL-1 and primary rat neuron medium. The high concentration of Co ions released from the tips into cell culture media of HL-1 and neuron cells causes cytotoxicity in long-term culture. When coating the FeCo magnetic tips with polypyrrole, the material segregation in the area near the laser cutting edge of the tips had an adverse effect on the deposition quality. However, parylene C coating showed excellent isolation and good durability, even for high force applications. Both cardiomyocyte and primary neuronal cell can be cultured with the parylene C coated magnetic tips for a long time.

4.3 Magnetic Twisting Cytometry Based on Electromagnets

4.3.1 Configuration

As in the introduction chapter, compared to MT, MTC usually owns the advantages such as higher throughput and multi-frequency measurement. Furthermore, there is no biocompatibility problem because there is no magnetic part needed to approach closely the cell samples in MTC. In this work, the MTC is based on the previous multi-pole electromagnetic tweezers setup. The diagram of the MTC setup is presented in Fig. 4.16 (a). The control and data acquisition for twisting beads is marked with red arrows. The twisting electromagnet consists of a main hexapole yoke, a group of actuating coils and a fluidic reservoir, as shown in Fig. 4.16 (b). The fluidic reservoir containing cell samples is located on the top central area and is enclosed by the symmetric magnetic poles. As shown in Fig. 4.16 (b), any direction of in plane twisting magnetic field can be generated with different combinations of coil currents. The rotation of vertically magnetized beads under a twisting field is shown in the inset figure. The cell samples were illuminated with transmitted light. In order to decrease the distortion of bead images under high speed twisting, global shutter was employed for the image exposure. The exposure time for each image was set to 0.15 ms. Pixel binning (2×2) was used to improve the signal-to-noise ratio of image, e.g. from 26.3 (without binning) to 39.5. The displacements of beads were analyzed by the 2D cross-correlation algorithm, as in section 3.1.4. The DAQ card was used to generate sinusoidal stimuli signals, which was connected to the custom-built power amplifier to drive the twisting electromagnet. In order to achieve a high timing precision, the stimuli signals generated by the DAQ card were refreshed at 100 kHz. The DAQ card was synchronized by the camera trigger signal. Both the camera and the DAQ card were controlled via customized LabVIEW software. During experiment, the raw image data read off the camera were quickly streamed into a pre-allocated buffer. Image acquisition, image processing, and stimuli signal generation were performed in three parallel threads.

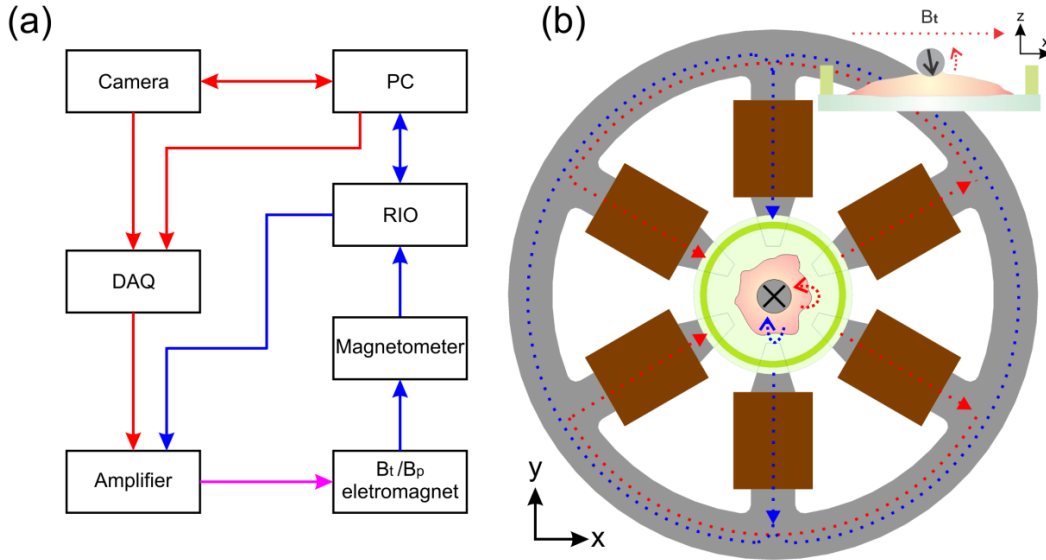


Fig. 4.16 (a) Block diagram of setup. The red arrows refer to the control/data flow of B_t , and the blue arrows denote the control/data flow of B_p . The B_t and B_p share the control/data flow depicted by the pink arrow. (b) Schematic of the twisting apparatus. Coils, yoke and fluidic reservoir are depicted in brown, grey and green, respectively. The red and blue dotted lines in the yoke show the magnetic flux of two orthogonal sample twisting fields. The inset shows the rotation of a vertically polarized bead under a twisting field. The fluidic reservoir is composed of a cover slip and a glass ring. The parts in the drawing are not to scale. (Adapted from Ref. [119].)

4.3.2 Heterodyning Technique

In MTC, the positions of beads during twisting are detected by the optical camera. According to the Nyquist sampling theorem, the bead movement can be only detected when the camera acquisition frequency is at least equal or larger than 2 times of the frequency of magnetic twisting field, as in Fig. 4.17 (a). However, when the bead movement is periodic like sinusoidal, it can be detected by choosing a special camera acquisition frequency and magnetic twisting frequency even the twisting frequency is higher than the camera frequency, as in Fig. 4.17 (b). The amplitude and the phase lag of bead displacement can be deduced by fitting to the formula $d \times \sin(\omega t + \phi)$ like in the low frequency. This method is also called as heterodyning technique. Within this technique, the operation between different devices should be synchronized very accurately. Besides, the frequency resolution and stability of both stimuli and detection are very important to the measurement precision. Although the maximal jitter of the camera is about $1 \mu\text{s}$, which is larger than the DAQ card's ($\sim 50 \text{ ns}$), it is accurate enough for detecting a signal with frequency $\leq 1 \text{ kHz}$.

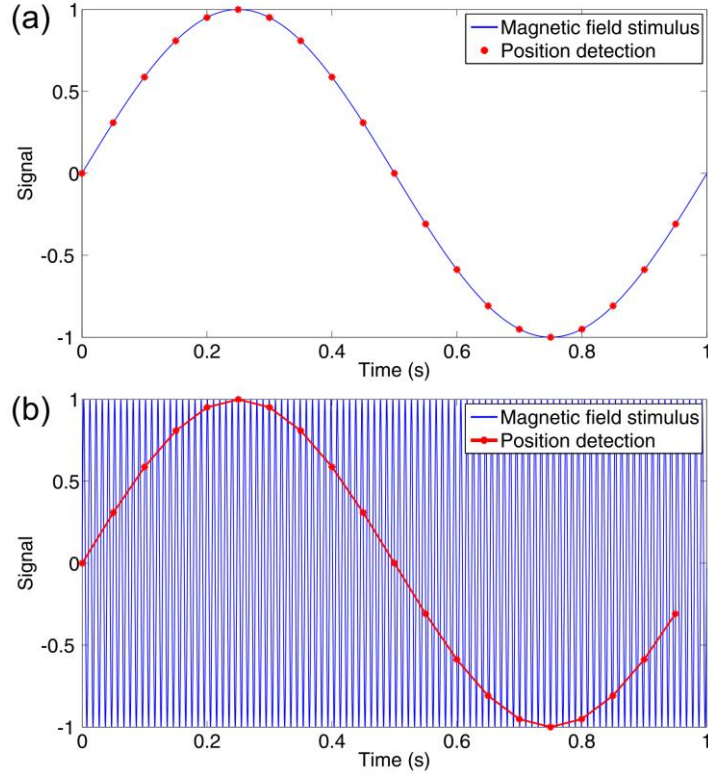


Fig. 4.17 (a) Low magnetic field stimulus frequency, (b) high magnetic field stimulus frequency.

The pre-set measurement parameters used in this work are listed in Table 4.5. The camera acquisition frequency f_A is set according to the twisting frequency f_T as

$$f_T - Nf_A = 1 / T_M \quad (4.2).$$

Here, N denotes a integer multiple and T_M is the measurement period. Only when f_T is larger than 3 Hz, the heterodyning technique is adopted. The camera is set to work at the highest speed to make the measurement time as short as possible. As in the Table 4.5, the number of images for each frequency measurement is deduced from $f_A \times T_M \times \text{cycles}$.

Table 4.5 Heterodyning technique: frequency, cycle, period. (Adopted from Ref. [119].)

Twisting frequencies	0.03	0.1	0.3	1	3	10	33	98	338	962
Acquisition frequencies	0.96	3.2	9.6	32	48	9.6	32	48	48	48
Measurement cycles	3	3	3	3	5	5	5	10	20	20
Measurement periods	100/3	10	10/3	1	1/3	2.5	1	0.5	0.5	0.5
Image numbers	96	96	96	96	90	120	160	240	480	480

4.3.3 Magnetic Field

In practice, the cell sample can be either cultured on a cover slip, then placed into a fluidic reservoir for measurement, or also can be cultured directly on the fluidic reservoir. Before measurement, the magnetic beads were bound on the cells and magnetized in a high vertical magnetic field, which was generated with the polarization electromagnet (see inset in Fig. 4.18 (c)). This polarization electromagnet is made of common St37 construction steel with a 5 mm gap in the yoke serving as the workspace. In one corner of the workspace, there is a small hall sensor installed. A feedback control loop based on the multifunction RIO card was implemented, which allows the device to achieve a magnetic field accuracy of 0.5 G. The items used for magnetizing the beads are marked by blue arrows in Fig. 4.16 (a). Both the twisting and polarization electromagnet share the same multi-channel power amplifier.

In MTC, it is important to generate a uniform magnetic field. With a homogeneous magnetic field, both torque error and the effect from a pulling force caused by the gradient field as in MT, can be reduced. In this work, the magnetic field distributions in the workspaces of twisting and polarizing electromagnets were examined by using finite element simulation. In order to decrease the leakage of magnetic flux, the 6 poles of the twisting electromagnet were paired into 3 groups of oppositely oriented poles. As shown in Fig. 4.16 (b), for example, the pair of poles along the y axis is used to generate a magnetic field along the y axis. The corresponding magnetic field distribution is presented in Fig. 4.18 (a). The maximum magnetic field variation within $1 \times 1 \text{ mm}^2$ is less than 2%. With a coil current of 100 Ampere turns, the magnetic field at the center of the simulation and in the experiment (measured by Gauss meter), are 80.8 and 83 G, respectively. The small difference between simulation and experimental measurement may originate from the approximation of the simulation geometry and from the practical position of the magnetic probe in the measurement which amounts to about 1 G accuracy in measurement. The magnetic field along the x axis can be generated adopting 2 pairs of poles with the same coil current, as shown by the red dotted lines in Fig. 4.16 (b). If the magnetic field is generated by two pairs of poles, it has a better uniformity than in the case of a single pair of poles, as shown in Fig. 4.18 (b). For example, the magnetic field variation within $1 \times 1 \text{ mm}^2$ is less than 0.7% when using two pairs of poles. In addition, the magnetic field changes more slowly along the y axis. Thanks to the large gap (10 mm) between the yoke poles, the planar twisting magnetic field also changes slowly along the z axis (vertical). For instance, the magnetic field B_y^0 only decreases about 2.7 % at a distance of 0.5 mm above the fluidic reservoir. In addition, the torque applied on the beads also depends on the magnetic moment of the beads. In order to obtain the maximum magnetic moment, the polarization magnetic field should be strong enough to magnetize the ferromagnetic beads along its main $M-H$ loop. In this situation, the final magnetic moment of the beads does not depend on the strength of the polarization field any more. Hence, it is very important to magnetize all the beads in the same direction. As shown in Fig. 4.18 (c), it is obvious that the magnetic field in the polarization electromagnet exhibits a very well defined direction in the central workspace. The

directional variation of the magnetization field is less than 1 degree in the central $15 \times 15 \text{ mm}^2$ area. The maximum off-vertical field is located near the edge of the yoke. The ratio of magnetic field to coil current in the workspace is about 1000 G/400 Ampere turns for the polarization electromagnet. Besides this, there is a non-negligible remnant magnetic field after the coil current is turned off because of the hysteresis of the steel core. In order to reduce this effect, the feedback control is activated to set the magnetic field to zero after bead magnetization.

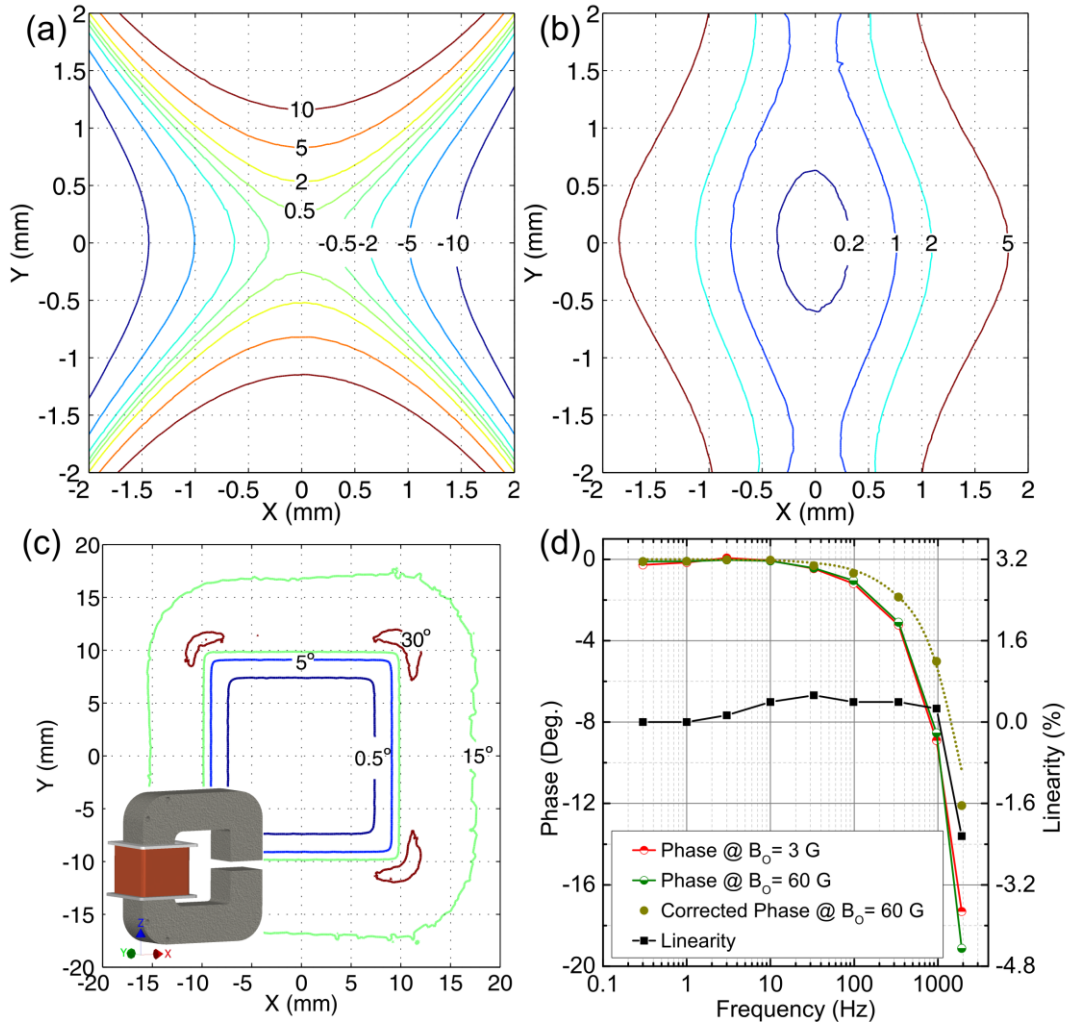


Fig. 4.18. (a) The variation of magnetic field $((B_y - B_y^0)/B_y^0, \text{ in percent})$ along y axis. The workspace center is defined as O. (b) The variation of magnetic field $((B_x - B_x^0)/B_x^0, \text{ in percent})$ along x axis. (c) The variation of magnetic field direction in the polarization electromagnet. The inset depicts the mechanical drawing of the polarization electromagnet. (d) Phase shift and linearity of twisting magnetic field. The linearity is calculated according to the magnetic field at 1 Hz. The phase shift represented by the red and green lines includes all parts: yoke, amplifier and magnetometer. The brown dots represent the corrected phase shift in which the contribution from the magnetometer was removed. The brown dotted line shows the fitting of the phase shift below 1 kHz to a single pole transfer function. (Adopted from Ref. [119].)

In addition to the static features, the dynamic properties of the twisting field also have significant influence on the measurement results. Because of the loss modulus feature of the cells, the response from the cells usually has some phase lag. Therefore, any phase error caused by the setup should be canceled out. For the twisting magnet, the phase shift and linearity of the magnetic field at different frequencies are shown in Fig. 4.18 (d). Thanks to the multi layer structure of the yoke, the phase lag at

low frequencies (<100 Hz) is very small. The linearity is also very good at all frequencies below 1 kHz. For frequencies below 1 kHz and magnetic fields below 100 G, the phase lag and the linearity are almost independent of the strength of the magnetic field. With higher frequency, the phase shift increases quickly and deviates from the single pole model behavior. This large phase lag is caused by the eddy current effect, which increases quickly at high frequencies [125].

4.3.4 Summary on Magnetic Twisting Cytometry

Based on the hexapole electromagnet used in the MT setup, a 2D optical MTC functionality for twisting ferromagnetic beads has been extended, in which both the strength and direction of the twisting field can be controlled. In the MTC, thanks to the high performance twisting electromagnet and the heterodyning technology, good linearity and small phase error can be achieved for frequencies up to 1 kHz when the twisting field is less than 100 G. In the other hand, an electromagnet with magnetic field feedback control was adopted to polarize the bead. With this method, it is easy to achieve a high polarization field in order to obtain a high remain magnetic moment.

4.4 Characterization of Cell Mechanics with High Throughput Magnetic Microrheometries

4.4.1 Characterization of Cardiomyocyte Mechanics with Magnetic Tweezers

As in the section 4.1, based on the optimized tri-pole magnetic tweezers, forces higher than 100 pN can be applied on small beads (Dynabeads® MyOne Carboxylic Acid, Thermo Fisher Scientific Inc., USA) in a workspace of $60 \times 60 \mu\text{m}^2$. This makes the study of stiff cell like HL-1 cell possible, and also allows to address multi-cell measurement, which helps to reduce sample to sample variability and increase throughput. An illustration of this experiment setup is shown in Fig. 4.19 (a). In order to achieve high force, the cover slip was flipped upside down on the magnetic tips in experiments, as depicted in Fig. 4.19 (a). With the amide bonding reaction of carboxylic acid and the small size (1 μm in diameter), the beads MyOne bound to proteins and were easily endocytosed by the cardiomyocyte HL-1 cells in culture. The real position of the beads had been checked by focused ion beam - scanning electron microscope (FIB - SEM). As depicted in the inset of Fig. 4.19 (b), 3 beads piled above 3 other beads were in the cortex region of the cell. However, there were also some beads bound on the surface of the cells. And because of the activated surface of the beads, a few beads adhered on the substrate with the help of the cell medium (marked with a red circle in Fig. 4.19 (b)), which can be distinguished by the response time of bead to the applied force. The bead bound on the substrate responded faster than the resolution of the optical detection.

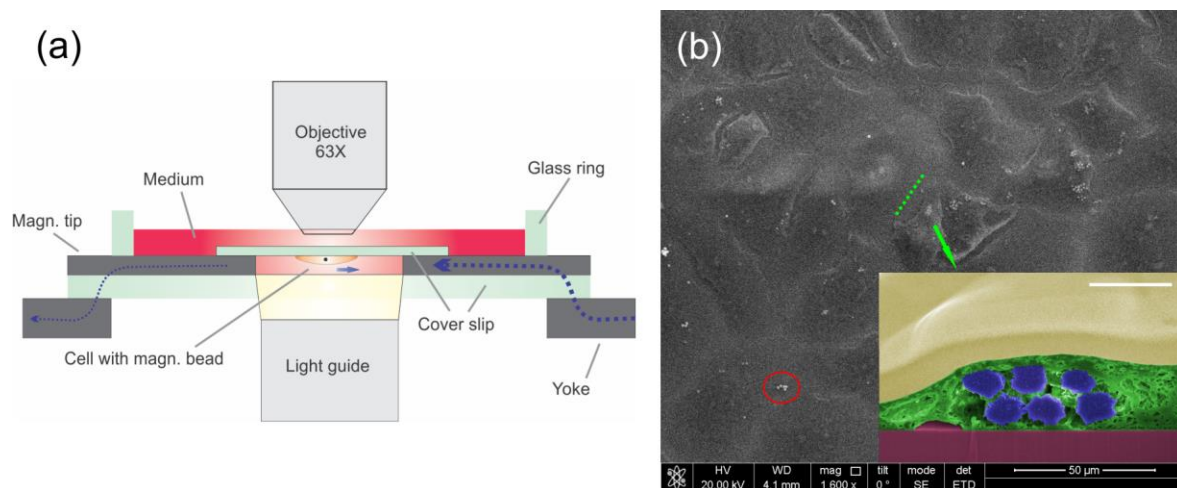


Fig.4.19. (a) Schematic of the setup. The blue dashed lines illustrate the magnetic flux. (b) SEM image of HL-1 cells cultured on a $10 \times 10 \text{ mm}^2$ silicon wafer substrate. The bright dots indicate magnetic beads. The beads in the red circle are located on the surface of the substrate in an area without cell coverage. The inset depicts a cross section after FIB cutting which was prepared parallel to the green dashed line. Pt deposition layer, cell material, magnetic bead, Si substrate are shown respectively in yellow, green, blue, red. The scale bar for inset figure is $2 \text{ }\mu\text{m}$. (Adopted from Ref. [116].)

Actually, the beads' positions can be confirmed roughly in SEM by using different electron acceleration voltages. For example, the beads on the surface are usually brighter, and the beads in cells are dim and blur in contrast and only visible under high energy electrons, as shown in Fig. 4.20 (a) - (b). Compared to the small bead MyOne, the endocytosis efficient of larger magnetic beads, such as Dynabeads[®] M-270 Epoxy ($2.8 \text{ }\mu\text{m}$ in diameter, Thermo Fisher Scientific Inc., USA), is much lower, as seen in Fig. 4.20 (c) - (d). The results obtained with Dynabeads[®] M-270 Carboxylic Acid were very similar (not shown here).

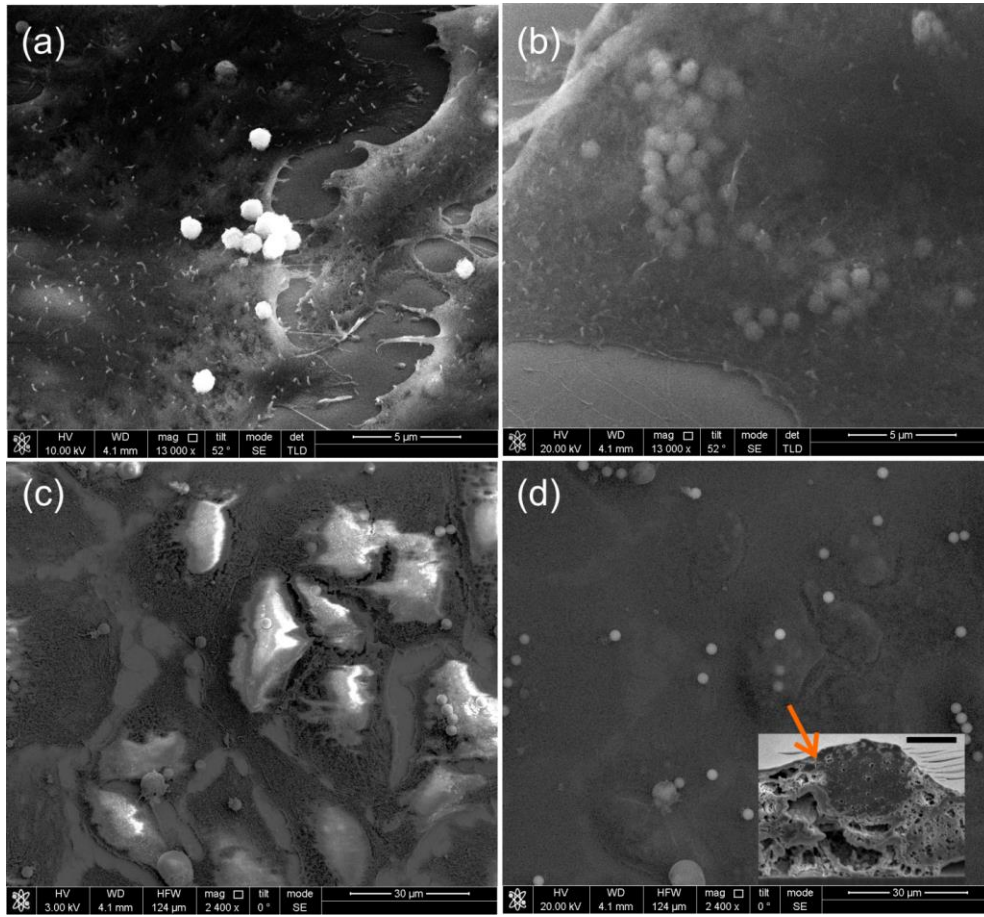


Fig.4.20. (a) - (b) SEM images of MyOne beads taken with low voltage and high voltage respectively. (c) - (d) SEM images of M-270 Epoxy beads taken with low voltage and high voltage respectively. The inset of (d) shows a FIB cutting, of which the scale bar is 1 μm .

Fig. 4.21 (a) depicts a light microscope image of a measured sample. The images acquired during the experiment were analyzed with the customized multi-bead tracking algorithm. Only single beads were analyzed, bead clusters were ignored. In order to avoid possible interference from the neighboring bead clusters, bead 8 and bead 9 were also not included in the result. The responses of beads 6 and 1 are shown in Fig. 4.21 (b). There are usually some “slips” in the first spikes which may come from the loose linkage between the bead and the cytoskeleton [126]. Therefore, only the second or third spikes were analyzed in data processing. Here, the linear viscoelasticity model was used to describe the cell mechanics. The bead creep response is fitted to Eq. 2.11, of which the mechanical model is shown in the inset of Fig. 4.21 (d). A total of 99 beads were analyzed. Both viscosity (η_0) and shear elastic modulus (μ) show an approximately log-normal distribution, as seen in Figs. 4.21 (c) and (d). This may derive from the high heterogeneity and intrinsic large variation of cell cytoskeletons. It was found that the 69 out of 99 beads that were taken up in high cell density cultures (>80% coverage) encountered stiffer mechanical properties, i.e. a geometric mean viscosity of $\eta_0 = 209.83 \pm 3.01 \text{ Pa s}$, a geometric mean shear elastic modulus of $\mu = 48.33 \pm 2.2 \text{ Pa}$, and a relaxation time of $\tau = 0.171 \pm 0.157 \text{ s}$. Moreover, 5 of the beads were found to be out of measurement range, of which the displacements were too small. This could be because the stiffness was too high or the particles

were bound on the surface of the cell. In contrast, the other 25 beads that were found in less dense cell cultures ($< 50\%$ coverage) exhibited $\eta_0 = 136.20 \pm 1.81$ Pa s, $\mu = 35.64 \pm 2.05$ Pa, and $t = 0.247 \pm 0.152$ s.

Student's t-test was used to test the statistically significant differences in the parameters. The significant (probability of the difference occurring by chance > 0.9824) observed stiffness increase with higher confluence probably originates from the cytoskeleton architecture remodeling and intracellular prestress reinforcing after cell-cell adhesions [6, 18]. However, the resultant mechanical parameter values such as elastic modulus are much lower than the results obtained in primary cardiac myocytes measured by atomic force microscopy [127, 128]. This difference may be due to the following facts: 1) these two methods actually characterize different cell regions which have different stiffness, as discussed in Ref. [126]. 2) The mechanical measurements are usually strongly dependent on how the mechanical model describes the linkage between the probe and cell cytoskeleton [18]. 3) The cytoskeleton structure of HL-1 cells is different from the adult primary cells'.

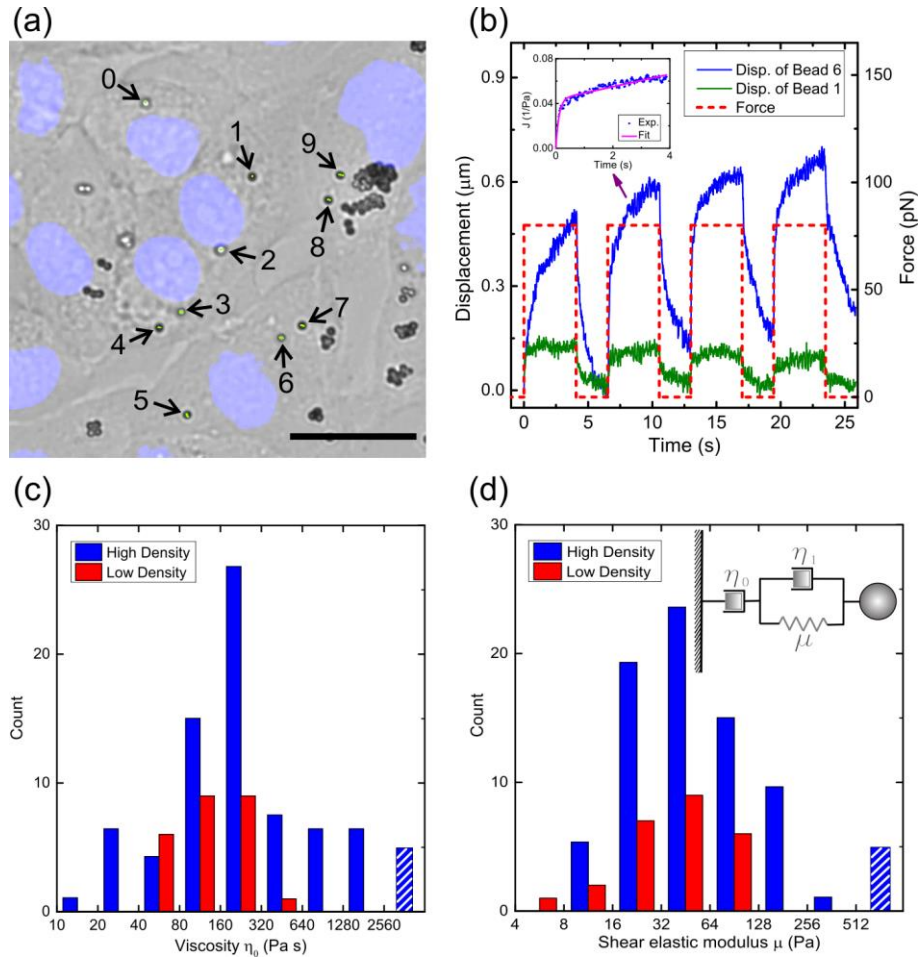


Fig. 4.21. (a) Multi cells measurement. The blue spots represent the cell nuclei stained with DAPI. The scale bar is 20 μm . (b) Displacement responses of beads 6 and 1 according to the applied force sequence. The inset depicts the second spike response of bead 6 and its fitting to the mechanical model, Eq. (2.11). (c) Viscosity η_0 distribution of 99 measured beads. The 5 beads out of range are indicated by the hatched bar. (d) Shear elastic modulus μ distribution of 99 measured beads. The 5 beads out of range are indicated by the hatched bar. The inset shows the adopted mechanical model. (Adopted from Ref. [116].)

With the help of good maneuverability in the multi-pole MT, obvious heterogeneity of cell mechanical properties was also observed. As shown in Fig. 4.22 (a), when the bead was actuated towards the nucleus, the response became stiffer. This effect can be interpreted by a denser actin meshwork and stress fibers close to the nuclei [126, 129]. Besides, there was an active response along the y direction. Unlike the regularly striated morphology of muscle tissue *in vivo*, the individual HL-1 cells cultured on glass still have a more radially organized cytoskeletal structure [129]. In the protruding part of the cell, the stress fibers usually align, by which the cytoskeleton could anchor tightly with extracellular matrix and contribute to the protrusion. As seen in Fig. 4.22 (b), it is obvious that the elasticity is different in the directions parallel and perpendicular to the cell protrusion.

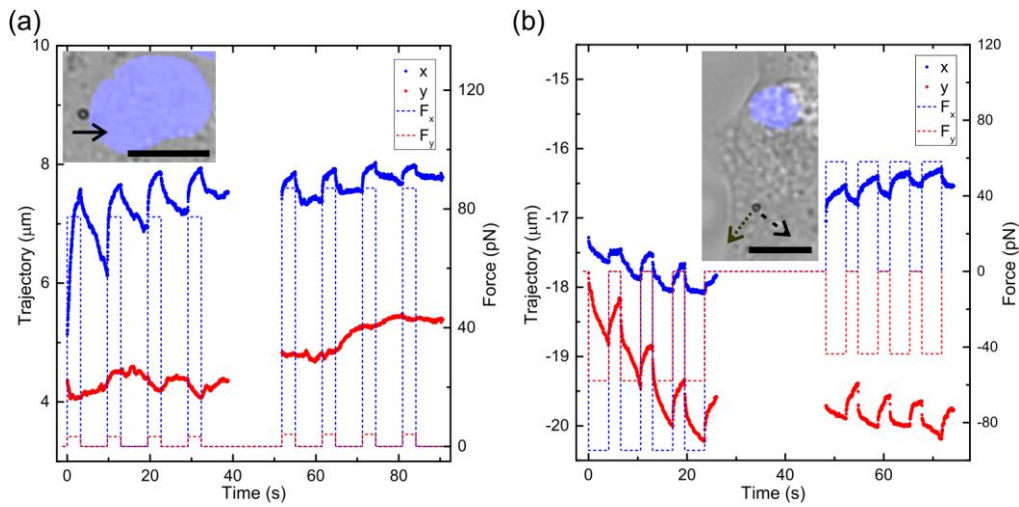


Fig. 4.22. Applied force sequence (dashed line) and observed particle trajectories (symbols) in horizontal x and vertical y direction in case of (a) a particle close to the cell nucleus (the arrow shows the force direction) and (b) in the protrusion far away from the nucleus (the dotted arrow shows the force along the protrusion, the dashed arrow shows the force vertical to the protrusion). Both scale bars are $10\ \mu\text{m}$. (Adopted from Ref. [116].)

4.4.2 Characterization of Cardiomyocyte Mechanics with Magnetic Twisting Cytometry

In MTC experiment, a microscope image of the HL-1 cells within workspace is shown in Fig. 4.23 (a). Limited by the size of the camera sensor and the magnification of objective ($40\times$), the actual measurement area was $300\times 300\ \mu\text{m}^2$. Although there were some beads in clusters, most beads were distributed over the cells evenly and adhered on their surface. In the bead movement analysis, like in the previous MT experiments, only the individual separated beads were considered. The bead clusters and the beads sitting near the edges of cells were ignored. Because this type of ferromagnetic bead has a large size distribution, very big and very small beads were also not included in the analysis. Fig. 4.23 (b) shows a SEM image of HL-1 cells with bound beads. The bead at the right of the image has a larger size than the other beads. The individual beads clearly show different embedding depths. The beads near the periphery of the cell body usually have a weak bonding with their cell, as shown in the inset.

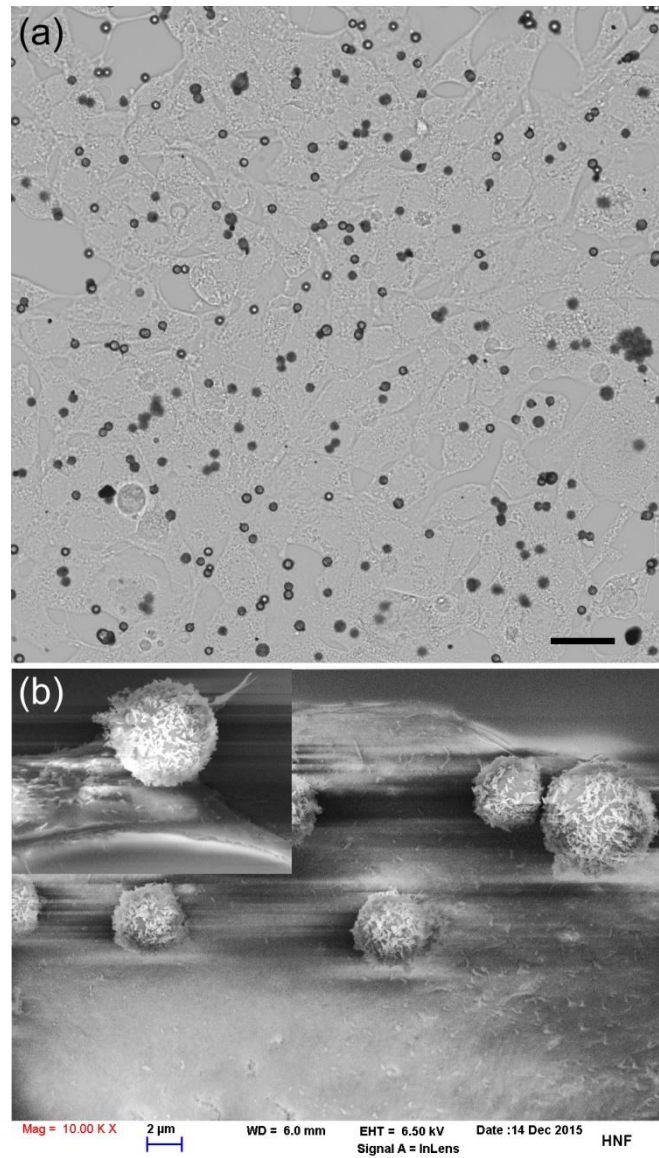


Fig. 4.23. (a) Microscope image of cells within workspace. Scale bar 30 μm . (b) SEM image of beads on HL-1 cell. Inset shows a bead bound on the periphery of a cell. (Adopted from Ref. [119].)

Before measurement, the sample was first magnetized vertically using a 2000 G magnetic field produced by the polarization electromagnet. Then the sample was transferred to the twisting apparatus. A group of specific frequencies as listed in the Table 4.5, which range from 0.03 Hz to 962 Hz, were used for twisting the beads. The beads with displacement larger than 2 μm or less than 10 nm were not included in the statistics. Displacements larger than 2 μm indicate that the beads failed to adhere to the cells. Displacements below 10 nm are too small to achieve accurate measurements. Moreover, only the beads with a phase lag falling into the range from 0 to -90 degree were considered. In order to decrease the effect from magnetic relaxation [80], the whole measurement process was finished in less than 10 minutes. As presented in Fig. 4.24 (a), the amplitude of bead displacement at different frequencies increases proportionally with the twisting magnetic field. However, the phase lag has a larger fluctuation when $B_t < 30$ G. This may be caused by the small displacement of the beads, which is close to the detection limit. Therefore, in this work, a twisting field B_t of 30 G was used unless indicated otherwise. As in Fig. 4.24 (b), the mechanical properties of single HL-1 cell are anisotropic

along different directions, in agreement with the previous result found within magnetic tweezers. The amplitude of bead response also obeys a log-normal distribution, see Fig. 4.24 (c). In addition, both the displacement distribution and the phase lag distribution can be fit by Gaussian functions very well, as shown in Fig. 4.24 (c) - (d).

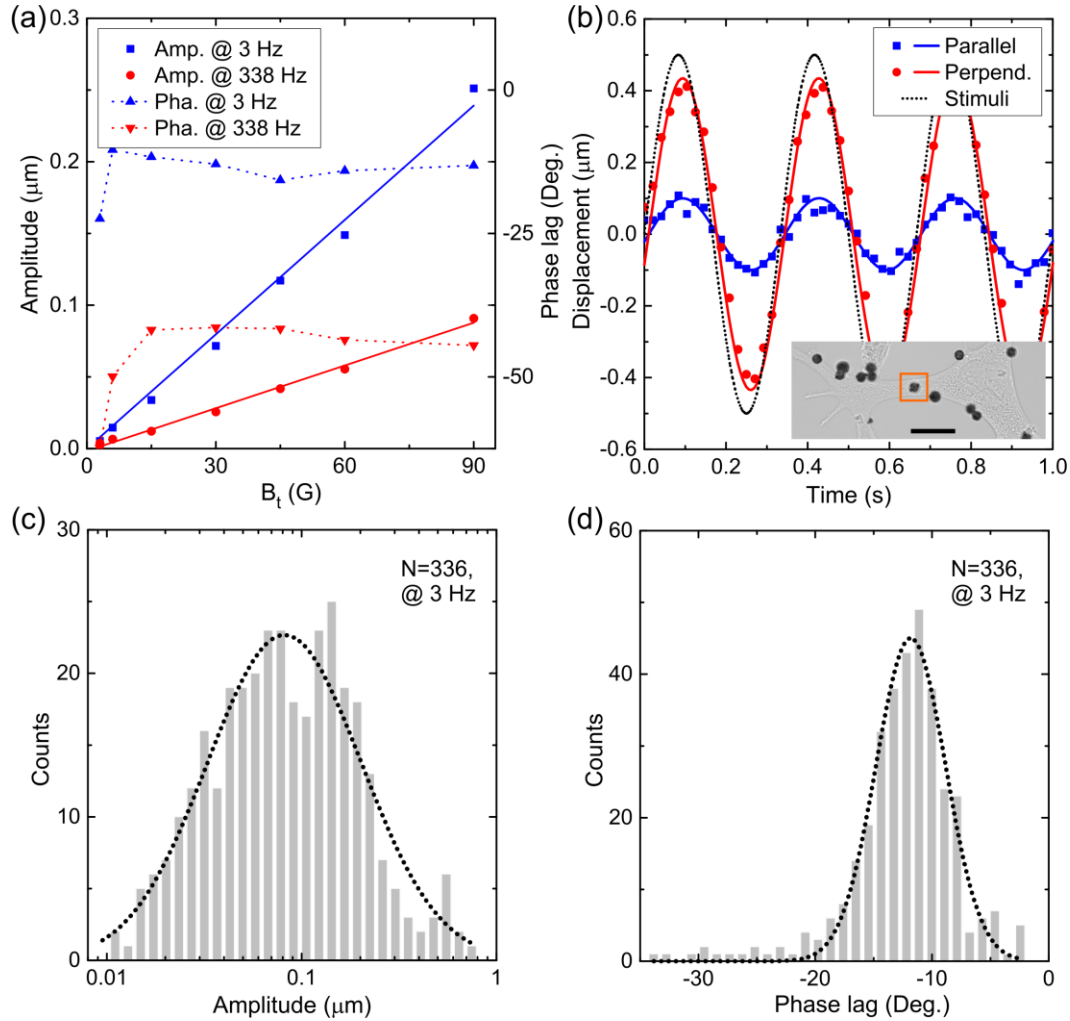


Fig. 4.24. (a) The dependency of displacement amplitude and phase lag on the twisting field B_t . (b) Bead responses in the parallel and perpendicular direction of the cell protrusion. The data is from the bead in the orange box in the inset image. The scale in the inset image is 20 μm . (c) The displacement distribution of the beads, of which the histogram is fit by a Gauss function (dot line). (d) The phase lag distribution of the beads, of which the histogram is fit by a Gauss function (dot line). (Adopted from Ref. [119].)

In MTC, the magnetic bead is bound to the cells intracellular cytoskeleton via the cell receptors of extracellular matrix such as integrins. Hence, the response of bead reflects the mechanical properties of the cell. The specific torque on the bead can be defined as the mechanical torque per unit bead volume [130]. For convenience, it can be written as

$$T = cB_t \cos\theta \quad (4.3).$$

Here, c is a constant factor; θ refers the angle between the bead's magnetic moment and the twisting field. The ferromagnetic beads used in this work have a mean diameter of 4.47 μm . When the polarization field B_p is as high as 2000 G, the maximum residual magnetic moment of $4.3 \times 10^{-13} \text{ Am}^2/\text{bead}$ can be obtained [131]. With these data, the parameter c can be deduced as 0.93 Pa/G.

Here, the soft glassy rheology (SGR) model, as in the section 2.2, was used to describe the frequency-depended mechanical properties of HL-1 cell. In order to obtain the traditional elastic shear (G') and loss (G'') moduli, a geometric factor α is usually adopted [130], by which the complex elastic modulus can be deduced from the bead displacement ($\tilde{G} = \alpha T / \tilde{d}$). However, according to the Ref. [132], the geometric factor strongly depends on the local geometry of the cell and on the degree of bead embedding. Actually, the bounding between bead and cell is different among each bead, as shown in Fig. 4.23 (b). For simplicity, in this work, the geometry factor of $\alpha = 6.8$ was taken for all beads as used in Ref. [31], which is based on the assumption that 10% of the bead diameter is embedded in a 5 μm high cell. As in Fig. 4.25 (a), according to the Eq. 2.15, the blue solid and dashed lines denote the fitting results of real and imaginary parts of elastic modulus of the control HL-1 cells, respectively. The median values of 336 beads at different frequency were used for this fitting. The best estimation of parameters for the control cells is: $G_0=1.850 \times 10^4$, $\Phi_0=2.748 \times 10^7$, $x=1.15$, and $\mu=0.954$. At low frequency range (< 1 Hz), an obvious stiffening phenomenon in loss modulus was observed, which deviates from the mechanical model. Compared to the other types of cells [31], the HL-1 cardiomyocytes exhibit a higher meta-stability of intracellular interactions or a lower agitation (small x). Similar to the finding in Ref. [31], the values of G_0 and Φ_0 can be regarded as invariants for the same type of cell under different experimental conditions. Therefore, only the parameters x and μ were taken as free fitting variables. The parameters G_0 and Φ_0 were fixed to the values obtained from the control sample. The detailed fitting results are shown in Table 4.6. The SSE is the sum of the squared differences (in log scale) between each experimental measurement and the SGR model's prediction. The parameter r^2 reflects the quality of fitting, of which the value closer to 1 means better fitting to the data. As shown in Fig. 4.25 (a), after the treatment with blebbistatin, the cells were softened by $\sim 20\%$. Moreover, after the inhibition of myosin, the stiffening at low frequency disappeared. This indicates that the stiffening mainly depends on the prestress generated by myosin activity. Besides, the cells become more fluidlike, both the viscosity and parameter x of the cells increased, as seen in Table 4.6. Unlike blebbistatin, the stiffness of cells increases quickly after fixation by paraformaldehyde. Although the twisting field B_t was set to 60 G, only 74 beads out of 185 chosen beads fell in our measurement range, whereas the ratio of valid beads to total beads in control cells was 336/420. The main reason for disqualification was failure to meet the minimum displacement threshold of 10 nm. The cell elastic shear modulus also showed a small dependence on the frequency, which is assumed to be a more solid-like behavior.

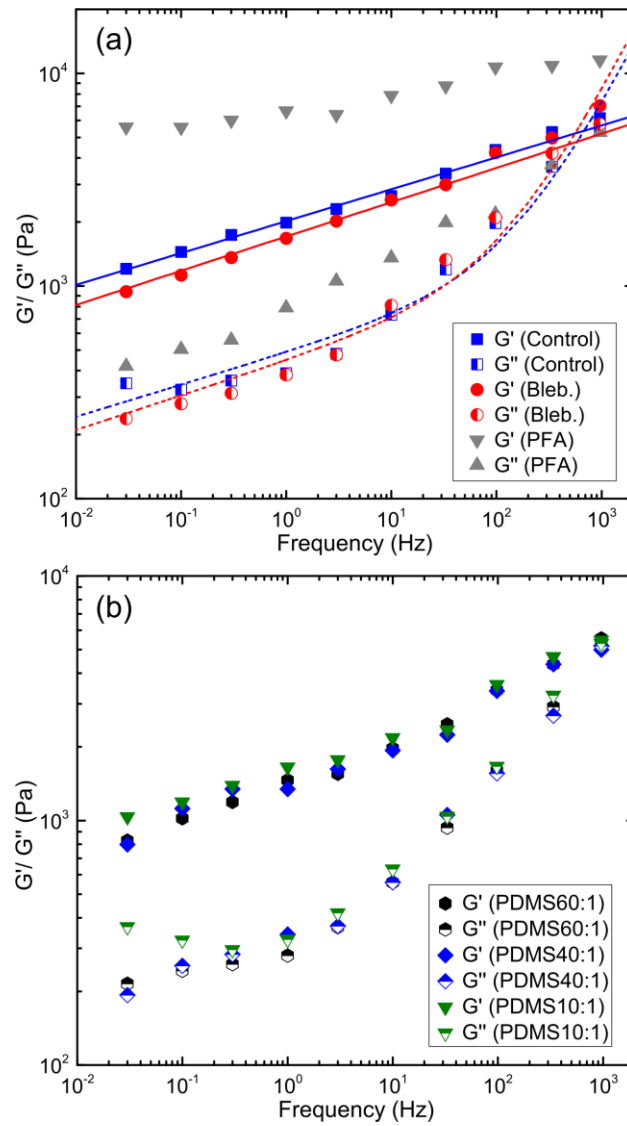


Fig. 4.25. (a) The elastic shear moduli and loss moduli of control HL-1 cells ($N = 336$ beads), blebbistatin ($50 \mu\text{M}$) treated cells ($N = 188$), paraformaldehyde (4%) treated cells ($N = 74$). The blue and red lines (dot) represent the fitting results according to SGR model for control and blebbistatin treated cells, respectively. (b) The elastic shear moduli and loss moduli of HL-1 cells cultured on substrates with PDMS60:1 ($N = 149$ beads), PDMS40:1 ($N = 244$), and PDMS10:1 ($N = 258$). (Adapted from Ref. [119].)

In this work, the substrates PDMS10:1, PDMS40:1 and PDMS60:1 exhibit a stiffness above, close and below the physiological heart stiffness, respectively [133]. As seen in Fig. 4.25 (b), the stiffening effect at low frequencies only happened on the hard substrate PDMS 10:1, which was similar to the control cell. However, the mechanical properties of cells cultured on different PDMS substrates show a very small variation, as seen in Table 4.6. This agrees with the finding that the cardiomyocytes from late embryos show adaptation to different stiffness conditions [134]. The parameter x decreased slightly with the substrate stiffness. The cells showed the smallest viscosity when grown on the PDMS40:1 substrate, which represented the optimal (physiological) stiffness for beating in a view of energy efficiency.

Table 4.6 Mechanic model fitting results

	x	μ	SSE	r^2
Control	1.150	0.954	0.346	0.973
Bleb.	1.161	1.137	0.540	0.967
PDMS (10:1)	1.164	0.819	0.543	0.957
PDMS (40:1)	1.175	0.730	0.313	0.978
PDMS (60:1)	1.176	0.794	0.389	0.975

4.4.3 Characterization of Brain Cells Mechanics with Magnetic Tweezers

Via binding the fibronectin coated magnetic beads on the rat brain cells, the mechanical properties of these cells can be probed by measuring the beads' displacements during a known applied magnetic force. The creep compliance can be described by the Eq. 2.12 and Eq. 2.14. For simplicity, all elastic modulus calculations in this part were based on the same geometry factor, which was adopted as $\pi \times R_{\text{bead}}$. The mean value and the standard deviation of viscoelasticity parameter β were deduced at a linear scale according to Eq. 4.4. The calculations of mean value and standard deviation of elastic modulus (stiffness) $1/J_0$ were taken at a logarithmic scale, as in Eq. 4.5. In order to determine the significance of data, one way ANOVA (Analysis of Variance) test was carried out for the data with multi groups (≥ 3). Student's t test was adopted for the data with only two groups. Values of $p < 0.05$ were considered statistically significant. N.S. indicates no statistical significance.

$$\text{mean}(\beta) = \bar{\beta} = \frac{1}{n} \sum_{i=1}^n \beta_i, \quad SE(\beta) = sd(\beta) = \left(\frac{1}{n-1} \sum_{i=1}^n (\beta_i - \bar{\beta})^2 \right)^{\frac{1}{2}} \quad (4.4)$$

$$\text{mean}(1/J_0) = 10^{\overline{\log_{10}(1/J_0)}}, \quad SE(1/J_0) = \frac{sd(\log_{10}(1/J_0))}{\log_{10}(1/J_0)} 10^{\overline{\log_{10}(1/J_0)}} \quad (4.5)$$

An experimental sample of living rat neurons is visualized in Fig. 4.26 (a). For neuronal cell experiments, the beads were categorized according to the morphological sites they were bound to. Bead clusters and beads bound on the edge of a cell soma were ignored. A SEM experiment showed good binding between bead and neurite, as shown in the inset image in Fig. 4.26 (a). The response of a neurite-bound bead is shown in Fig. 4.26 (b). In experiment, 3 cycles with 40% duty cycle of force and a period of 9 s were applied. For beads on neurites, a small force of around 200 pN was applied. In data analysis, only the beads with good repeatability in each response and with a maximal displacement of less than 2 μm were considered. This eliminates poorly bound beads that are ripped off the cell or slip during the experiment. In practice, like in the HL-1 cell experiment (section 4.4.1),

usually the second spike was adopted to fit to Eq. 2.14 to deduce the parameters $1/J_0$ and β . Although only two parameters were adopted, the experimental response of beads can be described with this formula very well, as seen in the inset of Fig. 4.26 (b).

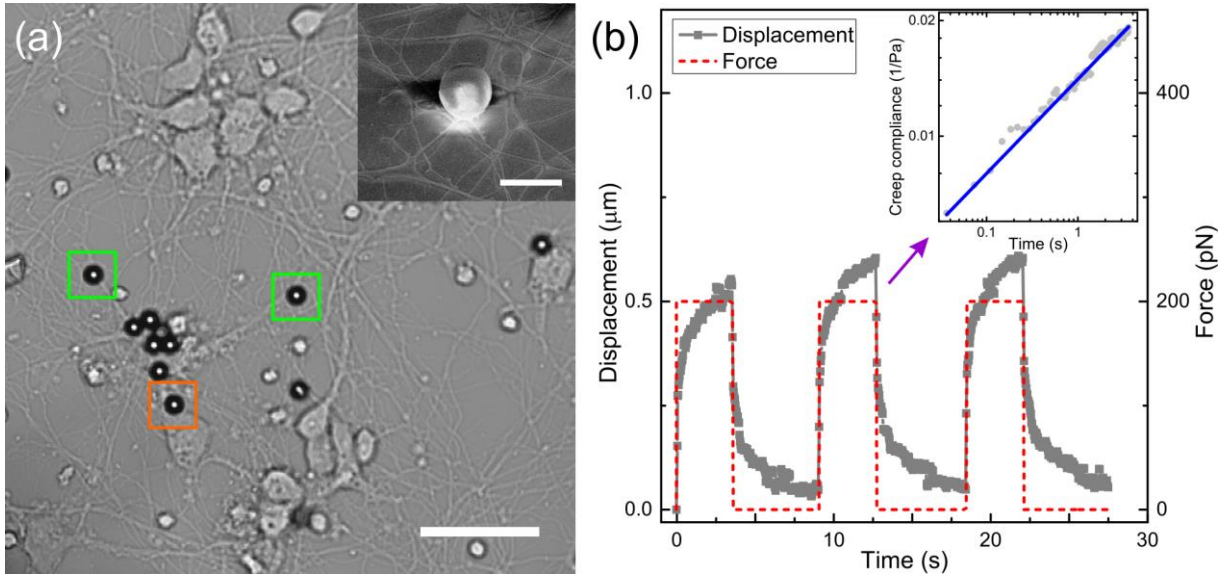


Fig. 4.26. (a) Microscope image of neurons (DIV4) and magnetic beads in workspace. The beads in the green boxes were bound on neurites. The bead in the orange box was bound on the neuron soma. Scale bar is 60 μm. The inset is a SEM image of a bead bound on neurites, scale bar 5 μm. (b) A bead response under an applied force sequence. The inset shows the creep compliance of the second spike and its fit to the power-law (both axes are scaled logarithmically). (Adopted from Ref. [105].)

The displacements of neurite bound beads at DIV7 and DIV15 are shown in Fig. 4.27 (a). The deviations are presented by the shadowed areas, which were calculated according to Eq. 4.4 and Eq. 4.5. It is obvious that the displacement amplitude of DIV7 is larger than DIV15, hence also the compliance. As shown in Fig. 4.27 (b), the neurites' stiffness at DIV15 obviously obeys a log-normal distribution, and spans around two orders in magnitude. The geometrical mean elastic modulus of the neurites at DIV15 is 82.6 Pa. The distribution probability can be fit by a Gaussian function in the logarithmic scale (median value 74.8 Pa). As seen in Fig. 4.27 (c), the parameter β ranges from 0.09 to 0.35, in which it has an arithmetic mean value of 0.207 (median value of fitting 0.201). The stiffness $1/J_0$ and viscoelasticity β of neurites at different times are presented in Fig. 4.27 (d). At the early culture time as DIV4, it is very impressive that both the elastic modulus and viscoelasticity parameter of the neurite exhibited the highest values. This high stiffness can be ascribed to the high growth tension inside early neurites, which was proposed as the main limitation of axonal lengthening [135]. The high value of β showed that the neurite is more viscous-like and has a high agitation level in the initial elongation stage. After 4 days, the elastic modulus of neurite decreases after the fast extension period. As displayed in the Fig. 4.28 (c) - (h), the neurite network developed between DIV4 and DIV10. With the maturation of neurite network, the stiffness of the neurites increased. Unlike the stiffness, the viscoelasticity parameter β always decreases with the culture time, which means the neurites become more stable with growth. Microtubulin and especially the neurofilament were found to be the main contributions to the mechanical properties of neurite [136]. As presented in Fig. 4.28 (g)

- (h), there was an obvious enhanced expression of neurofilament at DIV10 in neurites. In the late culture time, all mechanical parameters tend to stabilize, and exhibit smaller distributions (standard error).

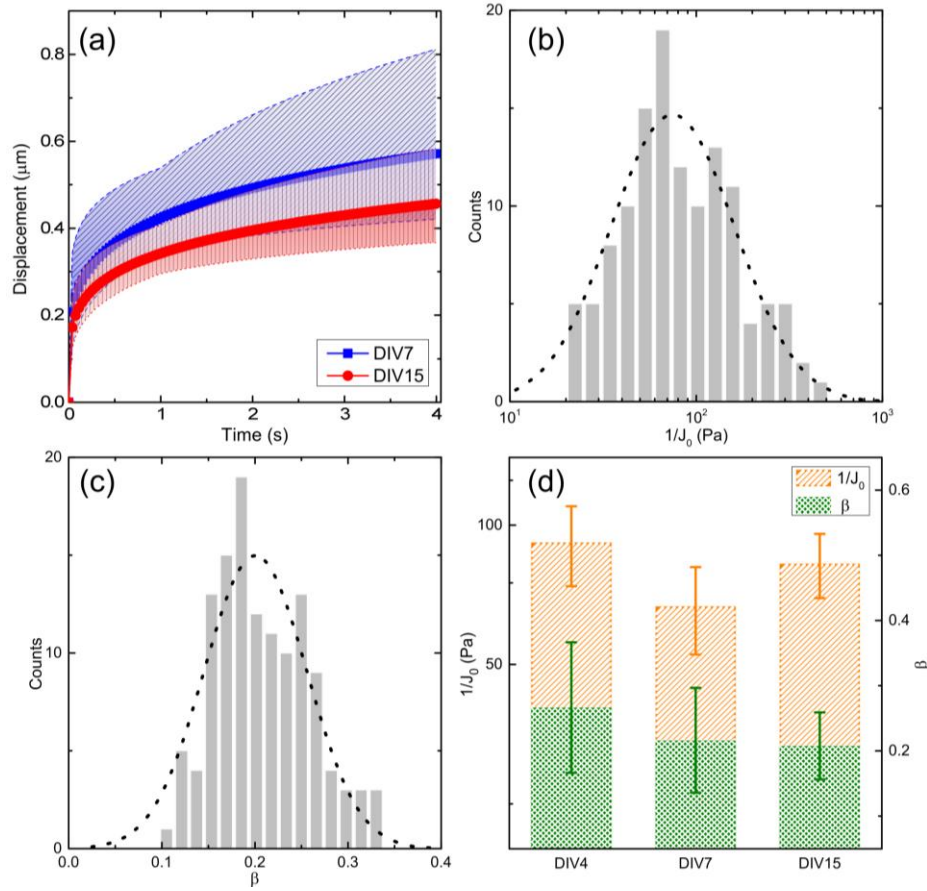


Fig. 4.27. (a) Creep response of neurites at DIV7 and DIV15. (b) The distribution of measured neurites' stiffness at DIV15, the short dash is a Gaussian function fitting of the histogram. (c) The distribution of measured neurites' β at DIV15, the short dash is a Gaussian function fitting of the histogram. (d) Elastic modulus ($p < 0.039$) and β ($p < 3.8 \times 10^{-6}$) of neurites at DIV4 ($N=58$), DIV7 ($N=102$), and DIV15 ($N=124$). (Adapted from Ref. [105].)

The mechanical properties of neuron soma are shown in Fig. 4.29 (a). Here, the applied force was set to around 640 pN. Unlike the neurites, the elastic modulus of the soma always increases with time in culture. This suggests the tension generated during early outgrowth is not dominated in the soma. The β of the neuronal soma also decreased with time. As shown in the Fig. 4.28 (a) - (b), the most volume of the neuronal soma is occupied by the nucleus. It was found that the elasticity of the neuron soma mainly depends on its nucleus [136]. In addition, as for brain tissue, the mechanical response usually shows nonlinearity which depends on the magnitude of the applied stress [137, 138]. As shown in Fig. 4.29 (b), the stiffness of neuronal soma increase with external stress, and the value of β does not show a significant change. These findings agree well with the results in Ref. [136].

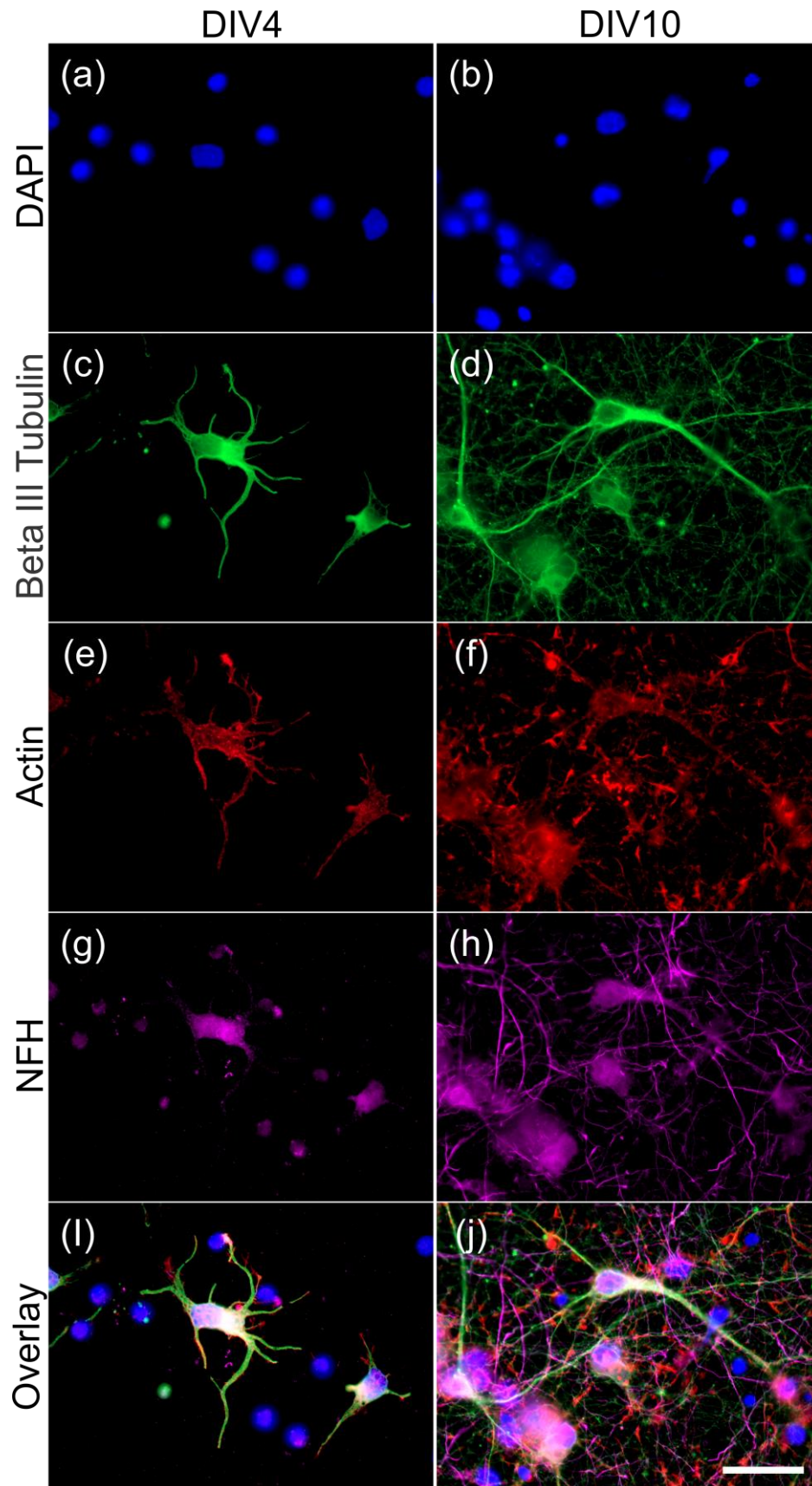


Fig. 4.28. (a) - (b) Nucleus staining. (c) - (d) Microtubulin staining. (e) - (f) F-Actin staining. (g) - (h) Neurofilament staining. (i) - (j) Overlay. Scale bar 30 μm . (Adopted from Ref. [105].)

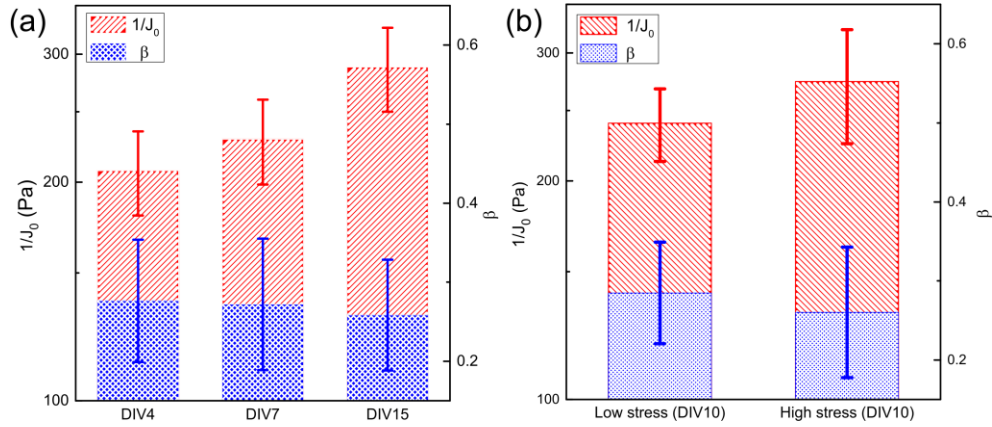


Fig. 4.29. (a) Elastic modulus ($p < 0.005$) and β ($p < 0.04$ for DIV4 and DIV15) of neuronal somas at DIV4 (N=90), DIV7 (N=92), and DIV15 (N=114). (b) Elastic modulus ($p < 0.01$) and β (N.S.) of neuronal somas at DIV10 under different stress. The low and high stress correspond to applied forces of 200 pN (N= 87) and 640 pN (N=102), respectively. (Adapted from Ref. [105].)

In order to determine the amount of glia in the mixed cell cultures, immunostainings of nucleus and MAP2 was performed at DIV6, as Fig. 4.30 (a) - (c). According to the procedure of cell dissociation (section 3.2.2), the glia in these samples accounted to about 64.3% on average. It is well known that the glia acts as the scaffold for the neuronal cell growth. The neuron tends to grow on top of glia. Compared to the neurons, glial cells here usually present a flat appearance in vitro (Fig. 4.30 (d), reflected light). Hence, it is possible to use morphological features such as round shape and extended neurite to designate the neurons in these mixed cultures using non-fluorescent images. By this method, an assignment accuracy of 76% can be obtained within these phase contrast images. In practice, these two types of cells can be distinguished more easily under transmitted light with a good focusing, as seen in Fig. 4.30 (e).

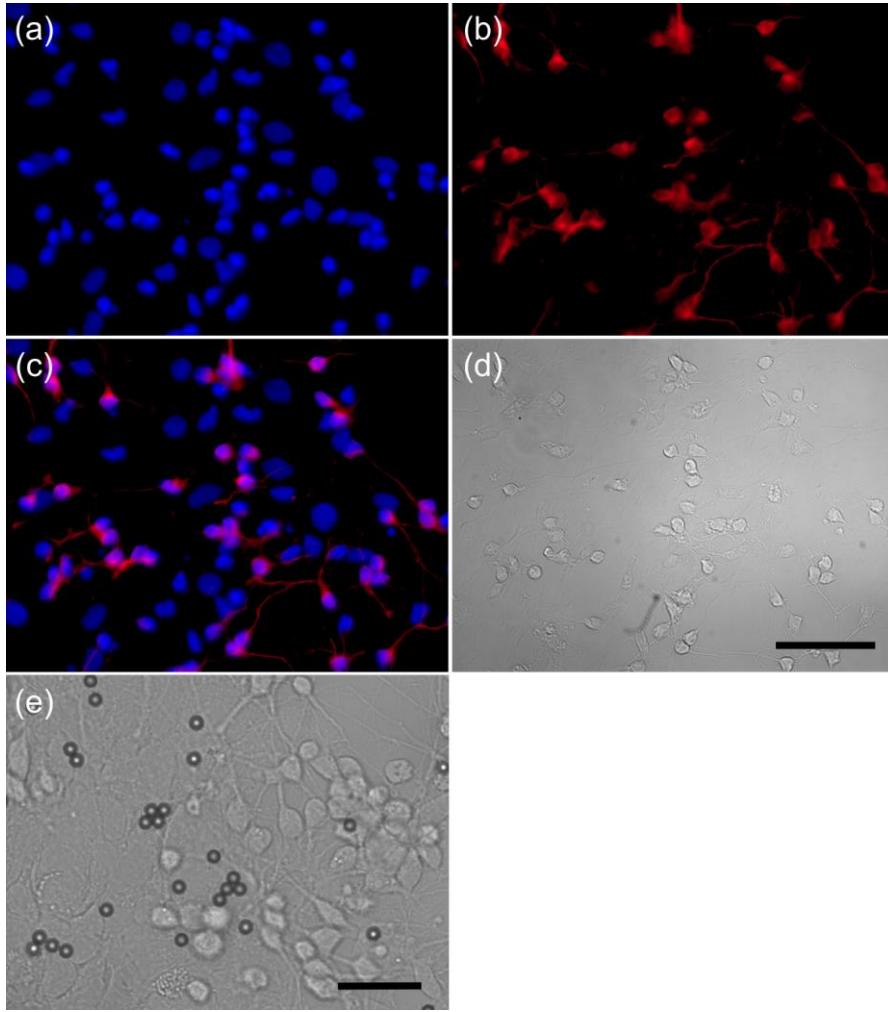


Fig. 4.30. (a) Nucleus stained with DAPI. (b) MAP2 staining. (c) Merged image (d) Phase contrast image. (a) - (d) share the same scale bar representing 50 μm . (f) A microscope image (bright field) taken during experiment, scale bar 25 μm . (Adopted from Ref. [105].)

As shown in Fig. 4.31 (a), the elastic moduli of glia sharply increase with culture time. It was reported that the increase in the stiffness of glial cells depend on the increased intermediate filaments, such as GFAP and Vimentin [139]. In that study, the stiffness increase was correlated with the reactive gliosis. As shown in Fig. 4.32 (c), the glial filaments at an early stage, such as DIV4, were only visible as blurry dots and scattered close to the nucleus. But highly organized and dense glial filament structures can be found at DIV7 (Fig. 4.32 (d)). It should be noted that even in the DIV7 samples, there were still some cells observed with blurry and non-structured GFAP, which were considered as near or undergoing mitosis phase (see the inset figure of Fig. 4.31 (b)). Unlike the finding in the report [140], which shows that the glial cells in central nervous system (CNS) are softer than the surrounding neuronal tissue. Here the stiffness of glia is higher than that of neuron, which can be mainly ascribed to its reactive gliosis or foreign body reaction. Besides the cytoskeleton adaption in the reactive gliosis, the flat morphology of glia cultured on glass here is very different from the cell phenotype when cultured on substrate with similar stiffness as brain tissue's [141, 142]. The detailed influence from substrate stiffness will be discussed later. Because of the smaller cell height, a larger strain resulted in the measurement even with the same displacement of bead. Due to the nonlinear mechanics, high strain will give rise to higher stiffness. As seen in Fig. 4.31 (a), the β value of glia

remains very stable, which can be explained by the continuous proliferation. Furthermore, the β values of glia were also higher (more viscous-like) than that of neurons. The histograms of glia' elastic moduli at DIV10 and DIV15 were depicted in Fig. 4.31 (b). The mean elastic moduli of glia at DIV10 and DIV15 did not show too much difference. This agrees well with the finding that the half-life of rat astrocytes cultured in serum supplemented medium is approximately 7.5 days [143]. Hence, the statistical mechanical measurements proved to be a sensitive method to inspect the microstructural properties of cells.

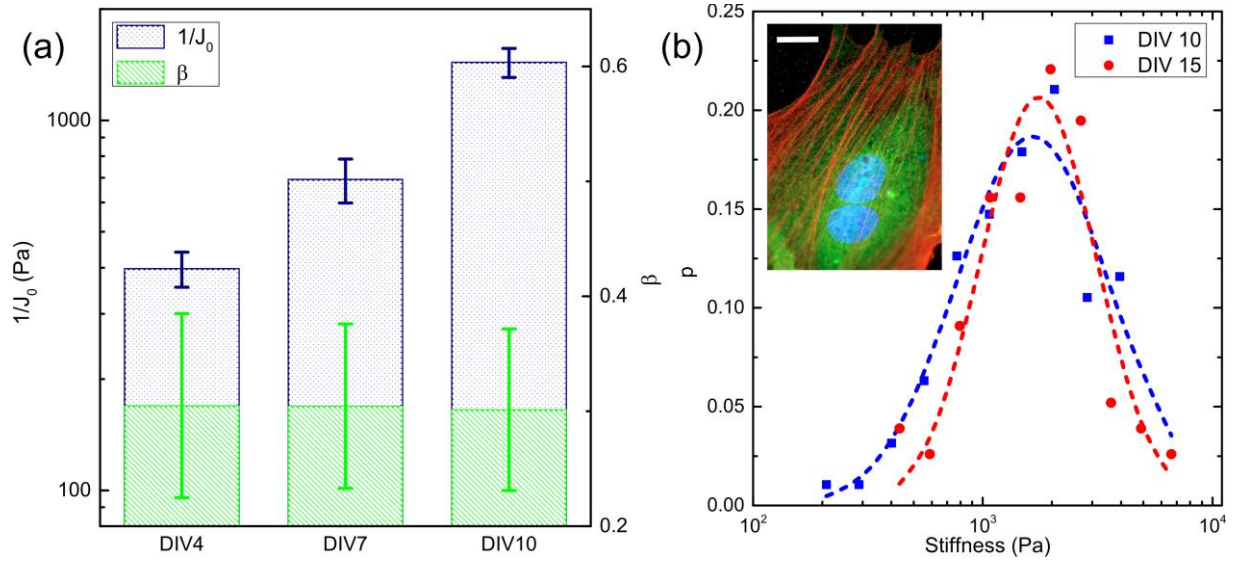


Fig. 4.31. Stiffness ($p < 6.1 \times 10^{-22}$) and β (N.S.) of glial cells in DIV4 (N=68), DIV7 (N=80) and DIV10 (N=95). (b) The histogram of the elastic modulus ($p < 0.04$) of glia at DIV10 and DIV15 (N=77). The inset show a glia close to the end of mitosis, the blue color refers to the cell nucleus. The scale bar is 20 μm . (Adapted from Ref. [105].)

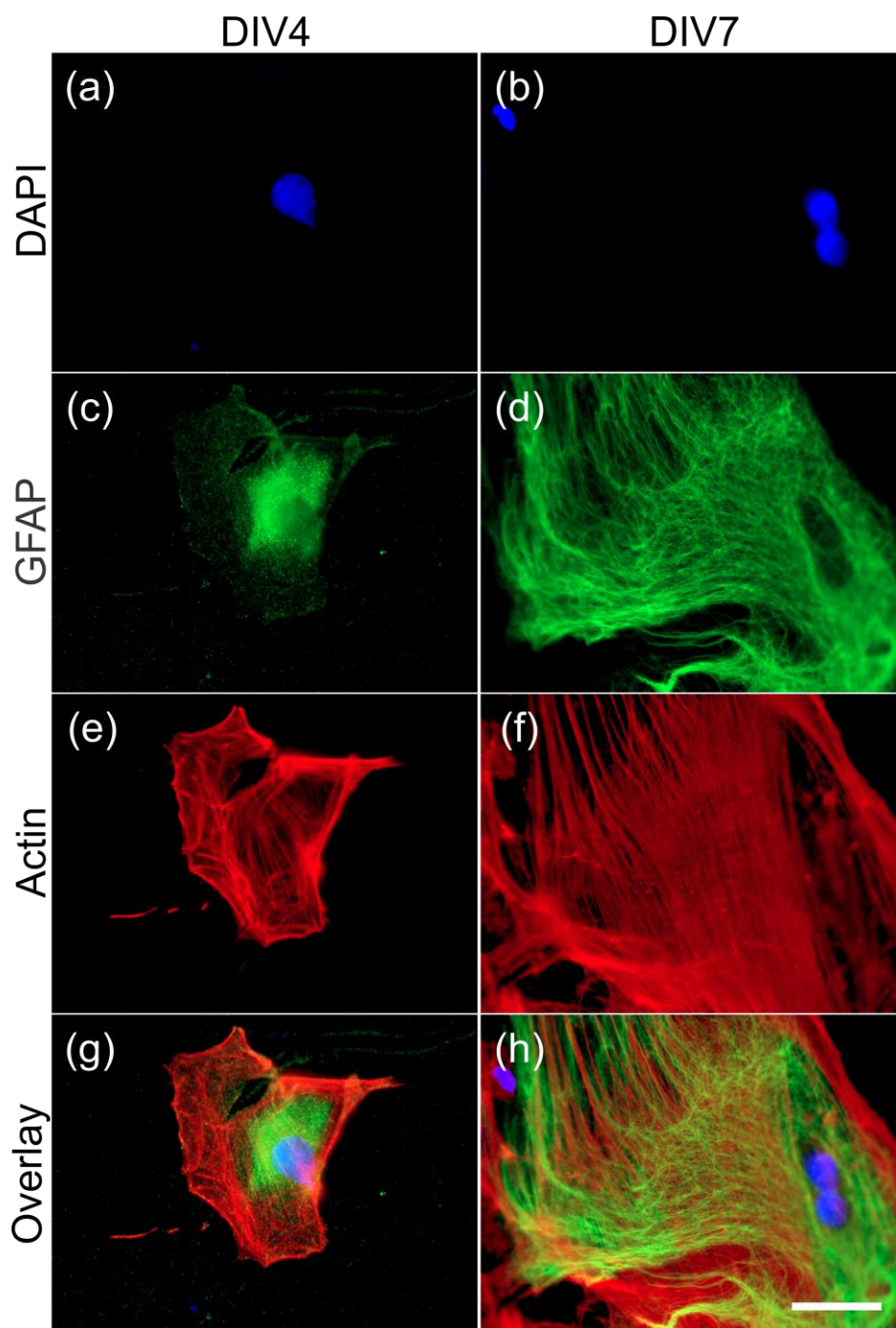


Fig. 4.32. (a) - (b) Nucleus staining. (c) - (d) Glial fibrillary staining. (e) - (f) F-Actin staining. (g) - (h) Overlay. Scale bar 30 μm . (Adopted from Ref. [105].)

It was argued that the difference in mechanosensitivity between glial cells and cortical neurons could play an essential role in the initial structuring of the nervous system [144]. In this work, both the mechanical properties of neuron and glia cultured on PDMS substrates with elastic moduli ranging from a few kPa (PDMS60:1) to MPa (PDMS10:1) were characterized. As shown in Fig. 4.33 (a), the stiffness of neurites decreases with decreasing rigidity of the substrates. This behavior that the neurites adapt their mechanical properties to the compliance of substrates has also been observed by other studies [136, 145]. As shown in Fig. A.7, the actin of neuronal cells on compliant substrates is

slightly more diffuse, while tubulin structures are not noticeably altered. However, the β values of the neurite are very stable.

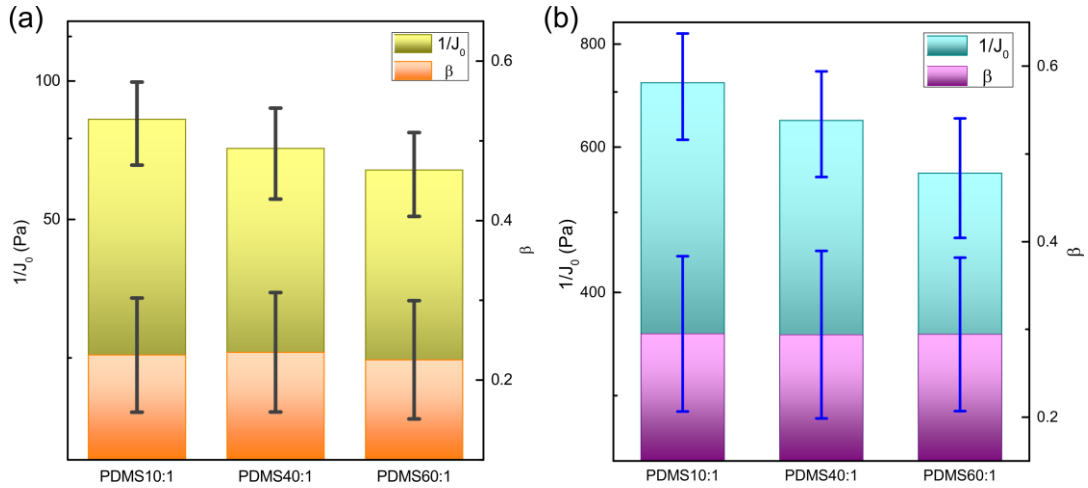


Fig. 4.33. (a) Stiffness ($p < 0.009$ for PDMS10:1 and PDMS60:1) and β (N.S.) of neurites at DIV10 cultured on PDMS10:1 (N= 157), PDMS40:1 (N= 145), and PDMS60:1 (N= 173) substrates. (b) Stiffness ($p < 0.03$ for PDMS10:1 and PDMS60:1) and β (N.S.) of glia at DIV7 cultured on PDMS10:1 (N= 104), PDMS40:1 (N= 123), and PDMS60:1 (N= 133) substrates. (Adopted from Ref. [105].)

Like in the case of neurons, the glia also showed a lower stiffness when cultured on the soft substrates, as seen in Fig. 4.33 (b). It was reported that the expression of GFAP decreases when glia is cultured on a soft substrate [141, 146]. As shown in Fig. 4.34 (c) and (d), the GFAP mesh of glia on soft substrates exhibits some blurred structures and lower density. The cell on the stiff substrate (PDMS10:1) showed clearer filament organization, which is similar to that on glass (Fig. 4.32 (d)). In addition, the actin fibers in glial cell on a compliant substrate showed less organization and some pores, which is similar to the observation in fibroblast [147]. It is well known that glia is a mechanical mediator in the brain. When injury or foreign body response occurs, they stiffen to bridge the mismatch between neurons and the hard object (modeled by the PDMS or glass coverslip). Like in the neurite, the viscoelasticity of glia did not present a dependence on the substrate stiffness.

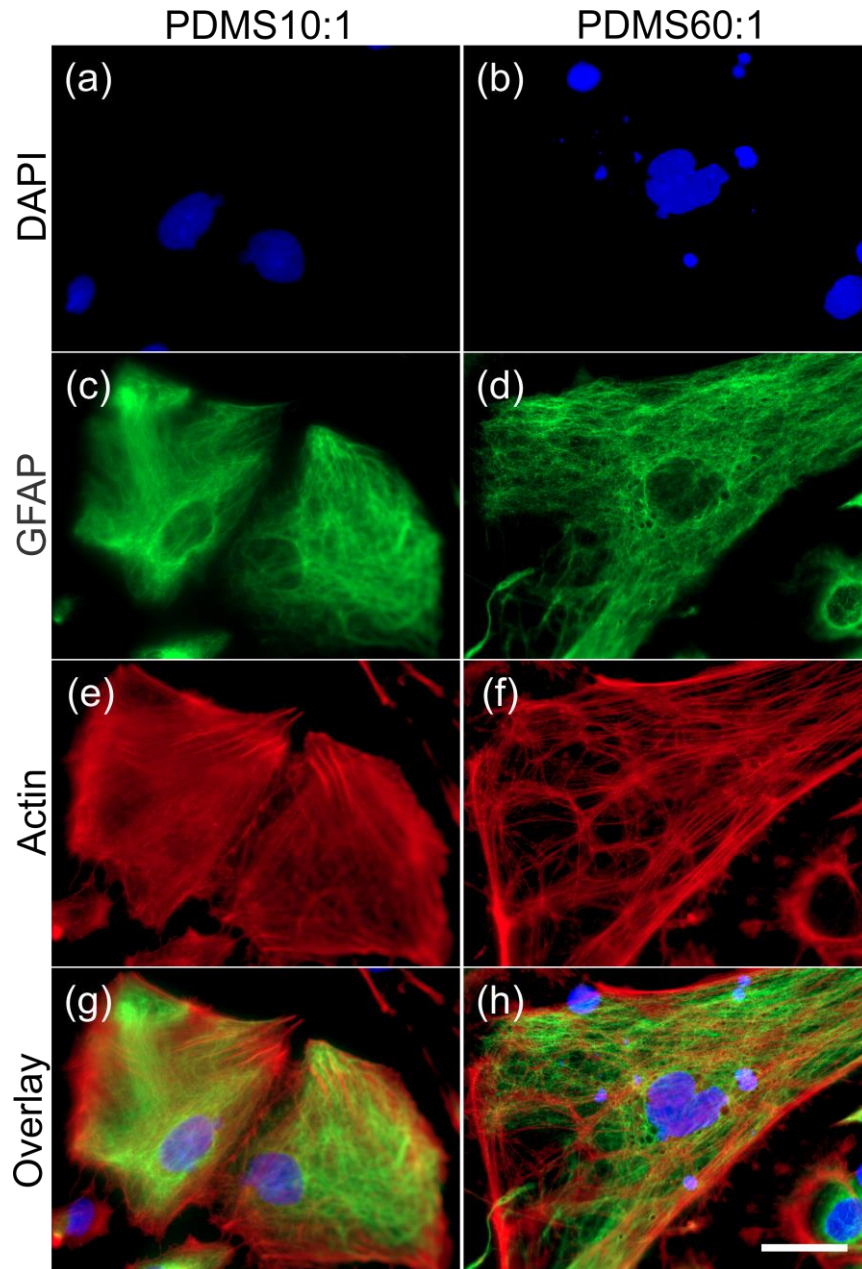


Fig. 4.34. (a) - (b) Nucleus staining, (c) - (d) Glial fibrillary staining, (e) - (f) F-Actin staining. (g) - (h) Overlay. Scale bar 30 μm . (Adopted from Ref. [105].)

4.4.4 Summary on the Mechanics Characterization of Cardiomyocyte and Brain Cells

HL-1 cells' mechanical properties were characterized with the developed magnetic tweezers. Compared to common single-pole MTs, the tri-pole MT with a large workspace allows to characterize many cells at a time. Thanks to the good maneuverability of the multi-pole MT, a living cell can be probed in different directions to investigate the cell heterogeneity without additional sample handling. The results show that HL-1 cells have a log-normal distribution in their elastic modulus. The cell structure becomes stiffer with increasing confluence, i.e. when the cells begin to mature due to feedback from contact with neighboring cells. In addition, the mechanical properties of these cells exhibit strong heterogeneity.

With the MTC setup, the complex elastic moduli of HL-1 cardiomyocytes were measured. In agreement with the findings by the MT, this type of cell shows high anisotropy and a log-normal distribution in stiffness. Furthermore, their complex elastic modulus follows the soft glassy rheology model. The stiffness of the substrate has an effect on the cell mechanical properties. For example, stiffening phenomenon at low frequency was observed on stiff substrates, which depends on the prestress generated by myosin activity.

The statistical mechanical measurements of living rat brain cells were performed by the magnetic tweezers with a larger workspace ($120 \times 120 \mu\text{m}^2$ compared to $60 \times 60 \mu\text{m}^2$ adopted in the HL-1 experiment). With maturing of cells, both the neurons and glia become stiffer. However, there is a high tension observed in the neurites of neuron at DIV4. The power-law exponent of neuronal cells decreases with culture time, but the β value of glia does not change during culture. For substrates with elastic modulus above few kPa, the stiffness of both neuron and glia increase with the substrate stiffness. The glial cell cultured on rigid substrates presents a reactive gliosis phenotype.

5. Conclusion

In the previous chapters, the implementation and application of both magnetic tweezers and magnetic twisting cytometry were presented. High throughput, high force or torque output, and good maneuverability have been achieved. Compared to magnetic tweezers, magnetic twisting cytometry showed higher throughput due to its large workspace, which is in practice only limited by the microscope and camera. The multi-cell measurement techniques allow high efficiency and to reduce the effect of variation from sample to sample. In the practical application, the multi-pole magnetic tweezers exhibited high flexibility to handle both stiff cells like cardiomyocytes and soft fragile cells like primary neuronal cells.

In the experiments, it was found that the mechanical properties of cells change during growth, maturation, and cell contacting. Besides this, the cell mechanical properties are also sensitive to the rigidity of the substrates. All types of cells show a log-normal distribution of stiffness, regardless of the probe location (inside the cell or bound on the surface of cell) and of the measurement protocol (creep response or oscillatory response). Both HL-1 and neuronal cells exhibited high heterogeneity in mechanical properties. Thanks to the good maneuverability in the multi-pole MT and MTC, a living cell can be probed in different directions without additional sample handling. The creep response of a cell can be fit to the linear viscoelasticity model (in case of HL-1 cell) or power-law rheology (for brain cell) very well. The complex elastic moduli of HL-1 cells follow the soft glassy rheology.

In the various magnetic tweezers, tri-pole magnetic tweezers exhibit several advantages such as high force and good maneuverability due to homogeneous force. The maximum magnetic field or force is dependent on both the geometry and material of the magnetic tips. For example, the optimized width of tip should have the same dimension as the radius of the workspace, and the thickness of tip also should not be too small as compared to the distance among the tips. In order to achieve feedback control, an inverse force model which can handle the nonlinear magnetization of magnetic beads was implemented. In MT, the magnetic tips can be configured conveniently for different requirements, such as high force ($60 \times 60 \mu\text{m}^2$ for cardiomyocytes), or high throughput ($120 \times 120 \mu\text{m}^2$ for brain cells). In this work, a hexapole was chosen for the main yoke structure, which exhibited high flexibility in practice. This structure is compatible to both tri-pole and hex-pole MT. Furthermore, 2D MTC functionality was extended on the hexapole electromagnet, in which better maneuverability and higher field can be more easily achieved as compared to common MTC [31]. Some examples of magnetic tweezers presented in literature are compared with the setup implemented in this work, see Table 5.1.

Table 5.1 Comparison of magnetic tweezers

Magnetic Tweezers	Force ^{a)}	Throughput	Maneuverability
Single-pole [56]	~ 2 nN	Single cell	Single direction force
Tri-pole [64]	~ 1 nN	Single cell	2D non-feedback control
Hex-pole [63]	few pN	— ^{b)}	Pseudo-3D feedback control
Quad/Hex-pole [60, 62]	few pN	—	2D/3D feedback control
This work: Tri-pole	~ 1 nN ^{c)}	Multi cells	2D feedback control

^{a)} The forces are estimated with the moment of Dynabead M270. The force of single-pole MT is given at a distance of 20 μm away from the magnetic pole. For multi-pole MT, all the forces are measured at the center of workspace. ^{b)} Because of small force, these apparatuses were mainly aimed for molecular biophysics studies. ^{c)} Here it refers to the MT with a workspace of $60 \times 60 \mu\text{m}^2$.

In order to obtain high force, a FeCo alloy was adopted as magnetic tips material because it has the highest saturation magnetization (2.35 T) of all known commercial magnetic materials. During the manufacturing of the magnetic parts, some segregation and formation of morphological roughness occurred near the laser cutting edge. This deteriorated the magnetic performance of the outer layer of the tips, which affected the accuracy and range of force and induced a non-vanishing force at zero coil current. The force errors caused by the irregular shapes of tips are usually local. Hence, the high force (small workspace) MT is more sensitive to the quality of tips than the low force one. In addition, the FeCo magnetic tips were found to be corrosive in HL-1 and neuron cell medium. The release of metal ions could cause cytotoxicity. The quality of electrodeposition for passivation purpose was also deteriorated near the cutting edge of tips. However, conformal coating with parylene C showed excellent isolation and good durability. Therefore, for any practical magnetic tweezers, a trade-off among high force, maneuverability, throughput, and manufacturing issues must be taken into account.

In order to obtain high performance, electronics and software were customized and optimized for different applications. For example, several multi-particle tracking algorithms have been implemented for high speed (center of mass) or high robust (2D cross-correlation) stringent situations. With the help of the adopted theoretical model of the amplifier, the performance for different coil configurations can be easily optimized. Due to the high magnetic performance of the yoke and the mechanical structure of the yoke holder, a high magnetic field can be achieved without worrying about the temperature rise in the fluidic reservoir. LabVIEW software and Matlab programs were developed for MT/MTC control and for data analysis. Some parameters of the setup are listed and compared with the results from other groups reported in literatures, see Table 5.2.

Table 5.2 Performance of electronics and software

Performance	This work	Other work	Comment
Coil current (Max / Min)	4 A / 150 μ A	3 A [56]	
Bandwidth (set time) of amplifier	22.4 kHz (< 50 μ s) ^{a)}	< 100 μ s [56]	Depends on the inductance of coil
Speed of feedback control loop	Up to 1 kHz	200 Hz [60]	Depends on delays of control I/O, camera, and particle tracking
Particle tracking accuracy ^{b)}	< 3 nm	~ 2 nm [108]	In real-time control, besides the accuracy, the speed is also very critical
Temperature rise ^{c)}	Negligible		For most single-pole MT, water cooling is necessary

^{a)} Tested with 80 turns coil. ^{b)} The accuracy is estimated for a 63 \times objective and cross-correlation based algorithm. ^{c)} Refers to the temperature rise in the cell medium caused by coil heating under the highest force or magnetic field used.

6. Outlook

In this work, the magnetic tweezers have been applied to cell mechanics characterization. It should be noted that the various advantages of this setup could also make it suitable for other potential applications such as single-molecular mechanics and soft matter rheology studies. For instance, Gosse *et al.* and Chiou *et al.* had demonstrated 6-pole electromagnetic tweezers can be used to stretch and twist single DNA molecules [63, 148]. Besides cutting the sharp tips from foil, the electrodeposition method has also been widely adopted [29, 148]. Although there is a thickness limitation, which affects the saturation force, the shape of tips can be defined very well in electrodeposition. With identical tips, both the accuracy of force and the maneuverability can be improved. Nevertheless, for high force and high throughput (large workspace) application, magnetic tips with appropriate thickness are indispensable. As demonstrated by the manufacturer (SEKELS GmbH, Germany), the morphology of magnetic tip can be improved with a new laser cutting machine.

In magnetic twisting cytometry, because of high field and economical advantage, an electromagnet was adopted for ferromagnetic particle polarization. However, it is not convenient to magnetize a single sample repeatedly because of the spatial transfer between the polarization and the twisting apparatuses. Furthermore, there is magnetic relaxation in ferromagnetic particle after polarization, namely the magnetic moment decreases with time [80, 130]. In principle, it is possible to embed a small magnetizing coil underneath the fluidic reservoir and perform on-site magnetization using a surge generator. By using such an on-site magnetizing coil, the magnetic moment of particles can be controlled better. On the other hand, in contrast to the Dynabeads® particle, the ferromagnetic bead used in this work has a large distribution in size, and its asymmetric (irregular) pattern under microscope tends to deteriorate the tracking accuracy during movement. Therefore, it will be beneficial to adopt another type of ferromagnetic bead which owns better shape and higher magnetization.

The mechanical properties of cells are assumed to be generated by cytoskeletal components (microtubules and actin filaments etc.), cytoplasm and cell nucleus, and influenced by the substrate and coupling between cells and the extracellular matrix. Usually, the cell mechanics can be tuned by genetic manipulation, drug treatment, by substrate extracellular matrix or by topographic pattern, substrate stiffness, and so on. Genetic manipulation, such as gene knockout, is one of the most powerful tools to investigate the role of specific genes (or its related proteins) for the mechanical properties of cells. Detailed knowledge of the knockout gene is essential for understanding how the cell functions, both in the normal and in the pathological states. In addition, as the blebbistatin used for myosin II inhibition in this work, drugs which selectively disrupt the specific parts of cell cytoskeleton can be added to distinguish the contributions of different parts in the cytoskeleton to the cell mechanical properties. It is well known that various cell functions and properties in growth are also regulated by the extracellular matrix (ECM) and by topographic cues. For example, the axon

growth of neurons can be guided by micropatterned ECM cue [149]. In this work, both cardiomyocyte and brain cells have shown some difference in their mechanical properties when cultured on soft PDMS substrates. However, substrates with stiffness below than 1 kPa are very hard to obtain using PDMS. Polyacrymide (PA) gels, which own better mechanical tunability, could be a promising material for very soft substrates [150].

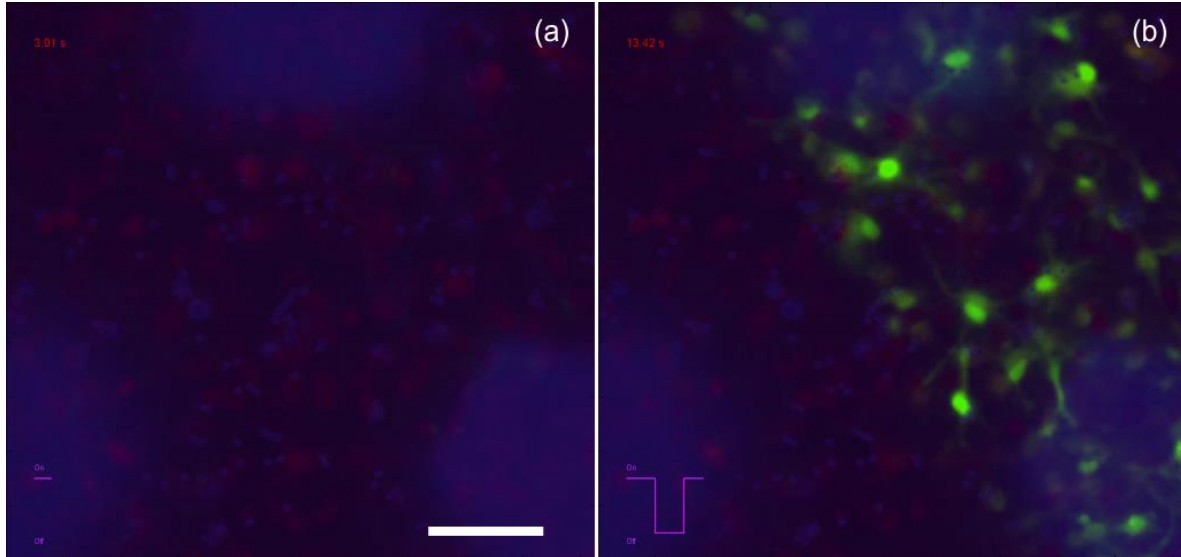


Fig. 6.1. (a) Initial stage of stretch, the blue and red refer the bright image (reduced in intensity) and fluorescence background respectively. (b) The green refers the Ca^{2+} fluorescence. The scale bar is 60 μm .

Actually, besides the cell mechanics measurement, it is also very interesting to study the non mechanical response of cells under mechanical stimuli. For instance, Kilinc *et al.* have demonstrated that the elongation and growth direction of neuronal axon can be manipulated by external force via magnetic tweezers [151]. It is well known that there are numerous mechanically sensitive ion channels in nerve cells. For example, a preliminary result of Ca^{2+} flux in neurons due to the stretching of magnetic beads is shown in Fig. 6.1. The applied force was 1 nN. Each on-off period of force was composed of 5 s on and 5 s off. In addition, electrogenic cells can also be probed by the patch clamp (a device broadly used in electrophysiology study) under stress stimulus with MTC or MT.

References

1. Mofrad, M.R.K. and e. Roger D. Kamm, *Cytoskeletal Mechanics*. 2006: Cambridge University Press.
2. Discher, D.E., P. Janmey, and Y.L. Wang, *Tissue cells feel and respond to the stiffness of their substrate*. Science, 2005. **310**(5751): p. 1139-1143.
3. Bao, G. and S. Suresh, *Cell and molecular mechanics of biological materials*. Nature Materials, 2003. **2**(11): p. 715-725.
4. Janmey, P.A. and C.A. McCulloch, *Cell mechanics: Integrating cell responses to mechanical stimuli*. Annual Review of Biomedical Engineering, 2007. **9**: p. 1-34.
5. Phillips, C.A. and J.S. Petrofsky, *Mechanics of skeletal and cardiac muscle*. Thomas, 1983.
6. McCain, M.L. and K.K. Parker, *Mechanotransduction: the role of mechanical stress, myocyte shape, and cytoskeletal architecture on cardiac function*. Pflugers Archiv-European Journal of Physiology, 2011. **462**(1): p. 89-104.
7. Levin, H.R., et al., *Reversal of Chronic Ventricular Dilation in Patients with End-Stage Cardiomyopathy by Prolonged Mechanical Unloading*. Circulation, 1995. **91**(11): p. 2717-2720.
8. Knoll, R., et al., *The cardiac mechanical stretch sensor machinery involves a Z disc complex that is defective in a subset of human dilated cardiomyopathy*. Cell, 2002. **111**(7): p. 943-955.
9. Swift, J., et al., *Nuclear lamin-A scales with tissue stiffness and enhances matrix-directed differentiation*. Molecular Biology of the Cell, 2013. **341**: 1240104.
10. Majkut, S., et al., *Heart-Specific Stiffening in Early Embryos Parallels Matrix and Myosin Expression to Optimize Beating*. Current Biology, 2013. **23**(23): p. 2434-2439.
11. Wen, S., H. Li, and J. Liu, *Dynamic signaling for neural stem cell fate determination*. Cell Adhesion & Migration, 2009. **3**(1): p. 107-117.
12. Raper, J. and C. Mason, *Cellular Strategies of Axonal Pathfinding*. Cold Spring Harbor Perspectives in Biology, 2010. **2**(9): a001933.
13. Moore, S.W. and M.P. Sheetz, *Biophysics of Substrate Interaction: Influence on Neural Motility, Differentiation, and Repair*. Developmental Neurobiology, 2011. **71**(11): p. 1090-1101.
14. Franze, K., *The mechanical control of nervous system development*. Development, 2013. **140**(15): p. 3069-3077.
15. Gomez, T.M. and P.C. Letourneau, *Actin dynamics in growth cone motility and navigation*. Journal of Neurochemistry, 2014. **129**(2): p. 221-234.
16. Hilgetag, C.C. and H. Barbas, *Developmental mechanics of the primate cerebral cortex*. Anatomy and Embryology, 2005. **210**(5-6): p. 411-417.
17. Moeendarbary, E. and A.R. Harris, *Cell mechanics: principles, practices, and prospects*. Wiley Interdisciplinary Reviews-Systems Biology and Medicine, 2014. **6**(5): p. 371-388.
18. Hoffman, B.D. and J.C. Crocker, *Cell Mechanics: Dissecting the Physical Responses of Cells to Force*. Annual Review of Biomedical Engineering, 2009. **11**: p. 259-288.
19. Vinckier, A. and G. Semenza, *Measuring elasticity of biological materials by atomic force microscopy*. Febs Letters, 1998. **430**(1-2): p. 12-16.
20. Rotsch, C. and M. Radmacher, *Drug-induced changes of cytoskeletal structure and mechanics in fibroblasts: An atomic force microscopy study*. Biophysical Journal, 2000. **78**(1): p. 520-535.
21. A-Hassan, E., et al., *Relative microelastic mapping of living cells by atomic force microscopy*. Biophysical Journal, 1998. **74**(3): p. 1564-1578.
22. Dao, M., C.T. Lim, and S. Suresh, *Mechanics of the human red blood cell deformed by optical tweezers*. Journal of the Mechanics and Physics of Solids, 2003. **51**(11-12): p. 2259-2280.
23. Sacconi, L., et al., *Optical micromanipulations inside yeast cells*. Applied Optics, 2005. **44**(11): p. 2001-2007.
24. Zhang, H. and K.K. Liu, *Optical tweezers for single cells*. Journal of the Royal Society Interface, 2008. **5**(24): p. 671-690.
25. Thoumine, O. and A. Ott, *Time scale dependent viscoelastic and contractile regimes in fibroblasts probed by microplate manipulation*. Journal of Cell Science, 1997. **110**: p. 2109-2116.
26. Desprat, N., et al., *Creep function of a single living cell*. Biophysical Journal, 2005. **88**(3): p. 2224-2233.
27. Bausch, A.R., et al., *Local measurements of viscoelastic parameters of adherent cell surfaces by magnetic bead microrheometry*. Biophysical Journal, 1998. **75**(4): p. 2038-2049.

28. Bausch, A.R., W. Moller, and E. Sackmann, *Measurement of local viscoelasticity and forces in living cells by magnetic tweezers*. Biophysical Journal, 1999. **76**(1): p. 573-579.
29. de Vries, A.H.B., et al., *Micro magnetic tweezers for nanomanipulation inside live cells*. Biophysical Journal, 2005. **88**(3): p. 2137-2144.
30. Fabry, B., et al., *Scaling the microrheology of living cells*. Physical Review Letters, 2001. **87**(14): 148102.
31. Fabry, B., et al., *Time scale and other invariants of integrative mechanical behavior in living cells*. Physical Review E, 2003. **68**(4): 041914.
32. Alcaraz, J., et al., *Microrheology of human lung epithelial cells measured by atomic force microscopy*. Biophysical Journal, 2003. **84**(3): p. 2071-2079.
33. Cai, P., et al., *Quantifying Cell-to-Cell Variation in Power-Law Rheology*. Biophysical Journal, 2013. **105**(5): p. 1093-1102.
34. Neuman, K.C. and A. Nagy, *Single-molecule force spectroscopy: optical tweezers, magnetic tweezers and atomic force microscopy*. Nature Methods, 2008. **5**(6): p. 491-505.
35. Yamada, S., D. Wirtz, and S.C. Kuo, *Mechanics of living cells measured by laser tracking microrheology*. Biophysical Journal, 2000. **78**(4): p. 1736-1747.
36. Crocker, J.C. and B.D. Hoffman, *Multiple-particle tracking and two-point microrheology in cells*. Cell Mechanics, 2007. **83**: p. 141-178.
37. Tseng, Y., T.P. Kole, and D. Wirtz, *Micromechanical mapping of live cells by multiple-particle-tracking microrheology*. Biophysical Journal, 2002. **83**(6): p. 3162-3176.
38. Chaudhuri, O., S.H. Parekh, and D.A. Fletcher, *Reversible stress softening of actin networks*. Nature, 2007. **445**(7125): p. 295-298.
39. Bursac, P., et al., *Cytoskeletal remodelling and slow dynamics in the living cell*. Nature Materials, 2005. **4**(7): p. 557-561.
40. Fabry, B., et al., *Signal transduction in smooth muscle - Selected contribution: Time course and heterogeneity of contractile responses in cultured human airway smooth muscle cells*. Journal of Applied Physiology, 2001. **91**(2): p. 986-994.
41. Medalia, O., et al., *Macromolecular architecture in eukaryotic cells visualized by cryoelectron tomography*. Science, 2002. **298**(5596): p. 1209-1213.
42. Maloney, J.M. and K.J.V. Vliet, *On the origin and extent of mechanical variation among cells*. arXiv, 2011. **1104.0702v2**.
43. Puig-de-Morales, M., et al., *Cytoskeletal mechanics in adherent human airway smooth muscle cells: probe specificity and scaling of protein-protein dynamics*. American Journal of Physiology-Cell Physiology, 2004. **287**(3): p. C643-C654.
44. Liu, Y., et al., *Evidence for Localized Cell Heating Induced by Infrared Optical Tweezers*. Biophysical Journal, 1995. **68**(5): p. 2137-2144.
45. Kollmannsberger, P. and B. Fabry, *Linear and Nonlinear Rheology of Living Cells*. Annual Review of Materials Research, 2011. **41**: p. 75-97.
46. Lu, A.H., E.L. Salabas, and F. Schuth, *Magnetic nanoparticles: Synthesis, protection, functionalization, and application*. Angewandte Chemie-International Edition, 2007. **46**(8): p. 1222-1244.
47. Pankhurst, Q.A., et al., *Applications of magnetic nanoparticles in biomedicine*. Journal of Physics D-Applied Physics, 2003. **36**(13): p. R167-R181.
48. Celedon, A., et al., *Magnetic Tweezers Measurement of Single Molecule Torque*. Nano Letters, 2009. **9**(4): p. 1720-1725.
49. Lipfert, J., et al., *Magnetic torque tweezers: measuring torsional stiffness in DNA and RecA-DNA filaments*. Nature Methods, 2010. **7**(12): p. 977-U54.
50. Dobson, J., *Remote control of cellular behaviour with magnetic nanoparticles*. Nature Nanotechnology, 2008. **3**(3): p. 139-143.
51. Lee, J.H., et al., *Magnetic Nanoparticles for Ultrafast Mechanical Control of Inner Ear Hair Cells*. Acs Nano, 2014. **8**(7): p. 6590-6598.
52. Huang, H., et al., *Three-dimensional cellular deformation analysis with a two-photon magnetic manipulator workstation*. Biophysical Journal, 2002. **82**(4): p. 2211-2223.
53. Ramms, L., et al., *Keratins as the main component for the mechanical integrity of keratinocytes*. Proceedings of the National Academy of Sciences of the United States of America, 2013. **110**(46): p. 18513-18518.

54. de Vries, A.H.B., et al., *Direct observation of nanomechanical properties of chromatin in living cells*. Nano Letters, 2007. **7**(5): p. 1424-1427.
55. Kilinc, D. and G.U. Lee, *Advances in magnetic tweezers for single molecule and cell biophysics*. Integrative Biology, 2014. **6**(1): p. 27-34.
56. Kollmannsberger, P. and B. Fabry, *High-force magnetic tweezers with force feedback for biological applications*. Review of Scientific Instruments, 2007. **78**(11): 114301.
57. Kolhatkar, A.G., et al., *Tuning the Magnetic Properties of Nanoparticles*. International Journal of Molecular Sciences, 2013. **14**(8): p. 15977-16009.
58. Landfester, K. and L.P. Ramirez, *Encapsulated magnetite particles for biomedical application*. Journal of Physics-Condensed Matter, 2003. **15**(15): p. S1345-S1361.
59. Hosu, B.G., et al., *Magnetic tweezers for intracellular applications*. Review of Scientific Instruments, 2003. **74**(9): p. 4158-4163.
60. Zhang, Z.P., Y.N. Huang, and C.H. Menq, *Actively Controlled Manipulation of a Magnetic Microbead Using Quadrupole Magnetic Tweezers*. Ieee Transactions on Robotics, 2010. **26**(3): p. 531-541.
61. Fisher, J.K., et al., *Thin-foil magnetic force system for high-numerical-aperture microscopy*. Review of Scientific Instruments, 2006. **77**(2): 023702.
62. Zhang, Z.P. and C.H. Menq, *Design and Modeling of a 3-D Magnetic Actuator for Magnetic Microbead Manipulation*. Ieee-Asme Transactions on Mechatronics, 2011. **16**(3): p. 421-430.
63. Gosse, C. and V. Croquette, *Magnetic tweezers: Micromanipulation and force measurement at the molecular level*. Biophysical Journal, 2002. **82**(6): p. 3314-3329.
64. de Vries, A.H.B., *High force magnetic tweezers for molecular manipulation inside living cells*. Universiteit Twente, 2004.
65. Kurosaki, Y., et al., *Importance of punching and workability in non-oriented electrical steel sheets*. Journal of Magnetism and Magnetic Materials, 2008. **320**(20): p. 2474-2480.
66. Klimczyk, P.K., et al., *Influence of Cutting Techniques on Magnetostriction Under Stress of Grain Oriented Electrical Steel*. Ieee Transactions on Magnetics, 2012. **48**(4): p. 1417-1420.
67. Sundar, R.S. and S.C. Deevi, *Soft magnetic FeCo alloys: alloy development, processing, and properties*. International Materials Reviews, 2005. **50**(3): p. 157-192.
68. Pouponneau, P., et al., *Corrosion Study of Iron-Cobalt Alloys for MRI-Based Propulsion Embedded in Untethered Microdevices Operating in the Vascular Network*. Journal of Biomedical Materials Research Part B-Applied Biomaterials, 2010. **93B**(1): p. 203-211.
69. Hallab, N.J., et al., *Effects of soluble metals on human peri-implant cells*. Journal of Biomedical Materials Research Part A, 2005. **74A**(1): p. 124-140.
70. Yamahata, C., et al., *A PMMA valveless micropump using electromagnetic actuation*. Microfluidics and Nanofluidics, 2005. **1**(3): p. 197-207.
71. Pirmoradi, F., L.N. Cheng, and M. Chiao, *A magnetic poly(dimethylesiloxane) composite membrane incorporated with uniformly dispersed, coated iron oxide nanoparticles*. Journal of Micromechanics and Microengineering, 2010. **20**(1): 015032.
72. Spinks, G.M., et al., *Electroactive conducting polymers for corrosion control - Part 2. Ferrous metals*. Journal of Solid State Electrochemistry, 2002. **6**(2): p. 85-100.
73. Fonner, J.M., et al., *Biocompatibility implications of polypyrrole synthesis techniques*. Biomedical Materials, 2008. **3**(3): 034124.
74. George, P.M., et al., *Fabrication and biocompatibility of polypyrrole implants suitable for neural prosthetics*. Biomaterials, 2005. **26**(17): p. 3511-3519.
75. Gonzalez, M.B. and S.B. Saidman, *Electrodeposition of polypyrrole on 316L stainless steel for corrosion prevention*. Corrosion Science, 2011. **53**(1): p. 276-282.
76. Khan, W., M. Kapoor, and N. Kumar, *Covalent attachment of proteins to functionalized polypyrrole-coated metallic surfaces for improved biocompatibility*. Acta Biomaterialia, 2007. **3**(4): p. 541-549.
77. Loeb, G.E., et al., *Parylene as a Chronically Stable, Reproducible Microelectrode Insulator*. Ieee Transactions on Biomedical Engineering, 1977. **24**(2): p. 121-128.
78. Rodger, D.C., et al., *Flexible parylene-based multielectrode array technology for high-density neural stimulation and recording*. Sensors and Actuators B-Chemical, 2008. **132**(2): p. 449-460.
79. Metallo, C., R.D. White, and B.A. Trimmer, *Flexible parylene-based microelectrode arrays for high resolution EMG recordings in freely moving small animals*. Journal of Neuroscience Methods, 2011. **195**(2): p. 176-184.

80. Valberg, P.A. and J.P. Butler, *Magnetic Particle Motions within Living Cells - Physical Theory and Techniques*. Biophysical Journal, 1987. **52**(4): p. 537-550.
81. Valberg, P.A. and H.A. Feldman, *Magnetic Particle Motions within Living Cells - Measurement of Cytoplasmic Viscosity and Motile Activity*. Biophysical Journal, 1987. **52**(4): p. 551-561.
82. Wang, N., J.P. Butler, and D.E. Ingber, *Mechanotransduction across the Cell-Surface and through the Cytoskeleton*. Science, 1993. **260**(5111): p. 1124-1127.
83. Nayfeh, M.H. and M.K. Brussel, *Electricity and magnetism*. Wiley, 1985.
84. Callister, W.D. and D.G. Rethwisch, *Materials Science and Engineering: An Introduction*. Wiley, 2010.
85. Boyer, T.H., *The Force on a Magnetic Dipole*. American Journal of Physics, 1988. **56**(8): p. 688-692.
86. Bardeen, J., L.N. Cooper, and J.R. Schrieffer, *Theory of Superconductivity*. Physical Review, 1957. **108**(5): p. 1175-1204.
87. Anderson, P.W., *The Theory of Superconductivity in the High-Tc Cuprates*. Princeton University Press, 1997.
88. Paglione, J. and R.L. Greene, *High-temperature superconductivity in iron-based materials*. Nature Physics, 2010. **6**(9): p. 645-658.
89. Krishnan, K.M., *Biomedical Nanomagnetism: A Spin Through Possibilities in Imaging, Diagnostics, and Therapy*. Ieee Transactions on Magnetism, 2010. **46**(7): p. 2523-2558.
90. Jeong, U., et al., *Superparamagnetic colloids: Controlled synthesis and niche applications*. Advanced Materials, 2007. **19**(1): p. 33-60.
91. Bean, C. and J. Livingston, *Superparamagnetism*. Journal of Applied Physics, 1959. **30**(4): p. S120-S129.
92. Franklin, G.F., J.D. Powell, and A. Emami-Naeini, *Feedback control of dynamic systems*. Addison-Wesley, 1994.
93. *COMSOL Multiphysics: Version 3.5a. Modeling guide*. Comsol, 2008.
94. *Finite element method*. https://en.wikipedia.org/wiki/Finite_element_method.
95. Kollmannsberger, P., C.T. Mierke, and B. Fabry, *Nonlinear viscoelasticity of adherent cells is controlled by cytoskeletal tension*. Soft Matter, 2011. **7**(7): p. 3127-3132.
96. Bausch, A.R. and K. Kroy, *A bottom-up approach to cell mechanics*. Nature Physics, 2006. **2**(4): p. 231-238.
97. Mackintosh, F.C., J. Kas, and P.A. Janmey, *Elasticity of Semiflexible Biopolymer Networks*. Physical Review Letters, 1995. **75**(24): p. 4425-4428.
98. Lenormand, G., et al., *Linearity and time-scale invariance of the creep function in living cells*. Journal of the Royal Society Interface, 2004. **1**(1): p. 91-97.
99. Sollich, P., *Rheological constitutive equation for a model of soft glassy materials*. Physical Review E, 1998. **58**(1): p. 738-759.
100. Trepatt, X., et al., *Universal physical responses to stretch in the living cell*. Nature, 2007. **447**(1): p. 592-595.
101. Kollmannsberger, P., *Nonlinear microrheology of living cells*. Friedrich-Alexander-Universität Erlangen-Nürnberg, 2009.
102. Ingber, D.E., *Tensegrity: The architectural basis of cellular mechanotransduction*. Annual Review of Physiology, 1997. **59**: p. 575-599.
103. Stamenovic, D. and M.F. Coughlin, *The role of prestress and architecture of the cytoskeleton and deformability of cytoskeletal filaments in mechanics of adherent cells: a quantitative analysis*. Journal of Theoretical Biology, 1999. **201**(1): p. 63-74.
104. Chen, L., A. Offenhausser, and H.J. Krause, *Magnetic tweezers with high permeability electromagnets for fast actuation of magnetic beads*. Review of Scientific Instruments, 2015. **86**(4): 044701.
105. Chen, L., et al., *Statistical study of biomechanics of living brain cells during growth and maturation on artificial substrates*. submitted to Biomaterials, 2016.
106. Chipperfield, A.J. and P.J. Fleming. *The MATLAB genetic algorithm toolbox*. in *Applied Control Techniques Using MATLAB*, IEE Colloquium on, 1995: 10.
107. Cheezum, M.K., W.F. Walker, and W.H. Guilford, *Quantitative comparison of algorithms for tracking single fluorescent particles*. Biophysical Journal, 2001. **81**(4): p. 2378-2388.
108. van Loenhout, M.T.J., et al., *Non-Bias-Limited Tracking of Spherical Particles, Enabling Nanometer Resolution at Low Magnification*. Biophysical Journal, 2012. **102**(10): p. 2362-2371.

109. Lipfert, J., et al., *A method to track rotational motion for use in single-molecule biophysics*. Review of Scientific Instruments, 2011. **82**(10): 103707.
110. Lucas, B.D. and T. Kanade. *An iterative image registration technique with an application to stereo vision*. in *IJCAI*. 1981: p674-679.
111. Claycomb, W.C., et al., *HL-1 cells: A cardiac muscle cell line that contracts and retains phenotypic characteristics of the adult cardiomyocyte*. Proceedings of the National Academy of Sciences of the United States of America, 1998. **95**(6): p. 2979-2984.
112. White, S.M., P.E. Constantin, and W.C. Claycomb, *Cardiac physiology at the cellular level: use of cultured HL-1 cardiomyocytes for studies of cardiac muscle cell structure and function*. American Journal of Physiology-Heart and Circulatory Physiology, 2004. **286**(3): p. H823-H829.
113. Rinklin, P., *Microwire crossbar arrays for chemical, mechanical, and thermal stimulation of cells*, RWTH Aachen University, 2014.
114. Ochsner, M., et al., *Micro-well arrays for 3D shape control and high resolution analysis of single cells*. Lab on a Chip, 2007. **7**(8): p. 1074-1077.
115. Santoro, F., *3D nanoelectrodes for bioelectronics: design and characterization of the cell-electrode interface*, RWTH aachen university, 2014.
116. Chen, L., et al., *Characterization of the mechanical properties of HL-1 cardiomyocytes with high throughput magnetic tweezers*. Applied Physics Letters, 2015. **107**(5): 053703.
117. Chen, L., A. Offenhausser, and H.J. Krause, *An inspection of force reduction in high force electromagnetic tweezers made of FeCo-V foil by laser cutting*. Journal of Applied Physics, 2015. **118**(12): 124701.
118. Chen, L., et al., *Passivation of magnetic material used in cell culture environment*. Sensors and Actuators B: Chemical, 2016. **236**: p. 85-90.
119. Chen, L., et al., *Implementation and application of a novel 2D magnetic twisting cytometry based on multi-pole electromagnet*. Review of Scientific Instruments, 2016. **87**(6): 064301.
120. Belhadj, A., P. Baudouin, and Y. Houbaert, *Simulation of the HAZ and magnetic properties of laser cut non-oriented electrical steels*. Journal of Magnetism and Magnetic Materials, 2002. **248**(1): p. 34-44.
121. Hall, R.C., *Magnetic Anisotropy and Magnetostriction of Ordered and Disordered Cobalt-Iron Alloys*. Journal of Applied Physics, 1960. **31**(5): p. S157-S158.
122. Bozorth, R.M., *Ferromagnetism*. New York: Van Nostrand, 1951.
123. Yu, R.H., et al., *Pinning effect of the grain boundaries on magnetic domain wall in FeCo-based magnetic alloys*. Journal of Applied Physics, 1999. **85**(9): p. 6655-6659.
124. Lipfert, J., X.M. Hao, and N.H. Dekker, *Quantitative Modeling and Optimization of Magnetic Tweezers*. Biophysical Journal, 2009. **96**(12): p. 5040-5049.
125. Chung, Y. and J. Galayda, *Effect of Eddy Current in the Laminations on the Magnet Field*. Argonne National Laboratory, 1992.
126. Hale, C.M., S.X. Sun, and D. Wirtz, *Resolving the Role of Actomyosin Contractility in Cell Microrheology*. Plos One, 2009. **4**(9).
127. Hofmann, U.G., et al., *Investigating the cytoskeleton of chicken cardiocytes with the atomic force microscope*. Journal of Structural Biology, 1997. **119**(2): p. 84-91.
128. Lieber, S.C., et al., *Aging increases stiffness of cardiac myocytes measured by atomic force microscopy nanoindentation*. American Journal of Physiology-Heart and Circulatory Physiology, 2004. **287**(2): p. H645-H651.
129. Pelloux, S., et al., *Non-beating HL-1 cells for confocal microscopy: Application to mitochondrial functions during cardiac preconditioning*. Progress in Biophysics & Molecular Biology, 2006. **90**(1-3): p. 270-298.
130. Fabry, B., et al., *Implications of heterogeneous bead behavior on cell mechanical properties measured with magnetic twisting cytometry*. Journal of Magnetism and Magnetic Materials, 1999. **194**(1-3): p. 120-125.
131. De Los Santos, V.L., et al., *Magnetic measurements of suspended functionalised ferromagnetic beads under DC applied fields*. Journal of Magnetism and Magnetic Materials, 2009. **321**(14): p. 2129-2134.
132. Mijailovich, S.M., et al., *A finite element model of cell deformation during magnetic bead twisting*. Journal of Applied Physiology, 2002. **93**(4): p. 1429-1436.
133. Lieber, S., J. Pain, and G. Diaz, *Aging increases stiffness of cardiac myocytes measured by atomic force microscopy*. Circulation, 2003. **108**(17): p. 276-276.

134. Hersch, N., et al., *The constant beat: cardiomyocytes adapt their forces by equal contraction upon environmental stiffening*. Biology Open, 2013. **2**(3): p. 351-U119.
135. Pfister, B.J., et al., *Extreme stretch growth of integrated axons*. Journal of Neuroscience, 2004. **24**(36): p. 7978-7983.
136. Grevesse, T., et al., *Opposite rheological properties of neuronal microcompartments predict axonal vulnerability in brain injury*. Scientific Reports, 2015. **5**: 9475.
137. Darvish, K.K. and J.R. Crandall, *Nonlinear viscoelastic effects in oscillatory shear deformation of brain tissue*. Medical Engineering & Physics, 2001. **23**(9): p. 633-645.
138. Cheng, S., E.C. Clarke, and L.E. Bilston, *Rheological properties of the tissues of the central nervous system: A review*. Medical Engineering & Physics, 2008. **30**(10): p. 1318-1337.
139. Lu, Y.B., et al., *Reactive glial cells: increased stiffness correlates with increased intermediate filament expression*. Faseb Journal, 2011. **25**(2): p. 624-631.
140. Lu, Y.B., et al., *Viscoelastic properties of individual glial cells and neurons in the CNS*. Proceedings of the National Academy of Sciences of the United States of America, 2006. **103**(47): p. 17759-17764.
141. Georges, P.C., et al., *Matrices with compliance comparable to that of brain tissue select neuronal over glial growth in mixed cortical cultures*. Biophysical Journal, 2006. **90**(8): p. 3012-3018.
142. Moshayedi, P., et al., *The relationship between glial cell mechanosensitivity and foreign body reactions in the central nervous system*. Biomaterials, 2014. **35**(13): p. 3919-3925.
143. Morrison, R.S., et al., *Hormones and Growth-Factors Induce the Synthesis of Glial Fibrillary Acidic Protein in Rat-Brain Astrocytes*. Journal of Neuroscience Research, 1985. **14**(2): p. 167-176.
144. Franze, K. and J. Guck, *The biophysics of neuronal growth*. Reports on Progress in Physics, 2010. **73**(9): 094601.
145. Jiang, F.X., et al., *Probing Mechanical Adaptation of Neurite Outgrowth on a Hydrogel Material Using Atomic Force Microscopy*. Annals of Biomedical Engineering, 2011. **39**(2): p. 706-713.
146. Saha, K., et al., *Substrate Modulus Directs Neural Stem Cell Behavior*. Biophysical Journal, 2008. **95**(9): p. 4426-4438.
147. Solon, J., et al., *Fibroblast adaptation and stiffness matching to soft elastic substrates*. Biophysical Journal, 2007. **93**(12): p. 4453-4461.
148. Chiou, C.H., et al., *New magnetic tweezers for investigation of the mechanical properties of single DNA molecules*. Nanotechnology, 2006. **17**(5): p. 1217-1224.
149. Fricke, R., et al., *Axon guidance of rat cortical neurons by microcontact printed gradients*. Biomaterials, 2011. **32**(8): p. 2070-2076.
150. Wang, Y.L. and D.E. Discher, *Cell Mechanics*. Elsevier Science, 2007.
151. Kilinc, D., et al., *Low Piconewton Towing of CNS Axons against Diffusing and Surface-Bound Repellents Requires the Inhibition of Motor Protein-Associated Pathways*. Scientific Reports, 2014. **4**: 7128.

Abbreviations

Abbreviation	Description
AFM	Atomic Force Microscope
ANOVA	Analysis of Variance
BB	Blocking Buffer
CMOS	Complementary Metal-oxide-semiconductor
COM	Center of Mass
CPD	Critical Point Drying
DAC	Digital-to-analog Converter
DAPI	4',6-diamidino-2-phenylindole
DAQ	Data Acquisition
DEG	Diethylene Glycol
DIV	Days in Vitro
DMEM	Dulbecco's Modified Eagle Medium
ECM	Extracellular Matrix
EDS	Energy Dispersive X-ray Spectroscopy
FBS	Fetal Bovine Serum
FEM	Finite Element Method
FIB	Focused Ion Beam
FPGA	Field-programmable Gate Array
GFAP	Glial Fibrillary Acidic Protein
HAZ	Heat-affected Zone
HBSS	Hanks Balanced Salt Solution
HEK	Human Embryonic Kidney
HL-1	A Cardiomyocyte-like Cell Line
ICP-MS	Inductively Coupled Plasma Mass Spectrometry
LED	Light-emitting Diode
LSB	Least Significant Bit
LUT	Lookup Table
MMF	Magnetomotive Force
MNP	Magnetic Nanoparticle
MT	Magnetic Tweezers
MTC	Magnetic Twisting Cytometry
NFH	Neurofilament Heavy
N.S.	No Statistical Significance
OF	Optical Flow
OT	Optical Tweezers
PA	Polyacrymide
PBS	Phosphate Buffered Saline
PDL	Poly-D-lysine
PDMS	Polydimethylsiloxane
PI	Proportional Integral
PPy	Polypyrrole
PTM	Particle Tracking Microheology
RIO	Reconfigurable Input/Output
ROI	Region of Interest
sCMOS	scientific CMOS
SEM	Scanning Electron Microscope
SGR	Soft Glassy Rheology
SNR	Signal-to-noise Ratio
XCor	Cross-correlation

Author's list of publications

1. La Chen, Andreas Offenhäusser, and Hans-Joachim Krause, *Magnetic tweezers with high permeability electromagnets for fast actuation of magnetic beads*, Review of Scientific Instruments **86**, 044701 (2015).
2. La Chen, Andreas Offenhäusser, and Hans-Joachim Krause, *An inspection of force reduction in high force electromagnetic tweezers made of FeCo-V foil by laser cutting*, Journal of Applied Physics **118**, 124701 (2015).
3. La Chen, Vanessa Maybeck, Andreas Offenhäusser, and Hans-Joachim Krause, *Characterization of the mechanical properties of HL-1 cardiomyocytes with high throughput magnetic tweezers*, Applied Physics Letters **107**, 053703 (2015).
4. La Chen, Vanessa Maybeck, Andreas Offenhäusser, and Hans-Joachim Krause, *Implementation and application of a novel 2D magnetic twisting cytometry based on multi-pole electromagnet*, Review of Scientific Instruments **87**, 064301 (2016).
5. La Chen, Andreas Omenzetter, Uwe Schnakenberg, Vanessa Maybeck, Andreas Offenhäusser, and Hans-Joachim Krause, *Passivation of magnetic material used in cell culture environment*, Sensors and Actuators B: Chemical **236**, 85 (2016).
6. La Chen, Wenfang Li, Vanessa Maybeck, Andreas Offenhäusser, and Hans-Joachim Krause, *Statistical study of biomechanics of living brain cells during growth and maturation on artificial substrates*, submitted to Biomaterials (2016).

Acknowledgments

There are many people I would like to thank for their help, support, and encouragement during my PhD work.

Prof. Andreas Offenhäusser, I would like to thank you for giving me the opportunity to work in the institute (ICS-8/PGI-8), and also for your support and advice in the whole project.

Dr. Hans-Joachim Krause, I would like to thank you for supervising my work, your guidance which was very important for me to find the right way to go, and all the kind encouragements during these years.

Prof. Jörg Fitter, I thank you for reviewing my thesis.

Dr. Vanessa Maybeck, I would also like to thank you for all the engaging biology discussions and lots of suggestions for the paper manuscripts.

Dieter Lomparski, I especially thank you for your instruction and help in the setups' mechanical construction design and LabVIEW programming. Some engineering ideas from you give me a great pull.

Norbert Wolters, I am grateful to you and your team for all PCB designs and the electronics development.

Alexander Kuck and your team, I thank you for the manufacturing of all kinds of mechanical parts and the patience for a layman like me.

Philipp Rinklin, I would like to thank you for introducing me the first practice to cell culture and helpful discussion in the beginning of this project.

Wenfang Li, I am grateful to you for preparing neuronal and glial cells and lots of biology discussion.

Lei Jin and Liping Du, I would like thank you for the help in cell cultures and also many biology discussion.

Dr. Swen Graubner (SEKELS GmbH), I should thank you for your professional suggestion in the magnetic yoke design and lots of exhaustive explanation to my questions.

Dr. Elmar Neumann, Elke, Stephany Bunte, I thank you for your help in cell SEM sample preparation, FIB cutting, and the EDS analyses of magnetic tips, respectively.

Tina and Rita, I thank you for the neuronal cell preparation and bio-lab support.

Dr. Uwe Shnakenberg and Andreas Omenzetter (IWE1, RWTH Aachen), I want to thank you for the Parylene coating of the magnetic tips.

Prof. Hamid Kokabi and Amine Rabehi (L2E, UMPC, France), I am grateful to your help in the time during Paris and the PROCOPE project we worked on.

Prof. Yi Zhang, many thanks for the help and advice in scientific work and daily life.

I would like to thank all the former and present members of the magnetic sensors group and the colleagues in PGI-8/ICS-8. Thank you for your support, your friendship, and the good time we spent together.

I also thank the China Scholar Council for the financial support during this work.

And finally I would thank my parents for their education and support during these decades.

Appendix

Table A.1 Immunostaining antibodies for brain cells

Neuron	Primary antibody	Second antibody
	Anti-MAP2 Mouse (1:500, Millipore)	Anti-Mouse Alexa Fluor 633 (1:1000, Life Technologies)
	Anti-Beta III Tubulin Rabbit (1:1000, Cell Signaling)	Anti-Rabbit Alexa Fluor 488 (1:1000, Life Technologies)
	Anti-NFH 200 kDa Chicken (1:500, Abcam)	Anti-Chicken Alexa Fluor 546 (1:1000, Life Technologies)
	Anti F-Actin Phalloidin Alexa Fluor 633 (200 unit/ml, Life Technologies)	—
	DAPI (1:1000, Life Technologies)	—
Glia	Primary antibody	Second antibody
	Anti-GFAP Mouse (1:500, Millipore)	Anti-Mouse Alexa Fluor 488 (1:1000, Life Technologies)
	Anti F-Actin Phalloidin Alexa Fluor 633 (200 unit/ml, ThermoFisher)	—
	DAPI (1:1000, Life Technologies)	—

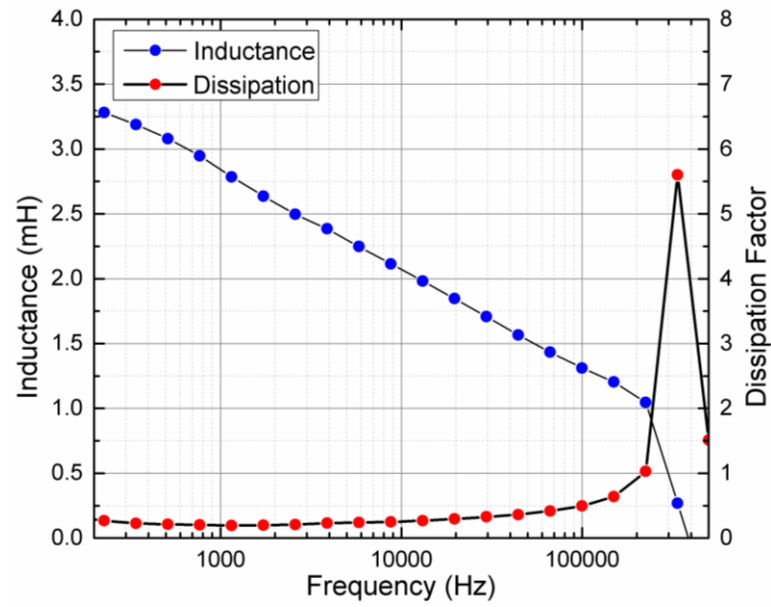


Fig. A.1. Inductance of yoke coil with 160 turns.

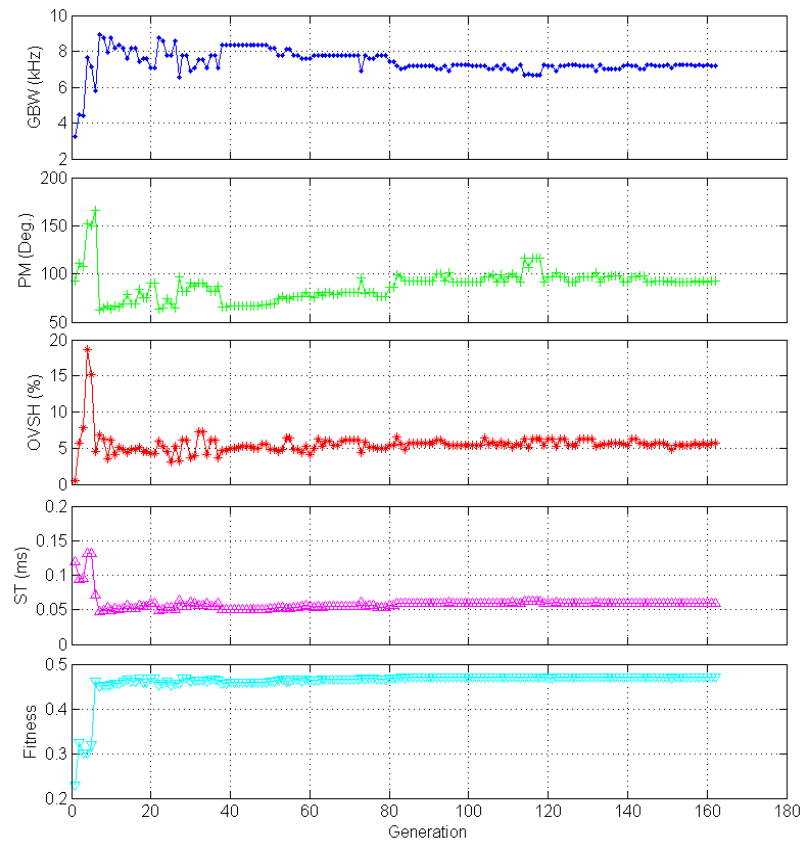


Fig. A.2. Optimization of amplifier with Genetic Algorithm.

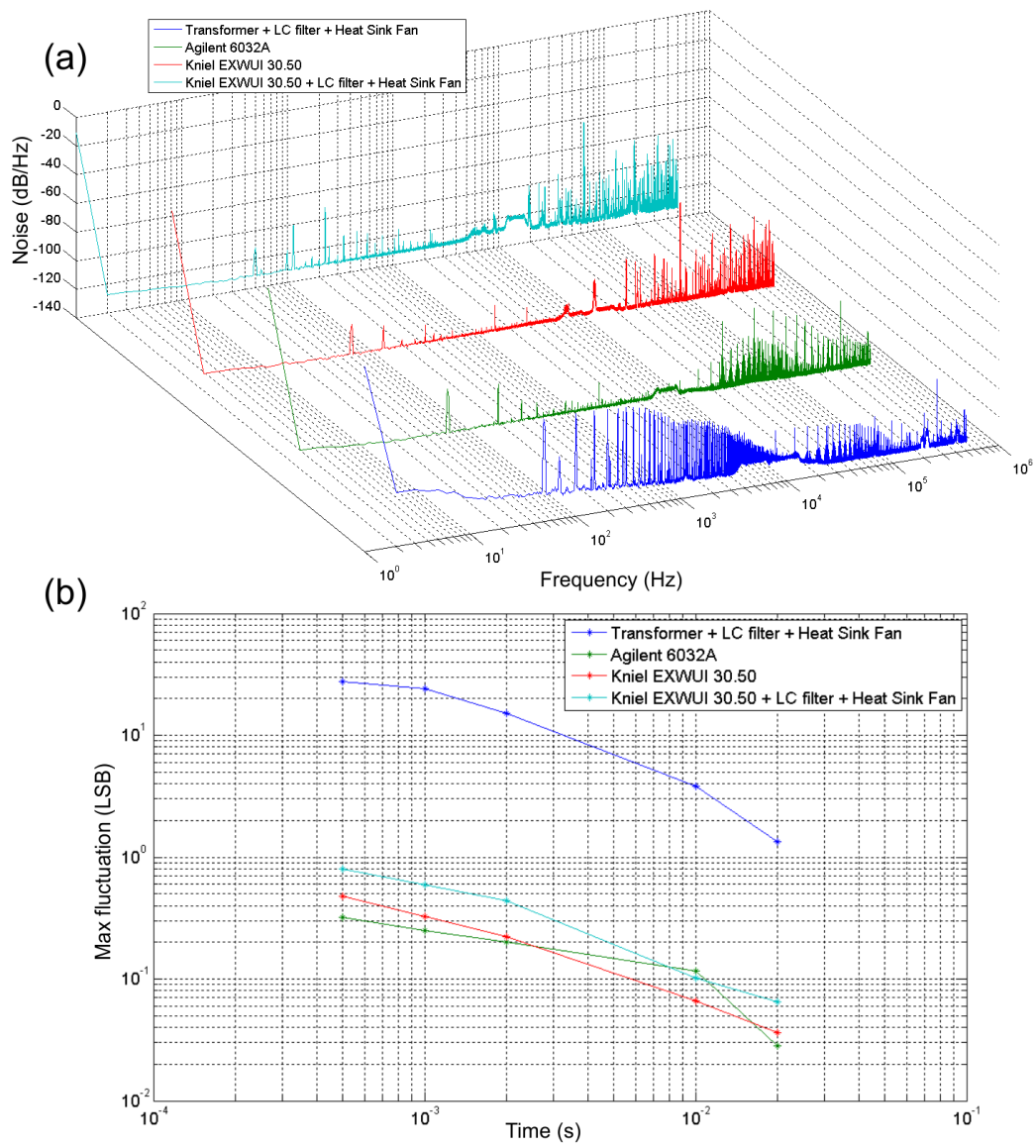


Fig. A.3. Noise of amplifier with different power supplies.

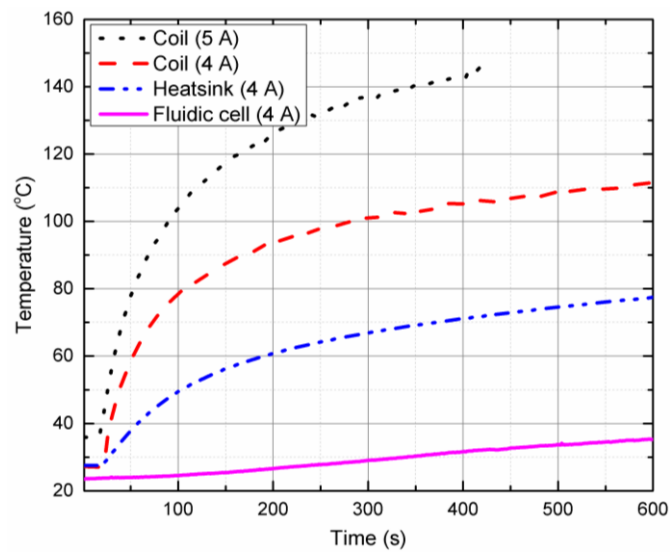


Fig. A.4. Temperature test.

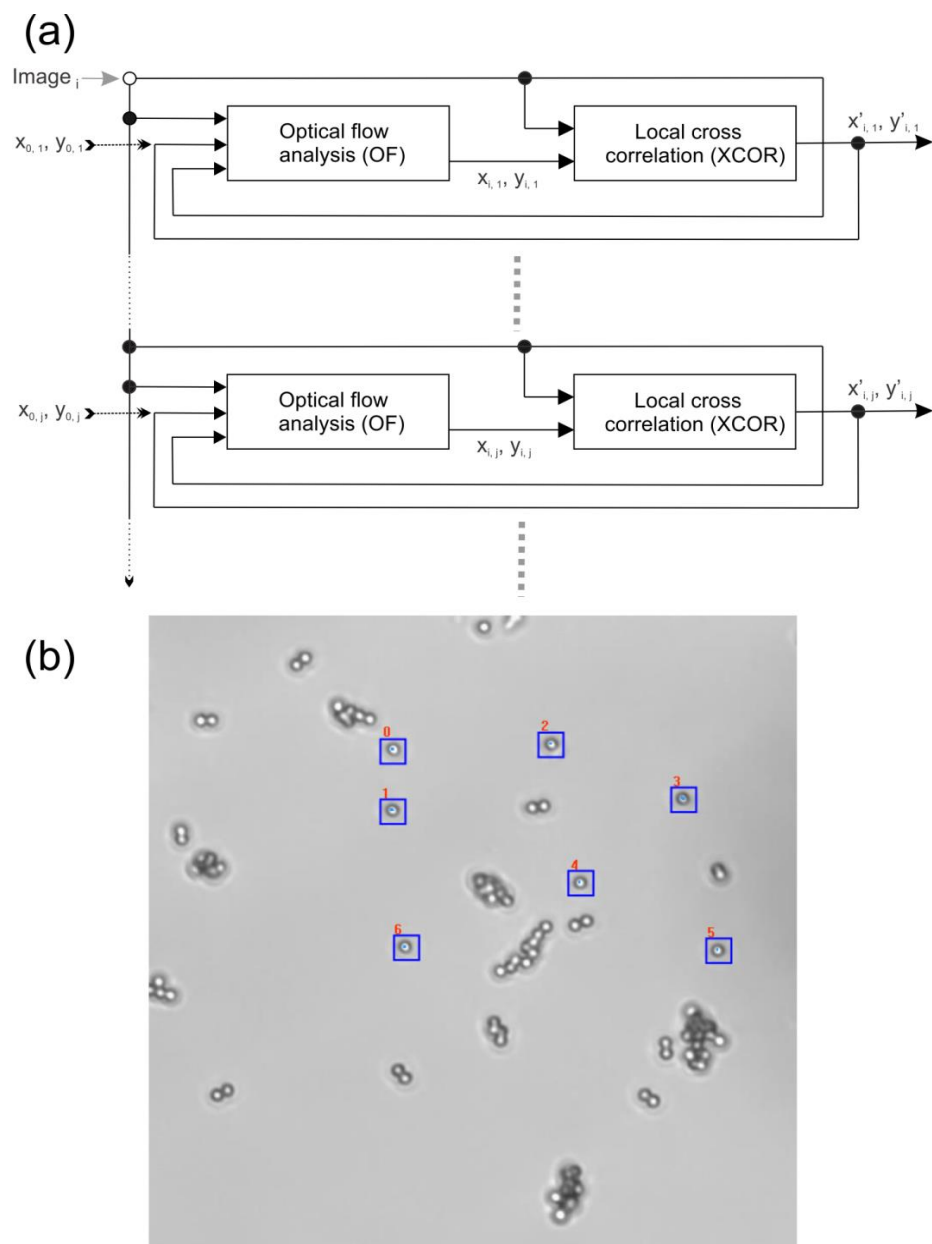


Fig. A.5. Multi-particle tracking

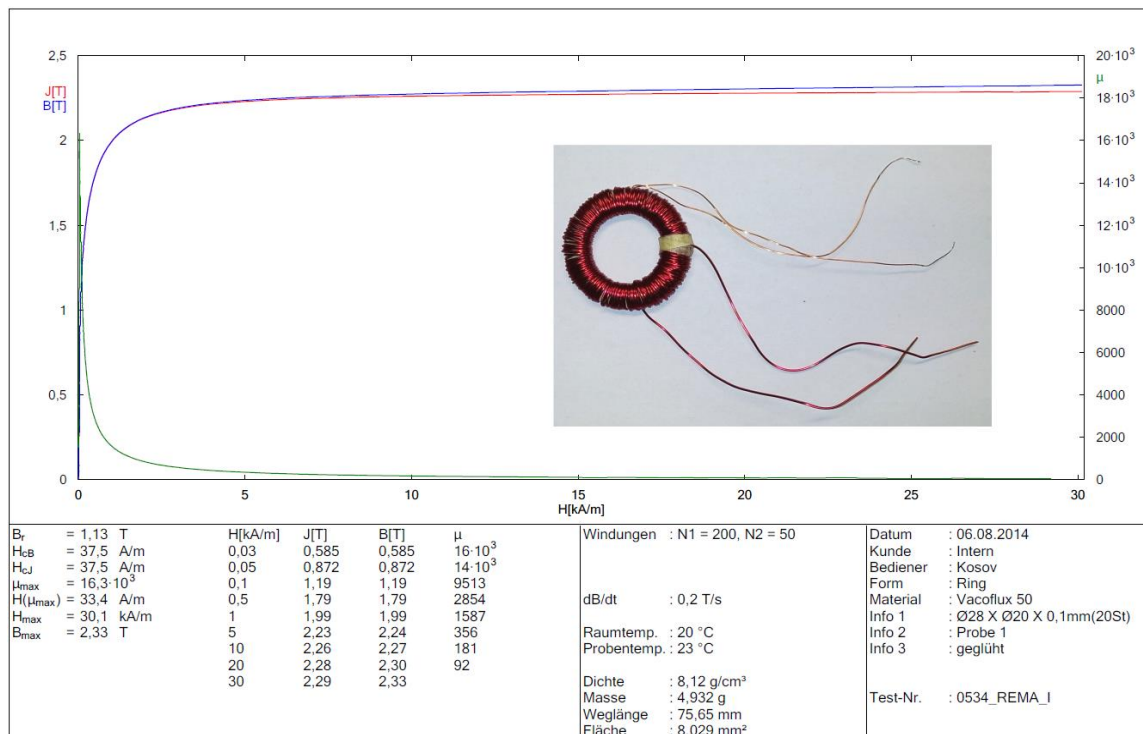


Fig. A.6. B - H measurement of 0.1 mm thick VACFLUX50 foil

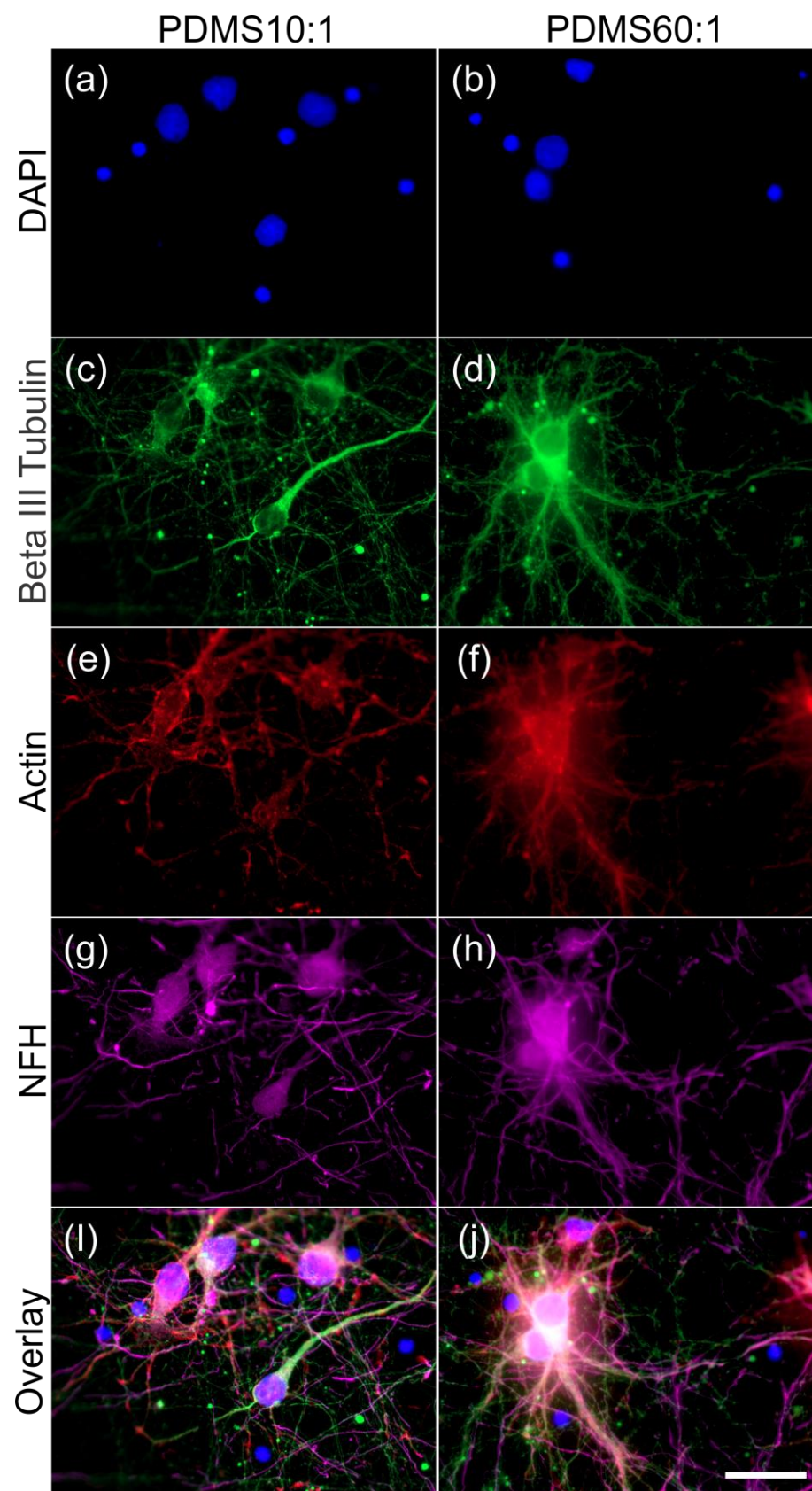


Fig. A.7. (a) - (b) Nucleus staining. (c) - (d) Microtubulin staining. (e) - (f) F-Actin staining. (g) - (h) Neurofilament staining. (i) - (j) Overlay. Scale bar 30 μm .

Script A.1 Inverse force model ---→

```

1. %% Workspace: 51*51 grid, one step is 2 μm
2. Bixy= load('Bixy3.txt'); % load magnetic field lookup table
3. mkb= load('mkb.txt'); % load B-H data of particle
4. mkb_n= max(size(mkb));
5. cur=zeros(3,1); % currents output
6. x=0E-6;y=0E-6; % position input
7. fx=400E-12;fy=00E-12; % force input
8.
9. step= 2e-6; % step length
10. sxy= step *step;
11. Bx=zeros(3,1);Bxx=zeros(3,1);Bxy=zeros(3,1);By=zeros(3,1);Byy=zeros(3,1);Byx=zeros(3,1);
12. B_m=zeros(3,1);
13. Ia=0;c=0;
14. Fvec=zeros(3,2);Fdot=zeros(3,1);
15. % if input position is out of workspace, stop program
16. if (fx==0)&&(fy==0) || (abs(x)>48e-6) || (abs(y)>48e-6)
17. cur=zeros(3,1);
18. return;
19. end
20. % get array index
21. nx=ceil((50.0e-6+x)/step);
22. ny=ceil((50.0e-6+y)/step);
23. for p=1:3
24. % calculate magnetic (gradient) field on 4 neighbor sites
25. bx11=Bixy((ny-1)*51+nx,2*p+1);
26. bxx11=(Bixy((ny-1)*51+nx+1,2*p+1)-Bixy((ny-1)*51+nx-1,2*p+1))/(2*step);
27. bxy11=(Bixy((ny-1+1)*51+nx,2*p+1)-Bixy((ny-1-1)*51+nx,2*p+1))/(2*step);
28. by11=Bixy((ny-1)*51+nx,2*p+2);
29. byx11=(Bixy((ny-1)*51+nx+1,2*p+2)-Bixy((ny-1)*51+nx-1,2*p+2))/(2*step);
30. byy11=(Bixy((ny-1+1)*51+nx,2*p+2)-Bixy((ny-1-1)*51+nx,2*p+2))/(2*step);
31.
32. bx12=Bixy((ny-1+1)*51+nx,2*p+1);
33. bxx12=(Bixy((ny-1+1)*51+nx+1,2*p+1)-Bixy((ny-1+1)*51+nx-1,2*p+1))/(2*step);
34. bxy12=(Bixy((ny-1+1+1)*51+nx,2*p+1)-Bixy((ny-1+1-1)*51+nx,2*p+1))/(2*step);
35. by12=Bixy((ny-1+1)*51+nx,2*p+2);
36. byx12=(Bixy((ny-1+1)*51+nx+1,2*p+2)-Bixy((ny-1+1)*51+nx-1,2*p+2))/(2*step);
37. byy12=(Bixy((ny-1+1+1)*51+nx,2*p+2)-Bixy((ny-1+1-1)*51+nx,2*p+2))/(2*step);
38.
39. bx21=Bixy((ny-1)*51+nx+1,2*p+1);
40. bxx21=(Bixy((ny-1)*51+nx+1+1,2*p+1)-Bixy((ny-1)*51+nx+1-1,2*p+1))/(2*step);
41. bxy21=(Bixy((ny-1+1)*51+nx+1,2*p+1)-Bixy((ny-1-1)*51+nx+1,2*p+1))/(2*step);
42. by21=Bixy((ny-1)*51+nx+1,2*p+2);
43. byx21=(Bixy((ny-1)*51+nx+1+1,2*p+2)-Bixy((ny-1)*51+nx+1-1,2*p+2))/(2*step);
44. byy21=(Bixy((ny-1+1)*51+nx+1,2*p+2)-Bixy((ny-1-1)*51+nx+1,2*p+2))/(2*step);
45.
46. bx22=Bixy((ny-1+1)*51+nx+1,2*p+1);
47. bxx22=(Bixy((ny-1+1)*51+nx+1+1,2*p+1)-Bixy((ny-1+1)*51+nx+1-1,2*p+1))/(2*step);
48. bxy22=(Bixy((ny-1+1+1)*51+nx+1,2*p+1)-Bixy((ny-1+1-1)*51+nx+1,2*p+1))/(2*step);
49. by22=Bixy((ny-1+1)*51+nx+1,2*p+2);
50. byx22=(Bixy((ny-1+1)*51+nx+1+1,2*p+2)-Bixy((ny-1+1)*51+nx+1-1,2*p+2))/(2*step);
51. byy22=(Bixy((ny-1+1+1)*51+nx+1,2*p+2)-Bixy((ny-1+1-1)*51+nx+1,2*p+2))/(2*step);
52. % bilinear interpolate
53. x1=(nx-26)*2e-6;x2=(nx-25)*2e-6;y1=(ny-26)*2e-6;y2=(ny-25)*2e-6;
54. Bx(p,1)=bx11*(x2-x)*(y2-y)/sxy+bxx11*(x-x1)*(y2-y)/sxy+bxx12*(x2-x)*(y-y1)/sxy+bxx22*(x-x1)*(y-y1)/sxy;
55. Bxx(p,1)=bxx11*(x2-x)*(y2-y)/sxy+bxx21*(x-x1)*(y2-y)/sxy+bxx12*(x2-x)*(y-y1)/sxy+bxx22*(x-x1)*(y-y1)/sxy;
56. Bxy(p,1)=bxy11*(x2-x)*(y2-y)/sxy+bxy21*(x-x1)*(y2-y)/sxy+bxy12*(x2-x)*(y-y1)/sxy+bxy22*(x-x1)*(y-y1)/sxy;
57. By(p,1)=by11*(x2-x)*(y2-y)/sxy+by21*(x-x1)*(y2-y)/sxy+by12*(x2-x)*(y-y1)/sxy+by22*(x-x1)*(y-y1)/sxy;
58. Byx(p,1)=byx11*(x2-x)*(y2-y)/sxy+byx21*(x-x1)*(y2-y)/sxy+byx12*(x2-x)*(y-y1)/sxy+byx22*(x-x1)*(y-y1)/sxy;
59. Byy(p,1)=byy11*(x2-x)*(y2-y)/sxy+byy21*(x-x1)*(y2-y)/sxy+byy12*(x2-x)*(y-y1)/sxy+byy22*(x-x1)*(y-y1)/sxy;
60.
61. B_m(p,1)=sqrt(Bx(p,1)^2+By(p,1)^2);
62. for m=1:mkb_n
63. if (mkb(m,3)<=B_m(p,1))&&(B_m(p,1)<mkb(m,4))
64. km=mkb(m,1)+mkb(m,2)/B_m(p,1); % km= m(B)/abs(B)
65. break;
66. else
67. continue;
68. end
69. end
70. Fvec(p,1)=km*(Bx(p,1)*Bxx(p,1)+By(p,1)*Byx(p,1));
71. Fvec(p,2)=km*(Bx(p,1)*Bxy(p,1)+By(p,1)*Byy(p,1));

```



```

72. Fdot(p,1)=(Fvec(p,1)*fx+Fvec(p,2)*fy)/sqrt(Fvec(p,1)^2+Fvec(p,2)^2)/sqrt(fx^2+fy^2);
73. end
74.
75. [proja,a]=max(Fdot); % get the max projection direction
76. Fdot(a,1)=-1;
77. [projb,b]=max(Fdot); % get the 2nd max projection direction
78.
79. % assume Ib=c*Ia;
80. k11=(Bx(a,1)*Bxx(a,1)+By(a,1)*Byx(a,1)); % IaIa
81. k12=(Bx(a,1)*Bxx(b,1)+Bx(b,1)*Bxx(a,1)+By(b,1)*Byx(a,1)+By(a,1)*Byx(b,1)); % IaIb
82. k13=(Bx(b,1)*Bxx(b,1)+By(b,1)*Byx(b,1)); % IbIb
83.
84. k21=(Bx(a,1)*Bxy(a,1)+By(a,1)*Byy(a,1)); % IaIa
85. k22=(Bx(a,1)*Bxy(b,1)+Bx(b,1)*Bxy(a,1)+By(a,1)*Byy(b,1)+By(b,1)*Byy(a,1)); % IaIb
86. k23=(Bx(b,1)*Bxy(b,1)+By(b,1)*Byy(b,1)); % IbIb
87.
88. % if the project angle exceed the threshold (~2.5 degree), apply a single coil current.
89. if proja>0.999
90.     c=0;
91. else
92.     if fx==0
93.         c1=0.5*(-k12+sqrt(k12^2-4*k11*k13))/k13;
94.         c2=0.5*(-k12-sqrt(k12^2-4*k11*k13))/k13;
95.     elseif fy==0
96.         c1=0.5*(-k22+sqrt(k22^2-4*k21*k23))/k23;
97.         c2=0.5*(-k22-sqrt(k22^2-4*k21*k23))/k23;
98.     else
99.         c1=0.5*(-(k22*fx-k12*fy)+sqrt((k22*fx-k12*fy)^2-4*(k23*fx-k13*fy)*(k21*fx-
k11*fy)))/(k23*fx-k13*fy);
100.        c2=0.5*(-(k22*fx-k12*fy)-sqrt((k22*fx-k12*fy)^2-4*(k23*fx-k13*fy)*(k21*fx-
k11*fy)))/(k23*fx-k13*fy);
101.    end
102.    c=min(c1,c2); % choose c< 0
103. end
104.
105. Bik=sqrt((Bx(a,1)^2+By(a,1)^2)+(Bx(b,1)^2+By(b,1)^2)*c^2+2*c*(Bx(a,1)*Bx(b,1)+By(a,1)*
By(b,1))); % B= Bik*Ia
106. for n=1:mkb_n
107.     mk=mkb(n,1);mb=mkb(n,2);
108.     if fx==0
109.         f0=fy/(k21+k22*c+k23*c^2);
110.     else
111.         f0=fx/(k11+k12*c+k13*c^2);
112.     end
113.
114.     if (mb/Bik)^2+4*mk*f0<0
115.         continue;
116.     end
117.
118.     Ia1=0.5*(-mb/Bik+sqrt((mb/Bik)^2+4*mk*f0))/mk;
119.     Ia2=0.5*(-mb/Bik-sqrt((mb/Bik)^2+4*mk*f0))/mk;
120.
121.     % verify whether the resulting B is located in the right range.
122.     if (mkb(n,3)<abs(Bik*Ia1)) && (abs(Bik*Ia1)<mkb(n,4))
123.         Ia=Ia1;
124.         break;
125.     elseif (mkb(n,3)<abs(Bik*Ia2)) && (abs(Bik*Ia2)<mkb(n,4))
126.         Ia=Ia2;
127.         break;
128.     end
129. end
130.
131. Ib=c*Ia;
132. cur(a,1)=Ia; cur(b,1)=Ib;
133. cur=cur*[1,-0.5,-0.5; -0.5,1,-0.5; -0.5,-0.5,1] % print currents

```

←--- Script A.1